Astronomy & Astrophysics

The fundamental plane of EDisCS galaxies

The effect of size evolution[*],[**]

R. P. Saglia[1,2], P. Sánchez-Blázquez[3,4], R. Bender[2,1], L. Simard[5], V. Desai[6], A. Aragón-Salamanca[7],
B. Milvang-Jensen[8], C. Halliday[9], P. Jablonka[10,11], S. Noll[12], B. Poggianti[13], D. I. Clowe[14], G. De Lucia[15], R. Pelló[16],
G. Rudnick[17], T. Valentinuzzi[18], S. D. M. White[19], and D. Zaritsky[20]

(Affiliations can be found after the references)

ABSTRACT

We study the evolution of spectral early-type galaxies in clusters, groups, and the field up to redshift 0.9 using the ESO Distant Cluster Survey (EDisCS) dataset. We measure structural parameters (circularized half-luminosity radii R_e, surface brightness I_e, and velocity dispersions σ) for 154 cluster and 68 field galaxies. On average, we achieve precisions of 10% in R_e, 0.1 dex in $\log I_e$, and 10% in σ. We sample $\approx$20% of cluster and $\approx$10% of field spectral early-type galaxies to an I band magnitude in a 1 arcsec radius aperture as faint as $I_1 = 22$. We study the evolution of the zero point of the fundamental plane (FP) and confirm results in the literature, but now also for the low cluster velocity dispersion regime. Taken at face value, the mass-to-light ratio varies as $\Delta \log M/L_B = (-0.54 \pm 0.01)z = (-1.61 \pm 0.01) \log(1 + z)$ in clusters, independent of their velocity dispersion. The evolution is stronger ($\Delta \log M/L_B = (-0.76 \pm 0.01)z = (-2.27 \pm 0.03) \log(1 + z)$) for field galaxies. A somewhat milder evolution is derived if a correction for incompleteness is applied. A rotation in the FP with redshift is detected with low statistical significance. The α and β FP coefficients decrease with redshift, or, equivalently, the FP residuals correlate with galaxy mass and become progressively negative at low masses. The effect is visible at $z \geq 0.7$ for cluster galaxies and at lower redshifts $z \geq 0.5$ for field galaxies. We investigate the size evolution of our galaxy sample. In agreement with previous results, we find that the half-luminosity radius for a galaxy with a dynamical or stellar mass of $2 \times 10^{11} M_\odot$ varies as $(1 + z)^{-1.0 \pm 0.3}$ for both cluster and field galaxies. At the same time, stellar velocity dispersions grow with redshift, as $(1 + z)^{0.59 \pm 0.10}$ at constant dynamical mass, and as $(1 + z)^{0.34 \pm 0.14}$ at constant stellar mass. The measured size evolution reduces to $R_e \propto (1 + z)^{-0.5 \pm 0.2}$ and $\sigma \propto (1 + z)^{0.41 \pm 0.08}$, at fixed dynamical masses, and $R_e \propto (1 + z)^{-0.68 \pm 0.4}$ and $\sigma \propto (1 + z)^{0.19 \pm 0.10}$, at fixed stellar masses, when the progenitor bias (PB, galaxies that locally are of spectroscopic early-type, but are not very old, disappear progressively from the EDisCS high-redshift sample; often these galaxies happen to be large in size) is taken into account. Taken together, the variations in size and velocity dispersion imply that the luminosity evolution with redshift derived from the zero point of the FP is somewhat milder than that derived without taking these variations into account. When considering dynamical masses, the effects of size and velocity dispersion variations almost cancel out. For stellar masses, the luminosity evolution is reduced to $L_B \propto (1 + z)^{1.0}$ for cluster galaxies and $L_B \propto (1 + z)^{1.67}$ for field galaxies. Using simple stellar population models to translate the observed luminosity evolution into a formation age, we find that massive ($>10^{11} M_\odot$) cluster galaxies are old (with a formation redshift $z_f > 1.5$) and lower mass galaxies are 3−4 Gyr younger, in agreement with previous EDisCS results from color and line index analyses. This confirms the picture of a progressive build-up of the red sequence in clusters with time. Field galaxies follow the same trend, but are $\approx$1 Gyr younger at a given redshift and mass. Taking into account the size and velocity dispersion evolution quoted above pushes all formation ages upwards by 1 to 4 Gyr.

Key words. galaxies: elliptical and lenticular, cD – galaxies: evolution – galaxies: formation – galaxies: fundamental parameters

1. Introduction

Despite their apparent simplicity, the physical processes involved in the formation of early-type galaxies (E/S0) remain unclear. The tightness of their scaling relations, such as the color-magnitude relation, and their slow evolution with redshift, are indicative of a very early and coordinated formation of their stars (e.g., van Dokkum et al. 2000; Blakeslee et al. 2003; Menanteau et al. 2004). However, in the ΛCDM paradigm, these galaxies are expected to form through mergers of smaller subsystems over a wide redshift range, managing to obey these constraints (Kauffmann 1996; De Lucia et al. 2006).

A particularly interesting relation is that of the fundamental plane (hereafter FP). In the parameter space of central velocity dispersion (σ), galaxy effective radius (R_e), and effective surface brightness ($SB_e = -2.5 \log I_e$), elliptical galaxies occupy a plane, known as the FP (Dressler et al. 1987; Djorgovski & Davis 1987), which exhibits very little scatter ($\sim$0.1 dex). The FP is usually expressed in the form

$$\log R_e = \alpha \log \sigma + \beta SB_e + ZP, \tag{1}$$

where the zero point, hereafter ZP, is computed from the mean values $\overline{\log R_e}$, $\overline{\log \sigma}$, and $\overline{SB_e}$ of the sample

$$ZP = \overline{\log R_e} - \alpha \overline{\log \sigma} - \beta \overline{SB_e}. \tag{2}$$

Based on the assumption of homology, the existence of a FP implies that the ratio of the total mass to luminosity (M/L) scales with σ and R_e. Since the galaxy M/L depends on both the star formation history of the galaxies and the cosmology, the study of

the FP is a valuable tool for studying the evolution of the stellar population in early-type galaxies.

Several studies of intermediate ($z \sim 0.3$) and high-redshift ($z \sim 0.85$) clusters of galaxies have used the ZP shift of the plane to estimate the average formation redshifts of stars in early-type galaxies (e.g., Bender et al. 1998; van Dokkum et al. 1998; Jørgensen et al. 1999; Kelson et al. 2000; van Dokkum & Stanford 2003; Wuyts et al. 2004; Jørgensen et al. 2006). In general, they have all found values compatible with a redshift formation greater than 3. In the field, early studies found slow evolution, compatible with that in clusters (e.g., van Dokkum et al. 2001; Treu et al. 2001; Kochanek et al. 2000). However, evidence of more rapid evolution in the field has been found by other authors (Treu et al. 2002; Gebhardt et al. 2003; Treu et al. 2005a). Taking into account the so-called progenitor bias (for which lower redshift early-type samples contain galaxies that have stopped their star formation only recently and that will not be recognised as early-types at higher redshifts) forces a revision to slightly lower formation redshifts (van Dokkum & Franx 2001, $z \approx 2$).

The current view is that both the evolution of early-type galaxies with redshift and the dependence of this evolution on environment differ for galaxies of different mass. These differences manifest themselves as an evolution in the FP coefficient α at increasing redshift, from 1.2 (in the B band) at redshift 0.0 to 0.8 at $z \sim 0.8-1.3$ (van der Wel et al. 2004; Treu et al. 2005a,b; van der Wel et al. 2005; di Serego Alighieri et al. 2005; Holden et al. 2005; Jørgensen et al. 2006). However, this change in the slope has not been observed at $0.2 < z < 0.8$ (e.g., van Dokkum & Franx 1996; Kelson et al. 2000; Wuyts et al. 2004; van der Marel & van Dokkum 2007b; MacArthur et al. 2008). If interpreted as a M-M/L ratio relation, this rotation of the FP indicates that there is a greater evolution in the luminosity of low-mass galaxies with redshift. This interpretation was however questioned by van der Marel & van Dokkum (2007b). Dynamical models provide little evidence of a difference in M/L evolution between low- and high-mass galaxies, and the steepening of the FP may be affected by issues other than M/L evolution, such as an increasing importance of internal galaxy rotation at lower luminosities, not captured by the simple aperture-corrected velocity dispersion used in Eq. (1) (Zaritsky et al. 2008), superimposed on the well known change with redshift in the fraction of S0 galaxies contributing to the early-type population (Dressler et al. 1997; Desai et al. 2007; Just et al. 2010). This so-called rotation of the FP, or change in the tilt of the FP, was originally found in field samples, but Jørgensen et al. (2006) claimed that is also exists for cluster galaxies at $z = 0.89$.

Most studies of evolution with redshift in cluster early-type galaxies have concentrated on single clusters. It remains unclear whether early-type galaxies in clusters at the same redshift share the same FP, or whether the FP coefficients vary systematically as a function of the global properties of the host cluster (e.g., richness, optical and X-ray luminosity, velocity dispersions, concentration, and subclustering). D'Onofrio et al. (2008) demonstrated that the universality of the FP has yet to be proven and that to avoid causing any biases by comparing the FP relation of clusters at different redshifts a larger number of clusters should be studied.

Furthermore, the ZP evolution of the FP with redshift has been interpreted as an evolution in the M/L ratio. However, this may not be entirely true if there is a structural evolution in the size of the galaxies. At face value, observations seem to show that the most massive ($M_* > 10^{11}\ M_\odot$) spheroid-like galaxies at $z > 1.5$, irrespective of their star-formation activity

(Pérez-González et al. 2008) were much smaller (a factor of ~4) than their local counterparts (Daddi et al. 2005; Trujillo et al. 2006, 2007; Longhetti et al. 2007; Zirm et al. 2007; Toft et al. 2007; Cimatti et al. 2008; van Dokkum et al. 2008; Buitrago et al. 2008; Saracco et al. 2009; Damjanov et al. 2009; Ferreras et al. 2009). van Dokkum et al. (2010) argue that the growth in size with decreasing redshift is due to the progressive build-up of the outer ($R > 5$ kpc) stellar component of galaxies, while the inner core is already in place at redshift ≈ 2. We note also that these conclusions have been questioned by Mancini et al. (2010), who find evidence for galaxies as large as local ones at redshifts higher than 1.4. Complementing our discussion above about the evolution of the zero point of the FP, if galaxy size were to vary with redshift, we should expect an accompanying partial revision of the importance of the effect of galaxy size evolution when taking into account the progenitor bias (Valentinuzzi et al. 2010a). Finally, if a variation in galaxy size with redshift were to occur, we should expect an accompanying increase in the central velocity dispersion with redshift (Cenarro & Trujillo 2009; van Dokkum et al. 2009). The evolutions both in size and velocity dispersion are predicted by theoretical models that take into account internal feedback "puffing" mechanisms (Biermann & Shapiro 1979; Fan et al. 2008) or the effect of merging (Khochfar & Silk 2006; Hopkins et al. 2009). As one can read from Eq. (2), a change in $\overline{\log R_e}$, $\overline{\log \sigma}$, and $\overline{SB_e}$ with redshift due to structural evolution will change the amount of stellar population evolution needed to explain the ZP variation and therefore needs to be taken into account when deriving constraints on the formation epoch of early-type galaxies.

In this paper, we present the evolution of the FP for a sample of 154 spectral early-type galaxies in 28 clusters or groups and 62 in the field using spectra and images from the ESO Distant Cluster Survey of galaxies (White et al. 2005, EDisCS). The clusters have redshifts between ~0.4 and 0.9 and velocity dispersions between 166 and 1080 km s^{-1} (Halliday et al. 2004; Clowe et al. 2006; Milvang-Jensen et al. 2008). Our clusters have generally lower velocity dispersions than those typically studied at similar redshifts and represent an intermediate-redshift sample for which a majority of the clusters may be progenitors of typical low-redshift clusters (see Poggianti et al. 2006; Milvang-Jensen et al. 2008).

The paper is organized as follows. Section 2 presents the data set. In particular, Sect. 2.1 describes the measurements of the galaxy velocity dispersions. Section 2.2 describes the measurement of the structural parameters, their errors, and the photometric calibration. Section 2.3 characterizes the statistical properties of the sample. Section 3 presents the FP of EDisCS galaxies. We start in Sect. 3.1 with the FP for 25 clusters and discuss the evolution of the FP zero point as a function of redshift and cluster velocity dispersion. Section 3.2 considers the differences between the FP of galaxies in clusters and the field and the dependence on galaxy mass. Section 3.3 discusses the related problem of the rotation of the FP. In Sect. 4, we consider the size evolution of galaxies and how this affects the stellar population time-dependence implied by the evolution of the FP. In Sect. 5, we draw our conclusions. Appendix A explains in detail how we compute circularized half-luminosity radii. Throughout the paper, we assume that $\Omega_M = 0.3$, $\Omega_\Lambda = 0.7$, and $H_0 = 70$ km s^{-1} Mpc^{-1}.

2. Data analysis

The sample of galaxies analyzed in this paper consists of spectroscopic early-type objects. We considered the flux-calibrated

spectra reduced in Halliday et al. (2004) and Milvang-Jensen et al. (2008) of galaxies with early spectral type (1 or 2). This indicates the total absence (type 1) or the presence of only weak (with equivalent width smaller than 5 Å) [OII] lines (Sánchez-Blázquez et al. 2009). We derive galaxy velocity dispersions from these spectra (Sect. 2.1). We match this dataset with HST and VLT photometry (Sect. 2.2). The HST images (Desai et al. 2007) provide visual classification and structural parameters for 70% of our galaxies. For the remaining 30%, we use VLT photometry, where no visual classification is available (Simard et al. 2009). Approximately 70% of the galaxies with HST photometry have early-type morphologies (Sect. 2.3).

2.1. Velocity dispersions

Velocity dispersions were measured in all galaxy spectra using the IDL routine pPXF (Cappellari & Emsellem 2004). This routine is based on a maximum penalized likelihood technique that employs an optimal template, and also performs well when applied to spectra of low signal-to-noise ratio (Cappellari et al. 2009). The algorithm works in pixel space, estimating the best fit to a galaxy spectrum by combining stellar templates that are convolved with the appropriate mean galaxy velocity and velocity dispersion. The results depend critically on how well the spectra are matched by the template. To compile an optimal template, we use 35 synthetic spectra from the library of single stellar-population models of Vazdekis et al. (2010), which uses the new stellar library MILES (Sánchez-Blázquez et al. 2006). These spectra were degraded to the wavelength-dependent resolution of the EDisCS spectra, determined from the widths of the lines in the arc lamp spectra, slit by slit, which match well the widths of the sky lines in the science spectra.

The library contains spectra spanning an age range from 0.13 to 17 Gyr and metallicities from [Z/H] = −0.68 to [Z/H] = +0.2. Operating in pixel space, the code allows the masking of regions of the galaxy spectra during the measurements. We use this to mask regions affected by skyline residuals. Although the code allows the measurement of the higher Gauss-Hermite order moments (Bender et al. 1994), we only fit the velocity and σ, which helps to stabilise the fits in our spectra of low signal-to-noise ratio. Errors were calculated by means of Monte Carlo simulations in which each point was perturbed with the typical observed error, following a Gaussian distribution. Because the template mismatch affects the measurement of the velocity and σ determined with pPXF, a new optical template was used in each simulation. The errors were assumed to be the standard deviation in measurements inferred from 20 simulations. Owing to limitations caused by the instrumental resolution, only velocity dispersions larger than 100 km s^{-1} are reliable and unbiased. Therefore, galaxies with smaller σ, as well as velocity dispersions with uncertainties larger than 20%, the approximate intrinsic scatter of the local FP (see Introduction), are not be considered any further.

We note that the velocity dispersions measured here are ≈10% lower than those given in Sánchez-Blázquez et al. (2009). The difference is caused by the instrumental resolution in that paper having been assumed to be constant with wavelength at the value of 6 Å. In reality, this is only the optimal resolution possible with our setup, which can be as large as 8 Å. The change is important here, but does not affect any of the results presented in Sánchez-Blázquez et al. (2009).

We measured velocity dispersions for 192 cluster and 78 field galaxies. Figure 1 shows the histograms of the statistical
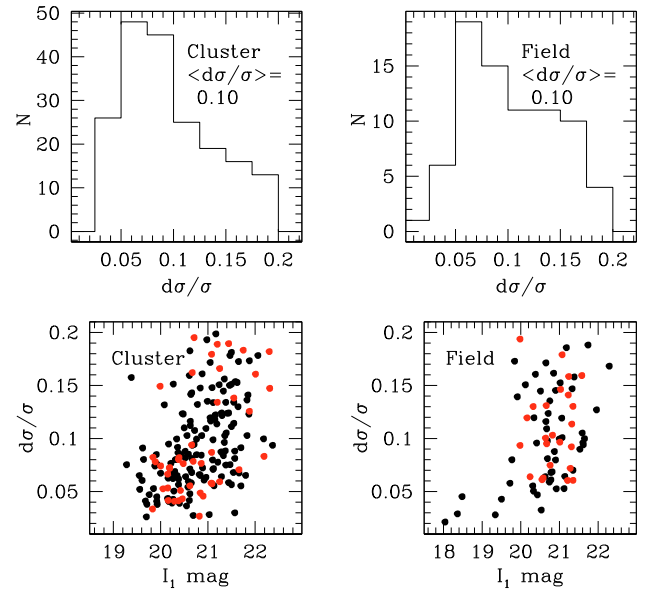

Fig. 1. The velocity dispersion errors. *First row*: the histograms of statistical errors on velocity dispersions. *Second row*: the statistical errors as a function of apparent *I* band magnitude in a 1 arcsec radius aperture. Colors code the spectroscopic type (black: 1; red: 2).

errors. The statistical errors are on average 10% and are a function of magnitude.

The systematic errors are more difficult to estimate, as they depend on the template mismatch, continuum variations, and filtering schemes. They have been extensively studied in the past (Cappellari & Emsellem 2004) and can be as large as 5−10%. To determine the size of the systematic errors, we derived the galaxy velocity dispersions using the FCQ method of Bender et al. (1994), which is less prone to template mismatching systematics and operates in Fourier space. We focused on the *G* band region at $z \approx 0.5$, the Mgb region at lower redshifts, or the largest available continuous range redder than the 4000 Å break, similar to the approach of Ziegler et al. (2005). The two methods agree well, with 68% of the values differing by less than the combined 1-σ error, and 96% by less than 3-σ, but smaller errors are derived using the pixel fitting approach, partially because most of each spectrum can be used. This allows us to conclude that our residual systematic errors are always smaller than the statistical ones.

Finally, an aperture correction following Jørgensen et al. (1995)

$$\log \sigma_{cor} = \log \sigma_{mes} + 0.04 * \log(Ap/3.4 \text{ kpc}), \tag{3}$$

where Ap represents the average aperture of our observations, 1.15 arcsec, scaled with the distances of the objects, was applied to the measured velocity dispersions σ_{mes} to place them on the Coma cluster standard aperture system of 3.4 kpc. Figure 2 shows that, on average, this correction amounts to 3% with ≈0.5% spread. From this point on, we drop the *cor* and indicate with σ the aperture-corrected value of the velocity dispersion.

Figure 3 presents the velocity dispersions as a function of redshift and their distribution. On average, the galaxy velocity dispersion is ≈200 km s^{-1}, with a mildly increasing trend with redshift. Weighting each galaxy by the inverse of its completeness value (see Sect. 2.3) in general changes the mean by no more than its error.
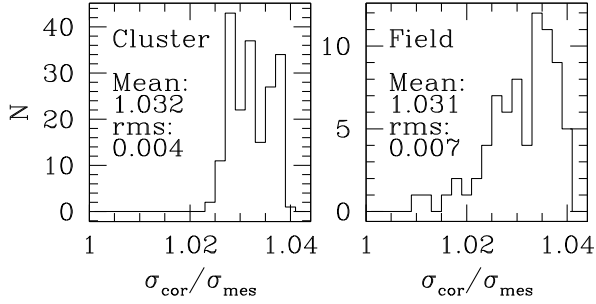
Fig. 2. The histogram of the fractional aperture corrections $\sigma_{cor}/\sigma_{mes}$ for cluster (*left*) and field (*right*) galaxies.
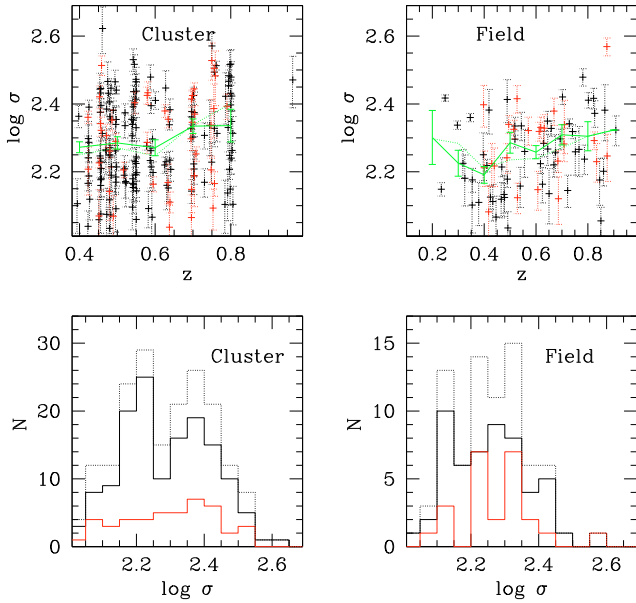

Fig. 3. The velocity dispersions of the galaxy sample. *Top*: the measured galaxy velocity dispersions as a function of redshift in clusters (*left*) and the field (*right*). The green lines show the mean values in 0.1 redshift bins and the relative errors. The dotted lines show the mean values weighting each galaxy with the inverse of its completeness value. *Bottom*: the histogram of galaxy velocity dispersions in clusters (*left*) and the field (*right*). Colors code the spectral type (black: 1; red:2). The dotted lines show the histogram for the entire sample irrespective of spectral type.

2.2. Photometry

The photometric part of the FP, i.e., the half-luminosity radius R_e and average effective surface brightness $\langle SB_e \rangle = -2.5 \log \frac{L}{2\pi R_e^2}$, where L is the total luminosity, was derived by fitting either HST ACS images (Desai et al. 2007) or I-band VLT images (White et al. 2005) using the GIM2D software (Simard et al. 2002). Simard et al. (2009) provide an extensive description of the methods and tests performed to assess the accuracy of the derived structural parameters, using exhaustive Monte Carlo simulations. To summarize, a two-component two-dimensional fit was performed, adopting an $R^{1/4}$ bulge plus an exponential disk convolved to the PSF of the images. From the parameters of the fit, we measured the (circularized) R_e and effective surface brightness from curves of growth constructed from the best-fit models using the procedure described in Appendix A.
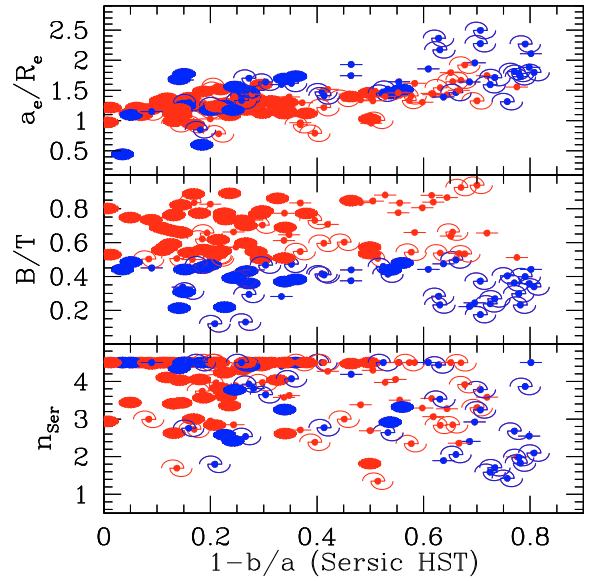
Fig. 4. The properties of the bulge+disk fits to galaxies with HST photometry and a measured velocity dispersion. We plot the ratio a_e/R_e of the semi-major effective scale length a_e of the best-fit Sersic profile to the circularized effective radius R_e of the best-fit B+D model (*top*), the bulge-to-total ratio B/T (*middle*), and the Sersic index n_{Ser} (*bottom*) as a function of the ellipticity $1 - b_e/a_e$ (where b_e is the semi-minor effective scale length) of the Sersic fit. Objects with $B/T > 0.5$ are plotted in red, the remainder in blue. Symbols code the morphology: filled ellipses show $T \leq -4$, filled circles crossed by a line $-3 \leq T \leq 0$, spirals $T > 0$.

Historically, effective radii were derived from fits to curves of growths, constructed from photoelectric photometry using circular apertures of increasing sizes (Burstein et al. 1987). Our procedure reproduces this approach and is identical to that followed by Gebhardt et al. (2003) to study the evolution of the FP of field galaxies with redshift. We prefer it to less sophisticated approaches (such as the straight $R^{1/4}$ fit often used in the literature) as it provides far superior fits to the images. As Gebhardt et al. (2003) do, we note that in the past a variety of methods have been adopted to measure the structural parameters that enter into the FP: curve of growth, isophotal photometry, or 2-dimensional fitting, pure $R^{1/4}$, Sersic, or bulge+disk (B+D) functions. The derived effective radii and surface brightness, however, when combined in Eq. (1) of the FP, deliver the same ZP to a high degree of accuracy (Saglia et al 1993). This has been proven for a large set of local clusters, including the Coma cluster (Saglia et al. 1997b; de Jong et al. 2004), and remains valid for the present data set (see below). This justifies the comparisons with FP samples from the literature presented below.

We later use effective radii to probe the size evolution of galaxies. Without a doubt, the scale length along the major axis of a pure disk galaxy is the correct measurement of its size, and our circularized R_e progressively underestimates the effective semi-major axis length as the inclination increases (see Fig. 4). However, for a pure bulge the inverse is true, and our R_e then averages out projection effects, producing the equivalent circularized size of each spheroid.

On the other hand, both the resolution and signal-to-noise ratio of the images considered here are too low to allow us to perform an accurate and unbiased determination of the sizes of the bulge and the disk components separately for our galaxies. Since the percentage of disk-dominated, highly inclined objects

in the galaxy sample considered here is low, as it is in the low redshift comparison, we conclude that our choice is reasonable. In particular, the mean axial ratios of our sample and the low redshift comparison are identical, as discussed in Valentinuzzi et al. (2010b).

We now consider the quantitative question of the extent to which our procedure for computing structural parameters is equivalent to other approaches discussed in the literature.

In analogy with procedures followed for local galaxies (Saglia et al. 1997a), where systematic errors are gauged by comparing different photometric fits, we assess the robustness of the structural parameters to the chosen $R^{1/4}$ bulge plus exponential disk surface brightness model by considering a second two-dimensional fitting approach to the HST images. We fit a single-component Sersic profile (with $0.5 \leq n_{\rm Ser} \leq 4.5$) to the HST ACS imaging in the $F814W$ band, available for 10 of the EDisCS clusters. Again, the circularized half-luminosity radius $R_{\rm e}({\rm Ser})$ is computed from curves of growth constructed from the best-fit model as described in Appendix A.

Figure 4 summarizes the results of our B+D and Sersic fits. The galaxies of our HST sample have on average a flattening $1 - b_{\rm e}/a_{\rm e}$ of 0.37 (0.33 without spirals), with some disk-dominated, nearly edge-on spiral galaxies reaching $1 - b_{\rm e}/a_{\rm e} \approx 0.8$. As a consequence, our circularized effective radii are on average 39% (33% without spirals) smaller than the effective semi-major lengths $a_{\rm e}$. On average, our objects are bulge-dominated ($\langle B/T \rangle = 0.59$, 0.64 without spirals) and reasonably well described by a de Vaucouleurs law ($\langle n_{\rm Ser} \rangle = 3.7$, 3.9 without spirals).

Figures 5−7 (top and middle panels) assess the robustness of the derived structural parameters derived for the galaxies with measured velocity dispersions. For this purpose, we also consider the harmonic radius $R_{\rm har} = (a_{\rm e} b_{\rm e})^{1/2}$, often used in the literature as a proxy for $R_{\rm e}$ (sometimes fixing the Sersic index to 4, the $R^{1/4}$ law) and the related average surface brightness $\langle SB_{\rm e}^{\rm har} \rangle$, where $a_{\rm e}$ and $b_{\rm e}$ are the effective semi-major and minor axis of the Sersic fits. The evaluated harmonic and circularized Sersic radii are on average very similar to our adopted $R_{\rm e}$, as well as the resulting effective surface brightness. When combined into the quantity orthogonal to the FP $\log R_{\rm e} - 0.27 \langle SB_{\rm e} \rangle$, they show minimal systematic differences and scatter. As discussed in Appendix A, only at high flattening (i.e. for almost edge-on disk-dominated galaxies) do the harmonic quantities show the expected stronger deviations.

Figure 8 quantifies the differences $\delta \log R_{\rm e} = \log R_{\rm e}(B+D) - \log R_{\rm e}({\rm Sersic})$, $\delta \langle SB_{\rm e} \rangle = \langle SB_{\rm e} \rangle(B+D) - \langle SB_{\rm e} \rangle({\rm Sersic})$, and the direction orthogonal to the FP, $\delta FP = \delta \log R_{\rm e} - 0.27 \delta \langle SB_{\rm e} \rangle$ by showing their histograms, separately for cluster and field galaxies.

In summary, the median differences are small (the Sersic $R_{\rm e}$ are 9% larger, the Sersic effective surface brightnesses are ≈ 0.13 mag brighter). The widths at the 68% percentile of the distributions are $\delta_{68} \log R_{\rm e} \sim 0.07$, $\delta_{68} \langle SB_{\rm e} \rangle \sim 0.24$, and $\delta_{68} FP \sim 0.005$ for cluster and (slightly smaller for) field galaxies with measured velocity dispersions. Given the quality of our HST ACS images, we conclude that we measure the structural parameters of galaxies with a precision similar to that of local galaxies (Saglia et al. 1997b; de Jong et al. 2004).

For the remaining clusters with only ground-based images, we derive the structural parameters as described above (Simard et al. 2009), i.e., by fitting an $R^{1/4}$ bulge plus an exponential disk 2D model to the I-band VLT deep images that were obtained in excellent seeing conditions. Circularized half-luminosity radii are derived from curves of growth constructed from the best fits
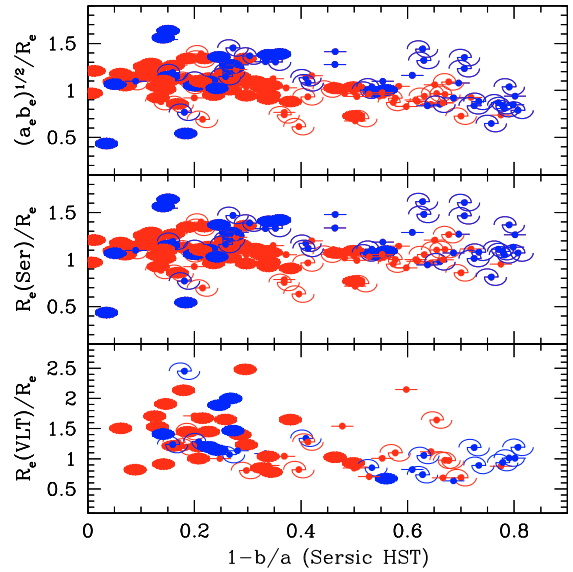
Fig. 5. The comparison between different estimations of the half-luminosity radii of all galaxies with HST photometry and a measured velocity dispersion. We plot the ratio of the harmonic radius $(a_{\rm e} b_{\rm e})^{1/2}$ to the circularized effective radius $R_{\rm e}$ of the best-fit HST B+D model (top), the ratio of the circularized effective radius $R_{\rm e}({\rm Ser})$ of the Sersic fit to $R_{\rm e}$ (middle), and the ratio of the circularized effective radius $R_{\rm e}({\rm VLT})$ of the best-fit VLT B+D model to $R_{\rm e}$ (bottom) as a function of $1 - b_{\rm e}/a_{\rm e}$. Symbols and color coding are as in Fig. 4.
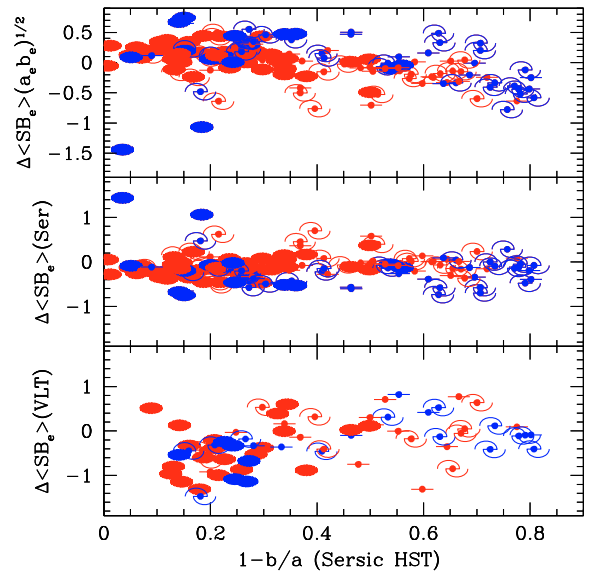
Fig. 6. The comparison between different estimates of the effective surface brightness of all galaxies with HST photometry and a measured velocity dispersion. We plot the difference $\Delta \langle SB_{\rm e}(a_{\rm e} b_{\rm e}) \rangle$ between the average surface brightness within $(a_{\rm e} b_{\rm e})^{1/2}$ and $R_{\rm e}$ (top), the difference $\Delta \langle SB_{\rm e}({\rm Ser}) \rangle$ between the average surface brightness within $R_{\rm e}({\rm Ser})$ and $R_{\rm e}$ (middle), and the difference between the average surface brightness within $R_{\rm e}(VLT)$ and $R_{\rm e}$ (bottom) as a function of $1 - b_{\rm e}/a_{\rm e}$. Symbols and color coding are as in Fig. 4.

as described in Appendix A. In general, simulations show that the structural parameters derived from the fits to VLT images are of reasonably good precision when nearly-isolated galaxies (i.e., those for which the segmentation area has little contamination

Fig. 7. The comparison between different estimations of the quantity $FP = \log R_e - 0.27\langle SB_e\rangle$ for all galaxies with HST photometry and a measured velocity dispersion. We plot $\Delta FP(a_e b_e)^{1/2} = \log((a_e b_e)^{1/2}/R_e) - 0.27(\langle SB_e\rangle(a_e b_e)^{1/2}) - \langle SB_e\rangle)$ (*top*), $\Delta FP = \log(R_e(\mathrm{Ser})/R_e) - 0.27(\langle SB_e\rangle(\mathrm{Ser}) - \langle SB_e\rangle)$ (*middle*), and $\Delta FP = \log(R_e(VLT)/R_e) - 0.27(\langle SB_e\rangle(VLT) - \langle SB_e\rangle)$ (*bottom*) as a function of $1 - b_e/a_e$. Symbols and color coding are as in Fig. 4.
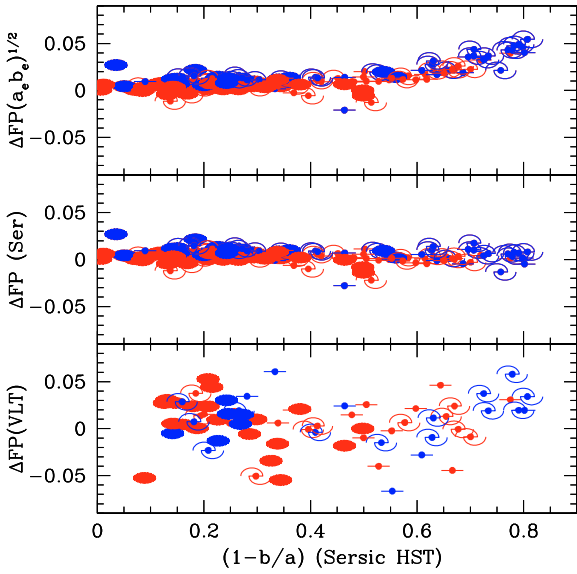

Fig. 8. The quality of the photometry parameters derived from HST images for cluster (*left*) and field (*right*) galaxies. We show histograms of the differences between structural parameters derived from bulge plus disk (B+D) and Sersic GIM2D fits to the HST ACS images of the galaxies with measured velocity dispersions. The mean, rms, and the widths at the 68% percentile of the distributions are given.

from nearby objects) are considered. Statistical errors smaller than 0.27 mag in total magnitudes and smaller than 0.36 dex in $\log R_e$ are derived, in addition to systematic errors smaller than 0.15 mag and 0.2 dex, respectively, if bright objects (Imag < 22.5) are examined (Simard et al. 2009). The galaxies in our sample are typically at least one magnitude brighter than this limit.

The bottom panels of Figs. 5–7 show the comparison of the VLT-derived structural parameters with the HST-derived structural parameters as a function of galaxy flattening, while Fig. 9 shows the histograms of the differences $\delta \log R_e = \log R_e(HST) - \log R_e(VLT)$, $\delta\langle SB_e\rangle = \langle SB_e\rangle(HST) - \langle SB_e\rangle(VLT)$, and $\delta FP = \delta \log R_e - 0.27\delta\langle SB_e\rangle$ for objects with measured velocity dispersions where HST images are also available. For cluster objects that are isolated or have only relatively small companions (SExtractor flags 0 or 2, Bertin & Arnouts 1996), the comparison is reasonable, with median $\langle\delta \log R_e\rangle_{\mathrm{med}} \sim -0.08$, $\delta_{68} \log R_e \sim 0.14$, (i.e., VLT half-luminosity radii are on average 20% larger than HST R_e with ≤25% scatter), and median difference $\langle\delta\langle SB_e\rangle\rangle_{\mathrm{med}} \sim -0.32$, $\delta_{68}\langle SB_e\rangle \sim 0.53$ (i.e., VLT effective surface brightnesses are on average 0.32 mag brighter than those from HST $\langle SB_e\rangle$ with ≤0.53 mag scatter). The errors $\delta \log R_e$ and $\delta\langle SB_e\rangle$ are correlated, with minimal scatter in the direction almost orthogonal to the FP, i.e., $\delta FP = \delta \log R_e - 0.27\delta\langle SB_e\rangle$ and $\delta_{68}FP \sim 0.025$ and there is a small median shift. No trend with redshift is seen. These values agree with or are of higher precision than those derived from simulations (see above). Very similar results are obtained for field objects. Therefore, the VLT dataset can be merged with the HST-based one to study the evolution of the FP (Sect. 3).

The systematic and random errors increase dramatically if objects with sizable companions (VLT SExtractor flag 3) are considered. In these cases, the VLT segmentation areas fitted by GIM2D are heavily contaminated by the companions. As a

consequence, $R_e(VLT)$ and VLT total magnitudes are systematically larger and brighter, respectively, than those derived from HST fits. There are 38 cluster and 10 field galaxies with early spectral type and measured velocity dispersion that have only VLT imaging and a SExtractor flag equal to 3. Given the already sizeable systematics in R_e detected for the "isolated" objects, we refrain from attempting an iterative fit and just exclude the affected galaxies from the FP analysis.

In Sect. 4, we use the half-luminosity radii discussed above to constrain the size evolution of our galaxies. The high-precision (≈10% systematic) HST half-luminosity radii are certainly good enough and our results are based on this dataset only. A number of caveats have to be kept in mind when considering the VLT radii. According to the Monte Carlo simulations discussed by Simard et al. (2009, Fig. 1), the VLT radii of the largest galaxies of the sample (larger than 1.8 arcsec) may underestimate the true radii by up to 40%. But only 2.5% of our sample has $R_e > 1.8''$. Sizes smaller than 0.1 arcsec are probably unreliable because of the limits to our resolution, but only 3% of cluster galaxies and 5% of field galaxies fall into this category. Finally, if galaxies have strong color gradients, our half-luminosity radii, derived from I band images (i.e., approximately rest-frame V band at redshift 0.5 and rest-frame B band at redshift 0.8) might be affected differentially with redshift. However,
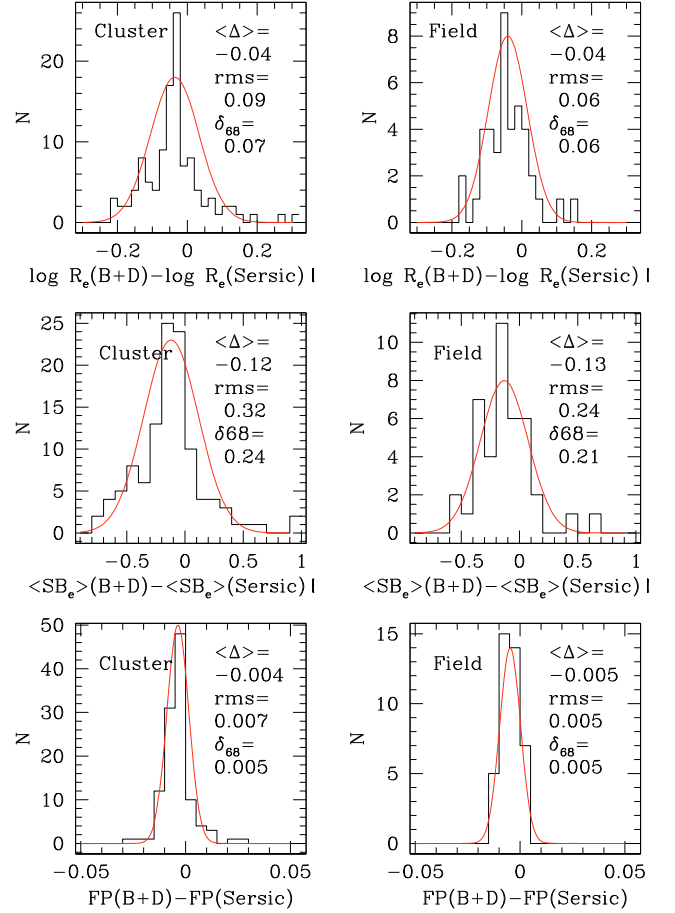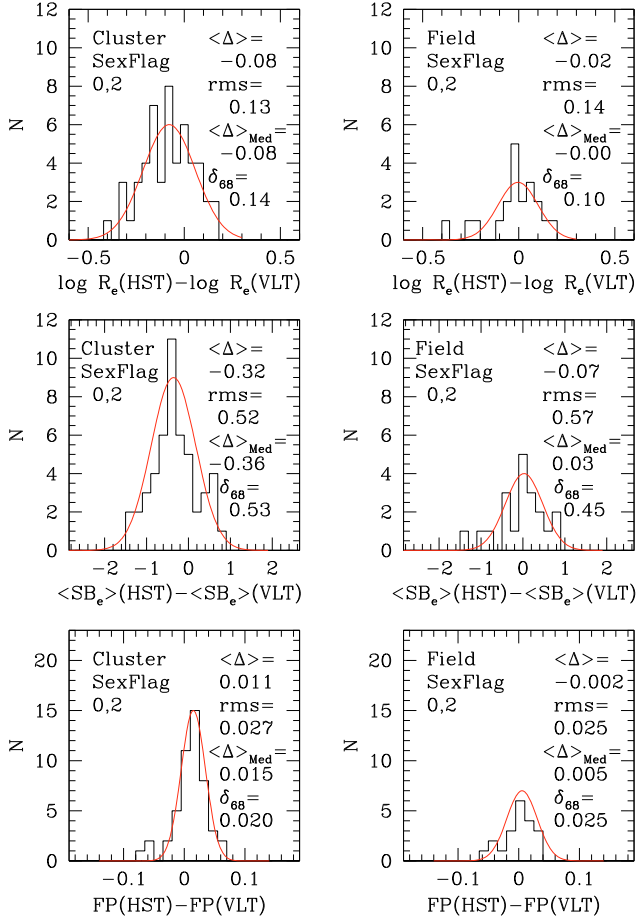
Fig. 9. The quality of the photometry parameters derived from VLT images for cluster (*left*) and field (*right*) galaxies. Histograms of the differences between structural parameters derived from bulge plus disk GIM2D fits to the HST ACS and VLT *I* band images of the isolated, undisturbed galaxies with measured velocity dispersions. The mean, rms, and the widths at the 68% percentile of the distributions are given.

we do not detect any significant trend with redshift in the sizes derived from our VLT *B* and *V* band images relative to the ones used here from the *I* band images. Despite all these systematic differences between HST and VLT R_e radii (on average 20%), Sect. 4 shows that the size evolution derived from VLT R_e radii is very similar.

As a last step, effective surface brightnesses were calibrated as follows. Corrections to rest-frame Johnson *B* band were applied based on the spectroscopic redshift *z* and an interpolation of the best-fit spectral energy distribution, using our photometric redshift procedure (Rudnick et al. 2009; Pelló et al. 2009). Moreover, the Tolman correction $(1+z)^4$ was taken into account. Finally, to be able to compare our results with those of Wuyts et al. (2004) and related papers, we transformed effective surface brightness to surface brightness at R_e using a conversion factor that is valid for a pure $R^{1/4}$ law, i.e., $I_e = \langle I_e \rangle / 3.61$ and $\log \langle I_e \rangle (L_\odot/\mathrm{pc}^2) = -0.4(\langle SB_e \rangle - 27)$.

Figure 10 shows $\log R_e$, $\log I_e$, and dynamical mass $\log M_{\mathrm{dyn}}$ as a function of redshift. Following van Dokkum & van der Marel (2007), we compute dynamical masses to be

$$M_{\mathrm{dyn}} = 5 R_e \sigma^2 / G = 1.16 \times 10^6 (R_e/\mathrm{kpc}), \times (\sigma/\mathrm{km\,s^{-1}})^2\ M_\odot \quad (4)$$

(see also Sect. 3.2). The mean size of the half-luminosity radius remains approximately constant at values of ≈ 2.5 kpc. In
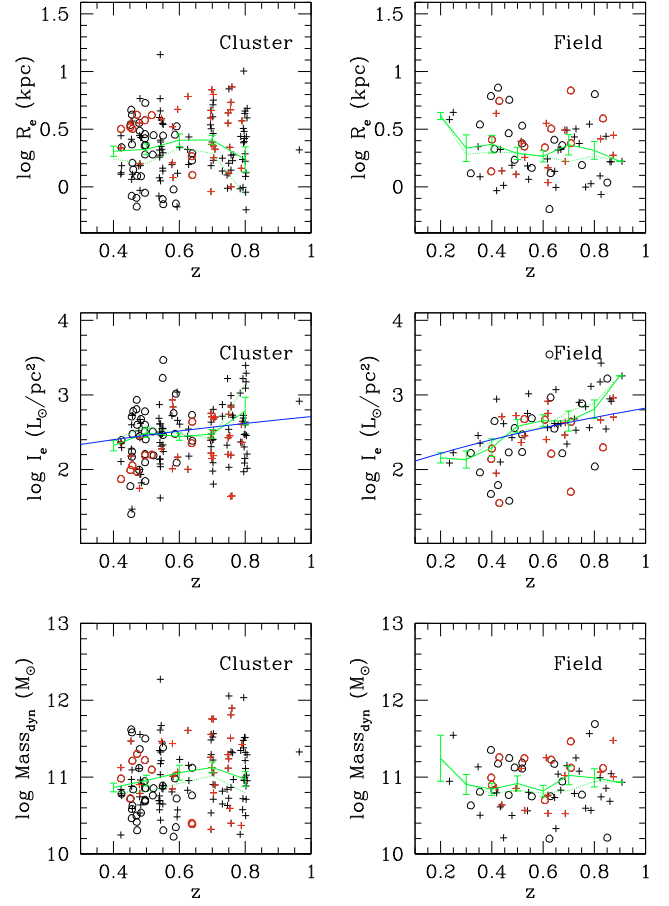
Fig. 10. The distribution with redshift of sizes, surface luminosities, and dynamical masses of the galaxy sample. We show the half-luminosity radii $\log R_e$ (*top*), effective surface brightness $\log I_e$ (*middle*), and dynamical mass $\log M_{\mathrm{dyn}}$ (*bottom*) as a function of redshift for cluster (*left*) and field (*right*) galaxies. Black and red points show spectroscopic types 1 and 2, respectively. Crosses and circles show galaxies with HST and VLT photometry, respectively. The solid green lines show the mean values in 0.1 redshift bins with the errors. The dotted lines show the averages obtained by weighting each galaxy with the inverse of its selection value. The blue lines show the mean luminosity evolution derived from Fig. 17: $\log I_e = 2.4 + 1.66 \log \frac{1+z}{1.4} / 0.83$ for cluster galaxies and $\log I_e = 2.4 + 2.27 \log \frac{1+z}{1.4} / 0.83$ for the field.

contrast, the surface brightness at R_e increases on average by a factor 2 from redshift 0.4 (where it is $\approx 250\ L_\odot/\mathrm{pc}^2$) to redshift 0.8. This matches the differential luminosity evolution inferred from the FP zero-point evolution with redshift (see Sect. 3.1). Weighting each galaxy with the inverse of its selection value to correct for incompleteness (see Sect. 2.3) pushes the sample averages of $\log R_e$ and $\log I_e$ to slightly lower and higher values, respectively. As for the velocity dispersions, the effect is however on the order of the error in the averages. We note that the situation changes when we consider the size evolution of mass-selected samples (see Sect. 4). We study cluster galaxies with dynamical masses higher than $1.5 \times 10^{10}\ M_\odot$ and field galaxies with dynamical masses higher than $2.5 \times 10^{10}\ M_\odot$. Both cluster and field galaxies have on average a dynamical mass of $10^{11}\ M_\odot$.
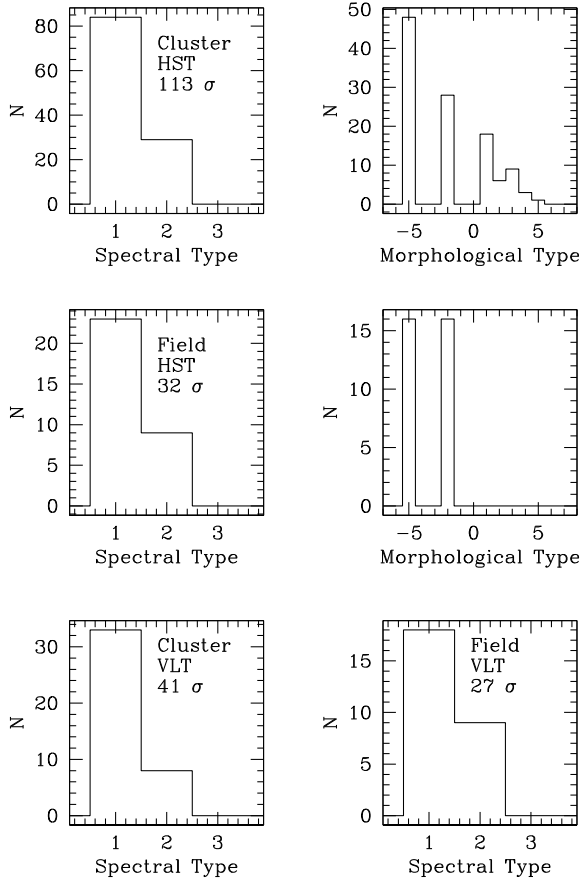
Fig. 11. Statistics of the sample of galaxies with measured velocity dispersions and photometric parameters.

Fig. 12. The relative completeness functions. The fraction of galaxies with an observed spectrum of spectroscopic type 1 or 2 for which we could measure velocity dispersions and obtain reliable photometric structural parameters. This relative completeness is shown for the clusters (*top row*) and the field (*bottom row*) as a function of galaxy magnitude in the *I* band in a 1 arcsec radius aperture. Colors code the spectral type (black: 1; red: 2). The full lines indicate the full redshift range, the dotted lines galaxies with $z < 0.6$, and the dashed lines galaxies with $z \geq 0.6$. The dots show the magnitudes of the single galaxies and the assigned completeness weight.

2.3. Selection function

Figure 11 describes the final sample. We measured velocity dispersions for 113 cluster and 41 field spectral early-type galaxies with HST photometry, and 41 cluster and 27 field galaxies with only VLT good photometry. A large fraction of galaxies with HST photometry also have early-type morphology: 67% of the objects in clusters and 78% in the field were classified as either Es or S0. Moreover, 77% of galaxies in clusters and 68% in the field do not exhibit [OII] emission, being of spectral type 1.

To quantify the selection function of our sample, we assign a selection probability P_S to each galaxy. This is computed in two steps. First, the σ-completeness probability P_σ of the velocity dispersion measurements is determined. This is shown in Fig. 12. For each given spectral type, we compute the ratio of the number of galaxies with a measured velocity dispersion and reliable photometric structural photometry (see above) to the number of galaxies with a spectrum in a given magnitude bin. In a way similar to Milvang-Jensen et al. (2008), we use the *I* band magnitude in a 1 arcsec radius aperture I_1. We compute these curves separately for cluster and field galaxies, and for galaxies with redshifts either equal to or lower than or higher than 0.6. Finally, we assign the probability $P_\sigma(I_1, z, ST, F/C)$ to each galaxy by linearly interpolating the appropriate curve for its redshift z, spectral type ST, and field or cluster environment (F/C) as a function of magnitude. The σ-completeness is high at bright magnitudes and declines toward fainter objects. In this regime, the σ completeness is also slightly higher for higher redshift galaxies, where the exposure times are longer.

The differences between cluster and field galaxies are not as pronounced.

As a second step, following Milvang-Jensen et al. (2008) we consider the total number of spectroscopically targeted galaxies N_T (drawn from a photometric magnitude-limited sample far deeper than that considered here; see Milvang-Jensen et al. 2008) in a given magnitude bin, separately for each of the 19 fields we observed. In the given field, we then consider the number of galaxies for which we were able to derive a secure redshift N_R (with a success rate of essentially 100%; see Milvang-Jensen et al. 2008), the number of galaxies spectroscopically found to be members of any cluster N_C, and the number of galaxies found in the field, $N_F = N_R - N_C$. We construct the ratio functions $R_C = \frac{N_C}{N_T}$ and $R_F = \frac{N_R - N_C}{N_T}$ and interpolate them at the magnitude of each galaxy. Finally, we assign to each galaxy the selection probability $P_S(\text{Cluster}) = P_\sigma \times R_C$ or $P_S(\text{Field}) = P_\sigma \times R_F$ if the galaxy belongs to a cluster or to the field.

Figure 13 shows the resulting probabilities as a function of I_1 and dynamical mass (see Eq. (4) and Sect. 3.2). In clusters, we sample between 10% and 30% of the spectral early-type population. The selection probability is almost flat as a function of mass for $M_{\rm dyn} \geq 4 \times 10^{10} \, M_\odot$. This is above the stellar mass completeness limit of our parent stellar catalogue. In this mass range, the selection probability has no dependence on the galaxy colors. We become progressively more incomplete at lower masses, where we sample just 10% of the population. The effect is less pronounced at higher redshifts. In the field, the average completeness is lower ($\approx 15\%$) and similar trends are observed. In general, P_σ traces P_S quite well, with $P_S \approx (0.29 \pm 0.12) P_\sigma$. In the abstract and in the following, we quote first results obtained by ignoring selection effects, and then illustrate the effect of the selection correction.
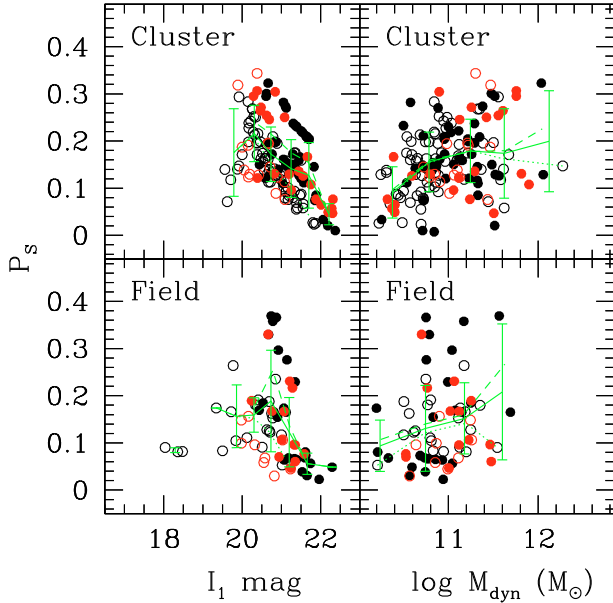
Fig. 13. The completeness function of the galaxy sample. The completeness weight for the galaxies with a velocity dispersion for clusters (top row) and the field (*bottom row*). *Left*: as a function of galaxy magnitude in the *I* band in a 1 arcsec radius aperture; *right*: as a function of dynamical mass. Colors code the spectral type (black: 1; red: 2). Filled circles show galaxies with redshift either equal to or higher than 0.6, open circles galaxies with redshift lower than 0.6. The green full lines with error bars show the bin averages and rms over the full redshift range. The dotted lines refer to the sample with $z < 0.6$, the dashed lines to the sample with $z \geq 0.6$.

Tables 1 and 2 summarize the velocity dispersions and the structural parameters of the cluster and field galaxies, respectively. For each galaxy, we list its name (White et al. 2005), the number of the cluster to which it belongs (if it is a cluster galaxy, see Table 4 for the correspondence between cluster name and number), spectroscopic redshift and type (Halliday et al. 2004; Milvang-Jensen et al. 2008), raw and aperture-corrected velocity dispersion $\sigma_{\rm mes}$ and $\sigma_{\rm cor}$ with estimated statistical error, circularized half-luminosity radius $R_{\rm e}$, surface brightness $\log I_{\rm e}$ in the rest-frame *B*-band, and, when HST images are available, morphological type. When VLT-only images are available, the morphological flag is set to be ∗ when the SExtractor flag is equal to 3, i.e., when the photometric parameters are expected to be contaminated by companions. Moreover, we list the selection probabilities $P_{\rm S}$ and the stellar masses (see Sect. 3.2). In addition, Table 3 gives the circularized $R_{\rm e}$ and $\log I_{\rm e}$ derived from Sersic fits (to HST images) and bulge+disk fits to VLT images for the galaxies for which both HST and VLT images are available.

3. The fundamental plane of the EDisCS galaxies

3.1. The FP of EDisCS clusters

Figure 14 shows the FP of the 14 EDisCS clusters with HST photometry, while Fig. 15 provides the FP of the additional 12 clusters with VLT-only photometry. In each cluster, good FP parameters are available for only a small number of galaxies (<9), the exceptions being cl1232.5-1144, cl1054.4-1146, cl1054.7-1245, and cl1216.8-1201. Therefore, at this stage we do not attempt to fit the parameters of the FP except for the zero point, keeping the velocity dispersion and surface brightness slopes fixed to the

local values ($\alpha_0 = 1.2$, $\beta_0 = -0.83/(-2.5) = 0.33$, Wuyts et al. 2004). In Sect. 3.3, we argue that this is a good approximation up to redshift 0.7. Following van Dokkum & van der Marel (2007), we compute the zero point as

$$ZP = \Sigma w (1.2 \log \sigma ({\rm km\,s^{-1}}) - 0.83 \log I_{\rm e}(L_\odot/{\rm pc^2})$$
$$- \log R_{\rm e}({\rm kpc}))/\Sigma w, \qquad (5)$$

where the sum comprises all N galaxies in a cluster with measured velocity dispersion, early spectroscopic type (1 or 2), and (for clusters with only VLT photometry) SExtractor flag 0 or 2, irrespective of morphology. At this stage, we weight each point by $w = (1/1.2{\rm d}\sigma)^2$, where ${\rm d}\sigma$ is the error in σ, and do not apply selection-weighting to be consistent with the procedures adopted in the literature and to minimize scatter. We note that this could generate systematic differences, given that the considered surveys have different selection functions. We explore below the influence of our selection function on the results. The error in the zero point is $\delta ZP = {\rm rms}(ZP)/\sqrt{N}$.

Following Wuyts et al. (2004), we use the Coma cluster as a reference point for the whole sample with $ZP = 0.65$. All past studies measuring the peculiar motions of the local universe of early-type galaxies (Lynden-Bell et al. 1988; Colless et al. 2001; Hudson et al. 2004, and references therein) agree with the conclusion that Coma, the richest and, in the FP context, the most well-studied local cluster, is at rest with respect to the cosmic microwave background and therefore the best suited as a reference. We convert the variation in the FP zero point into a variation in the mean mass-to-light ratio of galaxies in the *B* band with respect to Coma using the relation $\Delta \log M/L_B = (ZP - 0.65)/0.83$ (where $0.83 = \beta_0 \times 2.5$, see Eqs. (7) and (8)). We note that at this stage we still implicitly assume, as in the past, that no evolution in size or velocity dispersion is taking place. Figure 16, left, shows $\Delta \log M/L_B$ as a function of redshift. Only clusters with 4 or more ($N \geq 4$) galaxies are considered. Table 4 gives the relevant quantities: cluster number (Col. 1), cluster name (Col. 2, from Milvang-Jensen et al. 2008), cluster short name (Col. 3), type of photometry used (HST or VLT, Col. 4), cluster velocity dispersion (Col. 5), $\Delta \log M/L_B$ (Col. 6), scatter (Col. 7), and number of galaxies considered (Col. 8). Table 4 also lists the first six columns for the remaining clusters without FP ZPs. If we compute $\Delta \log M/L_B$ using the VLT photometry for the 12 clusters with both HST and VLT photometry, we derive a mean value $\Delta \log M/L_B(VLT - HST) = -0.04$ (-0.02 if two outliers, CL1354 and CL1138, are not considered) with an rms of 0.06 or an error in the mean of 0.02 (see also Sect. 3.2).

We add to the EDisCS sample 15 clusters from the literature (van Dokkum & van der Marel 2007), plus A370 from Bender et al. (1998). They span the redshift range $z = 0.109-1.28$ and sample the high cluster velocity dispersion ($\sigma_{\rm clus} > 800$ km s^{-1}) regime only. Moreover, as a common zero-redshift comparison we add the Coma cluster. A linear weighted fit to the whole sample gives $\Delta \log M/L_B = (-0.54 \pm 0.01)z$. Applying selection weighting reduces the slope to -0.47. A fit restricted to the literature sample alone gives -0.49 ± 0.02. Wuyts et al. (2004) derive -0.47, whereas van Dokkum & van der Marel (2007) find -0.555 ± 0.042. In view of the size evolution discussion of Sect. 4, where dependencies of $\log(1 + z)$ are considered, we also fit the slope η of the form $\Delta \log M/L_B = \eta \log(1 + z)$. The results are summarized in Table 5.

The residuals of the EDisCS cluster sample have an rms of 0.08 dex. The literature sample, which does not probe clusters with small velocity dispersions (see below), has an rms of 0.06 dex, the clusters at low redshift ($z \leq 0.2$) having systematically positive residuals. The combined sample has an rms scatter

Fig. 14. The FP of the EDisCS clusters with HST photometry. Each cluster is identified by its short name for clarity, see Table 4 for the full name. Colors code the spectroscopic type (black = 1, red = 2). Symbols code the morphology: filled ellipses show $T \leq -4$, filled circles crossed by a line $-3 \leq T \leq 0$, spirals $T > 0$. The magenta line shows the best-fit FP relation with no selection weighting. The full line shows the Coma cluster at zero redshift. The black dotted and dashed lines show data for the clusters MS2053-04 at $z = 0.58$ and MS1054-03 at $z = 0.83$, respectively, from Wuyts et al. (2004).

of 0.07. Taking into account the measurement errors, this implies an intrinsic scatter of 0.06 dex or 15% in M/L. The best-fit line closely matches the prediction of simple stellar population (hereafter SSP) models (Maraston 2005) with high formation redshift ($2 \leq z_f \leq 2.5$) and solar metallicities. Here and below we make use of Maraston (2005) models to translate mass-to-light or luminosity variations into formation ages or redshifts. Similar conclusions would be obtained using other models (e.g., Bruzual & Charlot 2003), as demonstrated for example by Jaffé et al. (2010). However, we bear in mind that systematic errors still affect the SSP approach (see Maraston et al. 2009; Conroy & Gunn 2010, for the difficulties in reproducing the colors of real galaxies).

Trimming the sample to high-precision data only (for example, considering only velocity dispersions determined to a

precision higher than 10%) does not change the overall picture. We discuss the effects of cutting the sample according to mass, spectroscopic type, or morphology in Sect. 3.2, where we consider the sample on a galaxy-by-galaxy basis, since any selection drastically reduces the number of clusters with at least 4 galaxies.

Figure 16 (right panel) shows the residuals $\Delta \log M/L_B + 0.54z$ as a function of the cluster velocity dispersion. No convincing correlation is seen (the Pearson coefficient is 0.21, the Spearman coefficient is 0.39 with a probability of 2.5% that a correlation exists), confirming that cluster massive early-type galaxies follow passive evolution up to high redshifts not only in massive clusters, as has been established (see discussion in the Introduction), but also in lower-mass structures down to the group size. There is a hint that scatter could increase
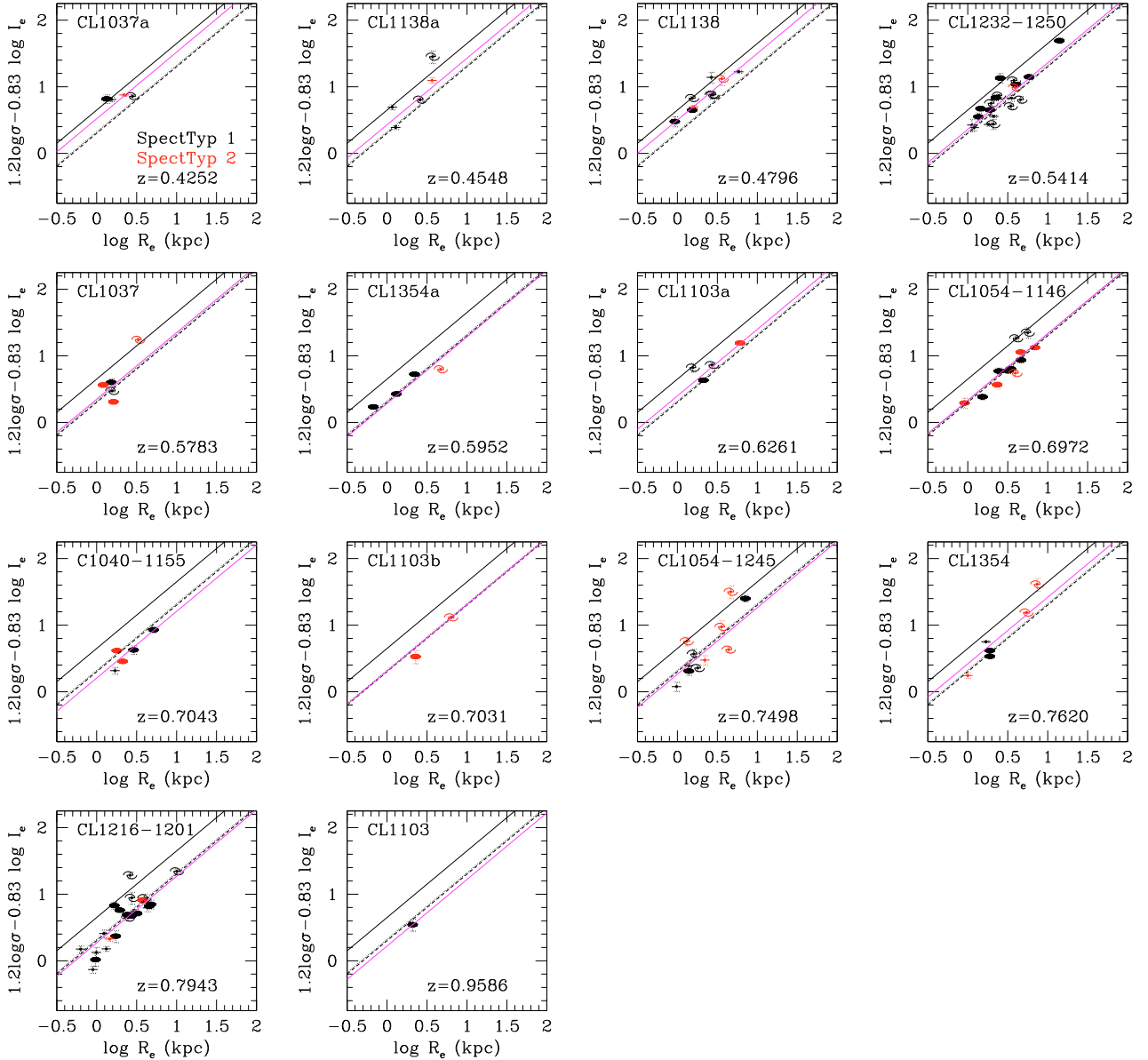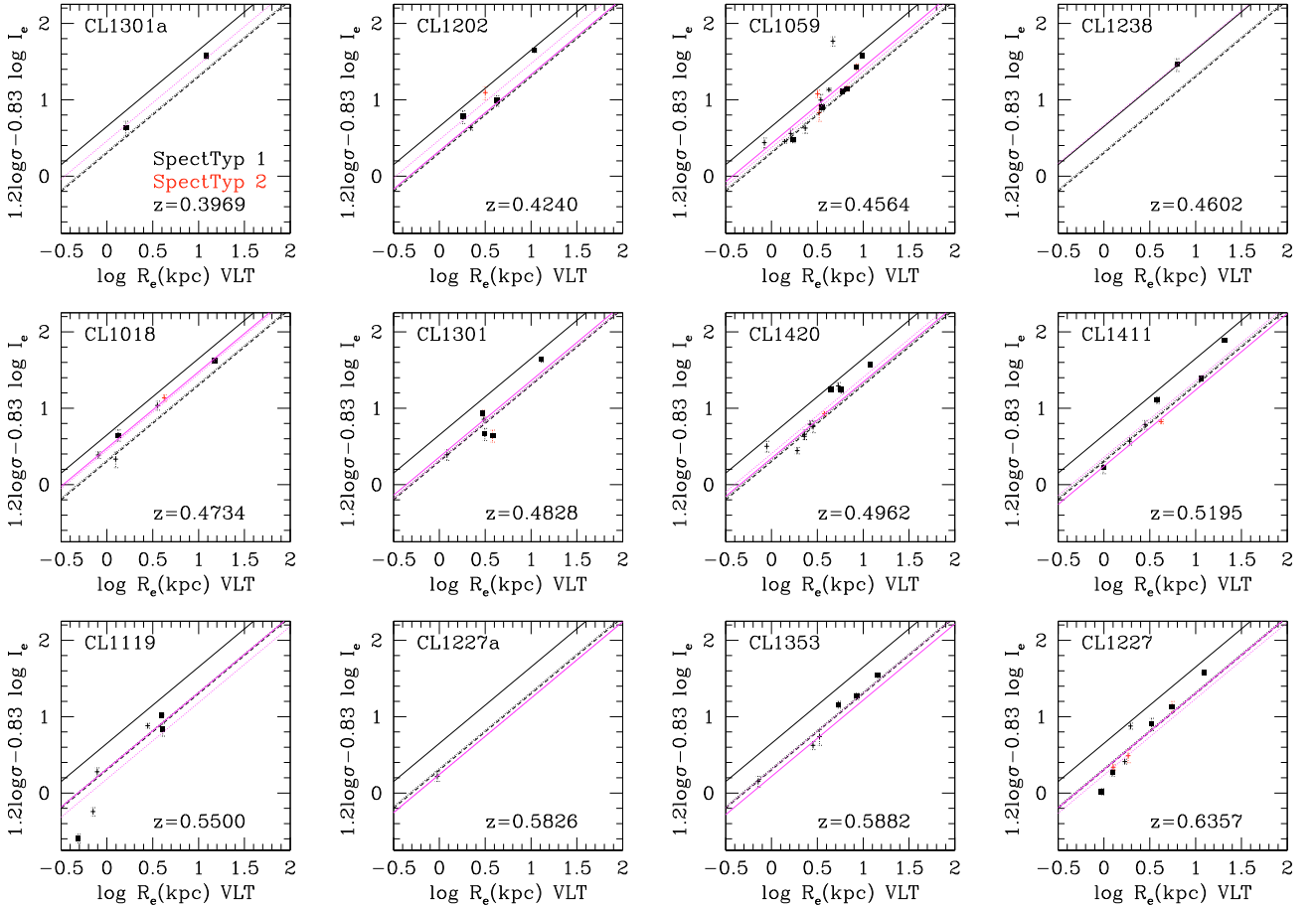
Fig. 15. The FP of the EDisCS clusters with VLT only photometry. Each cluster is identified by its short name for clarity, see Table 4 for the full name. Colors code the spectroscopic type. The black squares show galaxies with SExtractor flags different from 0 or 2 and therefore unreliable photometric parameters. The dotted magenta line shows the best-fit FP relation for all galaxies. The solid magenta line shows the best-fit FP relation when considering only galaxies with spectroscopy type ≤2 and SExtractor flag 0 or 2. The full line shows the Coma cluster at zero redshift. The black dotted and dashed lines show the clusters MS2053-04 at $z = 0.58$ and MS1054-03 at $z = 0.83$ from Wuyts et al. (2004), respectively.

for the low velocity-dispersion clusters: while the combined EDisCS+literature sample of high velocity-dispersion clusters ($\sigma_{\rm clus} > 800 \, {\rm km \, s^{-1}}$) exhibit an rms in the residuals $\Delta \log M/L_B + 0.54z$ of 0.06 dex, the lower $\sigma_{\rm clus}$ EDisCS clusters exhibit an rms of 0.08 dex. We note that the scatter in M/L measured in each cluster is larger (up to 0.3 dex) and intrinsic (i.e., not caused by measurement errors).

3.2. Environment and mass dependence

We now consider the sample on a galaxy-by-galaxy basis. As in Eq. (5), in Fig. 17 we show the evolution with redshift of $\Delta \log M/L_B = (1.2 \log \sigma - 0.83 \log I_e - \log R_e - 0.65)/0.83$ for the EDisCS cluster (left) and field (right) galaxies. For the 74 galaxies with both HST and VLT photometry, we derive a mean difference $\Delta \log M/L_B(VLT - HST) = -0.02$ with an rms of 0.06 or an error in the mean of 0.02, similar to that quoted for clusters in Sect. 3.1. In general, there is scatter in the galaxy data that falls even below the SSP model line for a formation redshift $z_{\rm f} = 1.2$ with twice-solar metallicity, or to positive values that are impossible to explain with SSP models. Many of these deviant points are galaxies with late-type morphology. Their measured velocity dispersion may not represent their dynamical state which is dominated by rotation.

First, we turn our attention to galaxies belonging to clusters. Averaging the points in redshift bins 0.1 wide shows that cluster galaxies closely follow the mean linear fit derived for clusters as a whole. This corresponds to a solar metallicity SSP model with formation redshift $z_{\rm f} = 2$ or formation lookback time of 10 Gyr (see Sect. 4.4 for a detailed discussion). The average values do not change within the errors if a cut in either mass ($M_{\rm dyn} > 10^{11} M_\odot$) or morphology ($T \le 0$) is applied. Table 5 lists the slope η and η' of $\Delta \log M/L = \eta \log(1 + z) = \eta' z$ derived by cutting the sample in a progressively more selective way. In general, P_S selection weighting produces shallower slopes. Shallower slopes are also obtained when only massive galaxies or spectral types ST = 1 are considered. The steepest slope ($\eta' = -0.56$) is obtained by considering only galaxies with HST early-type morphologies, no restrictions on either spectral type or mass, and no selection weighting. The shallowest slope ($\eta' = -0.32$) is obtained by considering only galaxies more massive than $10^{11} M_\odot$, with spectral type ST = 1, no constraints on morphology, and P_S weighting. Finally, considering galaxies with HST photometry and no constraints on morphology or mass, but with ellipticity less than $1 - b_e/a_e \le 0.6$ changes the slopes only minimally, from $\eta' = -0.53$ (for 113 objects) to $\eta' = -0.56$ (for 88 objects).

In contrast, galaxies in the field have values of $\Delta \log M/L_B$ more negative than the corresponding cluster bins starting
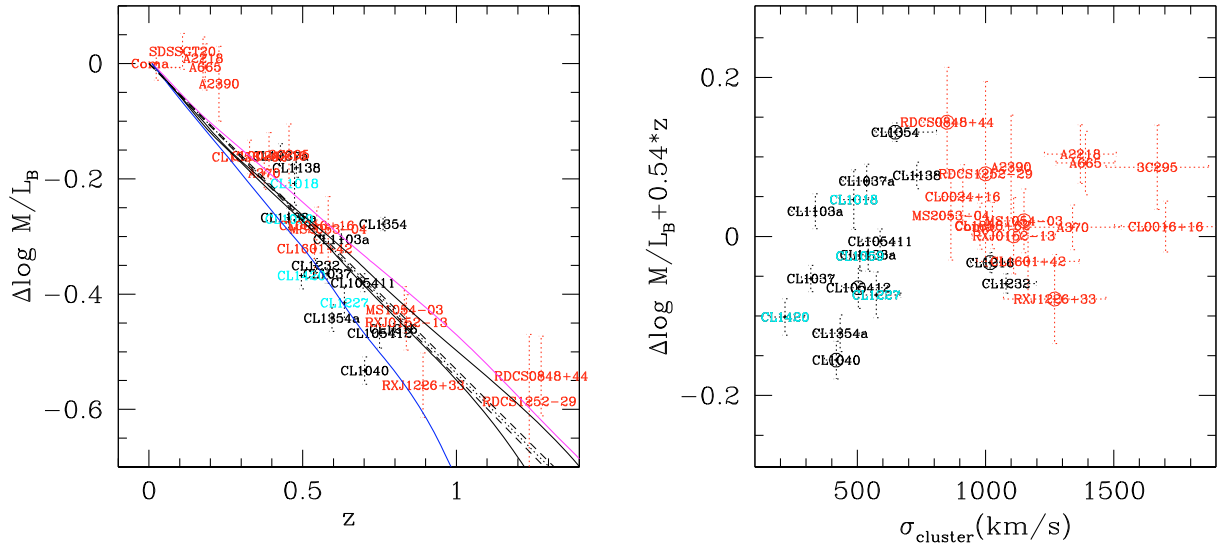
Fig. 16. *Left*: the redshift evolution of the *B* band mass-to-light ratio. The full black lines show the simple stellar population (SSP) predictions for a Salpeter IMF and formation redshift of either $z_f = 2$ (*lower*) or 2.5 (*upper curve*) and solar metallicity from Maraston (2005). The blue line shows the SSP for $z_f = 1.5$ and twice-solar metallicity, the magenta line the SSP for $z_f = 2.5$ and half-solar metallicity. The dotted line shows the best-fit linear relation and the 1σ errors dashed. *Right*: the (absence of) correlation of the M/L residuals $\Delta \log M/L_B + 0.54z$ with cluster velocity dispersion. Black points are EDisCS clusters with HST photometry, cyan points with VLT photometry. Each EDisCS cluster is identified by its short name for clarity, see Table 4 for the full name. Red points are from the literature, Bender et al. (1998) and van Dokkum & van der Marel (2007). Cluster velocity dispersions come from Halliday et al. (2004) and Milvang-Jensen et al. (2008) for EDisCS clusters and from Edwards et al. (2002) (Coma), Le Borgne et al. (1992) (A2218), Gómez et al. (2000) (A665), Carlberg et al. (1996) (A2390), Fisher et al. (1998) (CL1358+62), Mellier et al. (1988) (A370), Poggianti et al. (2006) (MS1054-03 and CL0024+16), van Dokkum & van der Marel (2007) (3C 295, CL1601+42, CL0016+16), Tran et al. (2005) (MS2053-04), Jørgensen et al. (2005) (RXJ0152-13), and Jørgensen et al. (2006) (RXJ1226+33) for the literature clusters. We estimate σ_{clus} for RDCS1252-29 and RDCS084+44 from their bolometric X-ray luminosity and the relation of Johnson et al. (2006). Circles indicate clusters at redshift >0.7.

from $z \approx 0.45$. For our sample, a solar metallicity SSP model with formation redshift $z_f = 1.2$ is an accurate representation of the data. This corresponds to a formation age of 8.4 Gyr or a mean age difference of 1.6 Gyr between cluster and field galaxies (see Sect. 4.4 for a detailed discussion). The slopes η listed in Table 5 for field galaxies are always steeper than the ones derived for cluster galaxies. The shallowest ($\eta' = -0.67$) is obtained when analyzing only galaxies more massive than $10^{11} M_\odot$ with ST = 2. Here we approach the result of van Dokkum & van der Marel (2007), who detect only a very small age difference between cluster and field galaxies of these masses and morphologies. Nevertheless, our shallowest slope for field galaxies is steeper than the steepest slope for cluster galaxies.

We compute dynamical masses as in Eq. (4). As discussed in the Introduction, the validity of this equation can be questioned in many respects. The value of the appropriate structural constant need not be the same for every galaxy. If ordered motions dominate the dynamics of a galaxy, as must be the case for disk galaxies, the use of velocity dispersion is inappropriate. Moreover, we also assume that the structure proportionality constant does not vary with redshift, which may not be true. Nevertheless, on average Eq. (4) delivers values that compare reasonably with stellar masses. We compute the (total) stellar masses from ground-based, rest-frame absolute photometry derived from SED fitting (Rudnick et al. 2009), adopting the calibrations of Bell & de Jong (2001), with a "diet" Salpeter IMF (with constant fractions of stars of mass less than 0.6 $M_\odot$) and $B - V$ colors, and renormalized using the corrections for an elliptical galaxy given in de Jong & Bell (2007). The method that calculates the rest-frame luminosities and colors is described

in Rudnick et al. (2003), and the rest-frame filters were taken from Bessel (1990). Although the photometric redshifts and rest-frame SEDs were computed from the matched aperture photometry of White et al. (2005), the rest-frame luminosities were adjusted to total values, as described in Rudnick et al. (2009).

In general, the dynamical masses are somewhat lower than the stellar ones ($M_{dyn}/M_* = 0.91$ for cluster galaxies, 0.75 for field galaxies), with an intrinsic scatter of a factor of two, on the order of the typical combined precision achieved for dynamical and stellar masses. If we consider only galaxies with HST morphology $T < 0$, the ratio M_{dyn}/M_* drops to 0.74 for cluster and 0.56 for field galaxies. Moreover, a possible decreasing trend with redshift of the ratio M_{dyn}/M_* is seen at the $2 - \sigma$ level, which is not unexpected given the size and velocity dispersion evolution discussed in Sect. 4.2. To conclude, the tendency for $M_{dyn}/M_* < 1$ may indicate that the structural constant used in Eq. (4) is too low. However, we note that the structural constant is the one that dynamical studies at low redshifts prefer (Cappellari et al. 2006; Thomas et al. 2010). Alternatively, our adopted IMF contains too high a fraction of low mass stars (Baldry et al. 2008). Finally, we refer to Thomas et al. (2010) for a discussion of the role of dark matter in the estimation of M_{dyn}.

In the following, we consider relations as a function of both dynamical and stellar masses to assess the robustness of each result.

Figure 18 shows the residuals $\Delta \log M/L_B + 1.66 \log(1 + z)$ as a function of galaxy dynamical mass, for cluster (top) and field galaxies (bottom), at low (left) and high (right) redshifts. We divided the sample into three redshift bins of $z < 0.5$, $0.5 \leq z < 0.7$, and $z \geq 0.7$. Averaging the points in mass

Table 4. The parameters of the EDisCS clusters with measured FP zero points $\Delta \log M/L_B$, without selection weighting.

N_{clus}	Cluster	Short name	Phot[a]	z_{clus}	σ_{clus} (km s^{-1})	$\Delta \log M/L_B$ (dex)	Scatter (dex)	N
1	cl1037.9-1243a	CL1037a	1	0.4252	537^{+46}_{-48}	-0.16 ± 0.02	0.13	4
2	cl1138.2-1133a	CL1138a	1	0.4548	542^{+63}_{-71}	-0.27 ± 0.02	0.27	5
3	cl1138.2-1133	CL1138	1	0.4796	732^{+72}_{-76}	-0.18 ± 0.02	0.08	9
4	cl1232.5-1144	CL1232	1	0.5414	1080^{+119}_{-89}	-0.35 ± 0.01	0.17	20
5	cl1037.9-1243	CL1037	1	0.5783	319^{+53}_{-52}	-0.36 ± 0.02	0.27	5
6	cl1354.2-1230a	CL1354a	1	0.5952	433^{+95}_{-104}	-0.44 ± 0.02	0.14	4
7	cl1103.7-1245a	CL1103a	1	0.6261	336^{+36}_{-40}	-0.30 ± 0.02	0.15	4
8	cl1054.4-1146	CL105411	1	0.6972	589^{+78}_{-70}	-0.38 ± 0.02	0.17	12
9	cl1040.7-1155	CL1040	1	0.7043	418^{+55}_{-46}	-0.53 ± 0.02	0.11	5
10	cl1054.7-1245	CL105412	1	0.7498	504^{+113}_{-65}	-0.47 ± 0.03	0.30	11
11	cl1354.2-1230	CL1354	1	0.762	648^{+105}_{-110}	-0.28 ± 0.01	0.22	6
12	cl1216.8-1201	CL1216	1	0.7943	1018^{+73}_{-77}	-0.46 ± 0.01	0.23	23
13	cl1059.2-1253	CL1059	0	0.4564	510^{+52}_{-56}	-0.27 ± 0.02	0.10	8
14	cl1018.8-1211	CL1018	0	0.4734	486^{+59}_{-63}	-0.21 ± 0.04	0.12	4
15	cl1420.3-1236	CL1420	0	0.4962	218^{+43}_{-50}	-0.37 ± 0.02	0.14	8
16	cl1227.9-1138	CL1227	0	0.6357	574^{+72}_{-75}	-0.42 ± 0.03	0.21	4
17	cl1103.7-1245	CL1103	1	0.9586	534^{+101}_{-120}	–	–	–
18	cl1103.7-1245b	CL1103b	1	0.7031	252^{+65}_{-85}	–	–	–
19	cl1119.3-1129	CL1119	0	0.5500	166^{+27}_{-29}	–	–	–
20	cl1202.7-1224	CL1202	0	0.424	518^{+92}_{-104}	–	–	–
21	cl1227.9-1138a	CL1227a	0	0.5826	341^{+42}_{-46}	–	–	–
22	cl1238.5-1144	CL1238	0	0.4602	447^{+135}_{-181}	–	–	–
23	cl1301.7-1139	CL1301	0	0.4828	687^{+81}_{-86}	–	–	–
24	cl1301.7-1139a	CL1301a	0	0.3969	391^{+63}_{-69}	–	–	–
25	cl1353.0-1137	CL1353	0	0.5882	666^{+136}_{-139}	–	–	–
26	cl1411.1-1148	CL1411	0	0.5195	710^{+125}_{-133}	–	–	–

Notes. [a] 1: with HST photometry, 0: with VLT photometry.

Table 5. The slopes of the zero-point evolution of the FP $\Delta \log M/L = 0.4(ZP(z) - ZP(0))/\beta_0 = \eta' z = \eta \log(1 + z)$.

Type	N_{gal}	P_S	HST	VLT	ST	Morph	M_{dyn}	η'	η
Clusters	132	No	Yes	Yes	2	10	All	-0.54 ± 0.01	-1.61 ± 0.01
Clusters	132	Yes	Yes	Yes	2	10	All	-0.47 ± 0.003	-1.43 ± 0.01
Cluster galaxies	154	No	Yes	Yes	2	10	All	-0.55 ± 0.006	-1.66 ± 0.02
Cluster galaxies	154	Yes	Yes	Yes	2	10	All	-0.48 ± 0.01	-1.45 ± 0.03
Cluster galaxies	67	No	Yes	Yes	2	10	$10^{11} M_\odot$	-0.44 ± 0.01	-1.34 ± 0.02
Cluster galaxies	67	Yes	Yes	Yes	2	10	$10^{11} M_\odot$	-0.36 ± 0.01	-1.10 ± 0.02
Cluster galaxies	43	No	Yes	Yes	1	10	$10^{11} M_\odot$	-0.41 ± 0.01	-1.24 ± 0.03
Cluster galaxies	43	Yes	Yes	Yes	1	10	$10^{11} M_\odot$	-0.32 ± 0.01	-0.97 ± 0.03
Cluster galaxies	76	No	Yes	No	2	0	All	-0.56 ± 0.01	-1.70 ± 0.02
Cluster galaxies	76	Yes	Yes	No	2	0	All	-0.51 ± 0.01	-1.54 ± 0.04
Cluster galaxies	33	No	Yes	No	2	0	$10^{11} M_\odot$	-0.47 ± 0.01	-1.44 ± 0.03
Cluster galaxies	33	Yes	Yes	No	2	0	$10^{11} M_\odot$	-0.44 ± 0.01	-1.34 ± 0.03
Cluster galaxies	24	No	Yes	No	1	0	$10^{11} M_\odot$	-0.46 ± 0.01	-1.41 ± 0.03
Cluster galaxies	24	Yes	Yes	No	1	0	$10^{11} M_\odot$	-0.43 ± 0.01	-1.32 ± 0.03
Field galaxies	68	No	Yes	Yes	2	10	All	-0.76 ± 0.01	-2.27 ± 0.03
Field galaxies	68	Yes	Yes	Yes	2	10	All	-0.76 ± 0.01	-2.28 ± 0.03
Field galaxies	28	No	Yes	Yes	2	10	$10^{11} M_\odot$	-0.68 ± 0.01	-2.05 ± 0.03
Field galaxies	28	Yes	Yes	Yes	2	10	$10^{11} M_\odot$	-0.67 ± 0.01	-1.99 ± 0.04
Field galaxies	16	No	Yes	Yes	1	10	$10^{11} M_\odot$	-0.70 ± 0.01	-2.10 ± 0.04
Field galaxies	16	Yes	Yes	Yes	1	10	$10^{11} M_\odot$	-0.73 ± 0.02	-2.16 ± 0.04
Field galaxies	32	No	Yes	No	2	0	All	-0.83 ± 0.01	-2.46 ± 0.04
Field galaxies	32	Yes	Yes	No	2	0	All	-0.87 ± 0.02	-2.58 ± 0.05
Field galaxies	8	No	Yes	No	2	0	$10^{11} M_\odot$	-0.83 ± 0.02	-2.43 ± 0.06
Field galaxies	8	Yes	Yes	No	2	0	$10^{11} M_\odot$	-0.90 ± 0.02	-2.59 ± 0.07
Field galaxies	6	No	Yes	No	1	0	$10^{11} M_\odot$	-0.82 ± 0.02	-2.40 ± 0.06
Field galaxies	6	Yes	Yes	No	1	0	$10^{11} M_\odot$	-0.91 ± 0.02	-2.59 ± 0.07
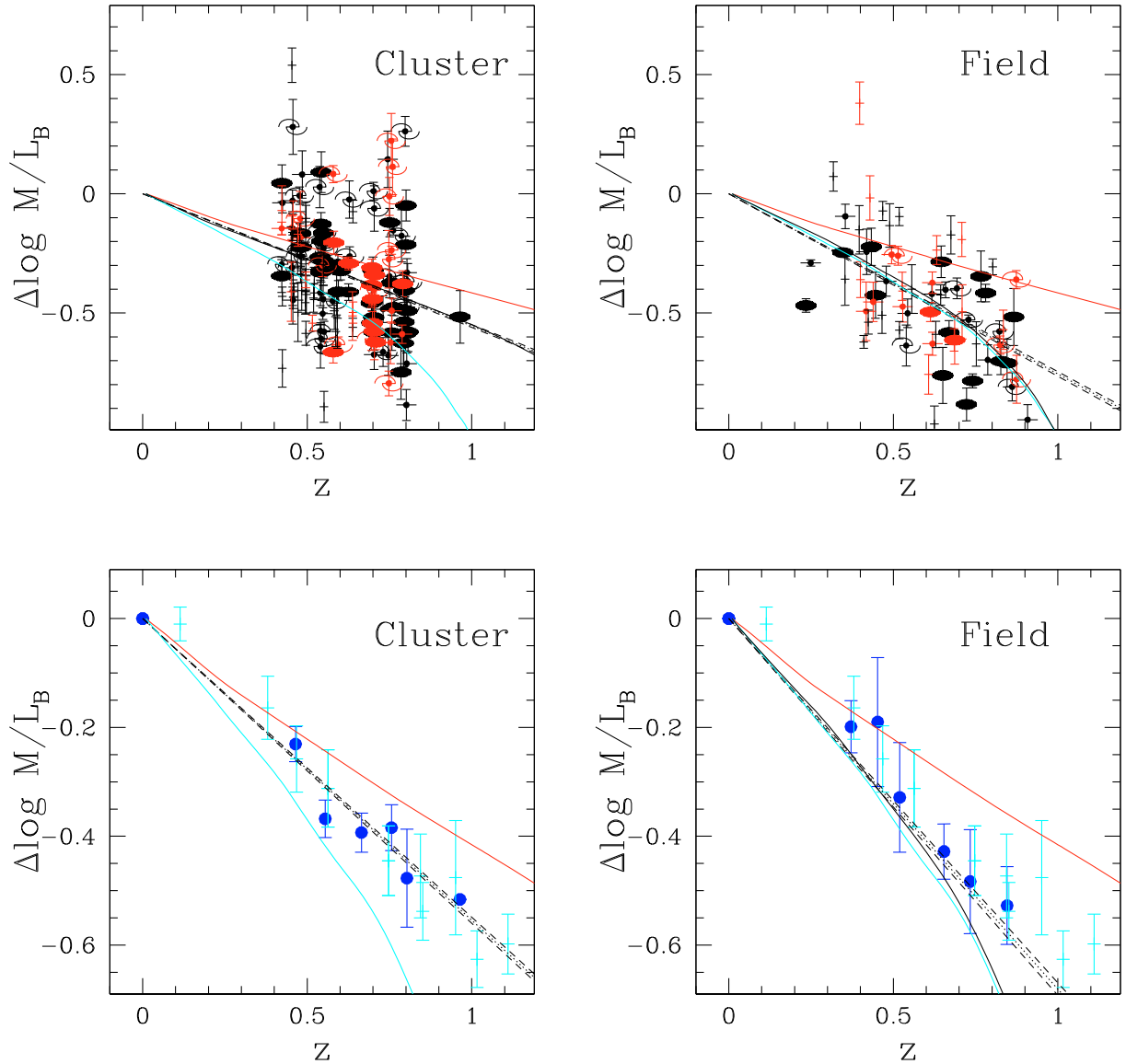
Fig. 17. The redshift evolution of the mass-to-light ratio for cluster (*left*) and field (*right*) galaxies. *Top*: black and red indicate galaxies with spectroscopic types 1 and 2, respectively. Morphologies for galaxies with HST photometry are coded as in Fig. 14. Galaxies with VLT photometry only are shown as crosses. Only galaxies with good VLT photometry (i.e., SExtractor flag 0 or 2) are plotted. The solid black lines show the solar metallicity SSP for $z_f = 2$ (cluster) and $z_f = 1.2$ (field). The solid red line shows the SSP for $z_f = 3.5$ and half-solar metallicity, the cyan line shows the SSP for $z_f = 1.2$ and twice-solar metallicity. The dotted line shows the best-fit linear relation ($-0.55z$ for cluster and $-0.76z$ for field galaxies) and the 1σ errors dashed. *Bottom*: the blue points show averages over redshift bins 0.1 wide. The cyan points are average field galaxies from van Dokkum & van der Marel (2007). Only field galaxies (plot to the right) with dynamical masses higher than $10^{11} M_\odot$ are considered.

bins 0.25 dex wide, one derives the following (see also Fig. 25). At low redshifts ($z < 0.5$), there is no convincing systematic trend between mass and residuals from the passively evolved FP, for both cluster (where the Pearson coefficient is 0.55 with a 2.5σ deviation from the no-correlation hypothesis) and field galaxies (where the Pearson coefficient is 0.15 for a t-value of 0.58 in agreement with the absence of a correlation). Within the errors, the solar metallicity SSP model with $z_f = 2$ provides a reasonable description of the evolution of luminosity of all cluster and field early-type galaxies more massive than $10^{10} M_\odot$. At intermediate redshifts ($0.5 \leq z < 0.7$), field (and to a lower extent cluster) galaxies with dynamical masses lower than $10^{11} M_\odot$ show systematically negative mean residuals. At higher redshifts

($z \geq 0.7$), both cluster and field galaxies with masses lower than $10^{11} M_\odot$ show systematically negative mean residuals, i.e., are brighter than predicted by the passively evolved FP at zero redshift, with Spearman correlation coefficients between mass and residuals larger than 0.66 and a t-value of 6.3 for cluster galaxies. The trends are stronger if we restrict the sample to galaxies with HST early-type ($T < 0$) morphology. We note that down to masses $\approx 4 \times 10^{10} M_\odot$ we sample a constant fraction ($\approx 20\%$) of the existing galaxy population (see Fig. 13). At lower masses, however, this drops to just 10% and we can expect residual selection effects to play a role, as discussed in van der Wel et al. (2005). We do not detect any additional dependence on cluster velocity dispersion.
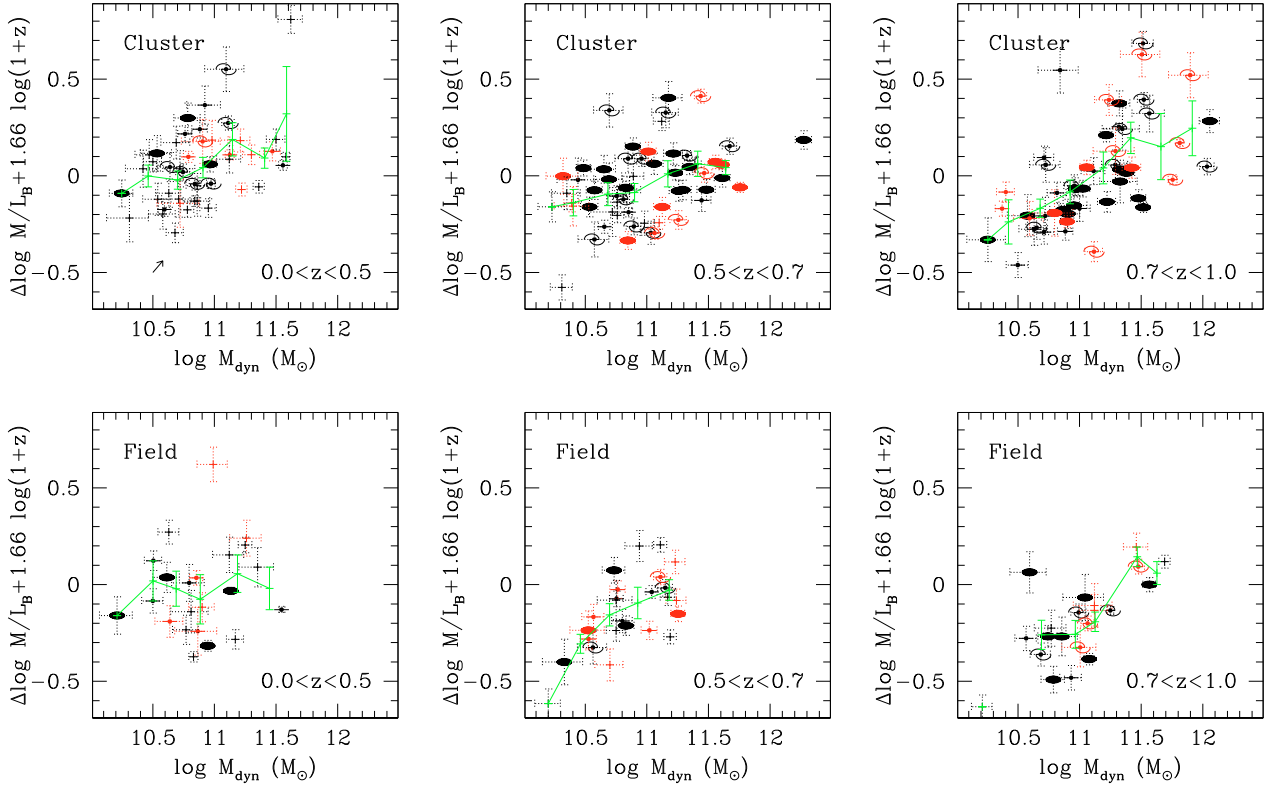
Fig. 18. The mass dependence of FP mass-to-light ratios. *Top*: the residuals $\Delta \log M/L_B + 1.66 \log(1+z)$ as a function of galaxy mass for cluster galaxies at low (*left*, $z < 0.5$), intermediate (*middle*, $0.5 \leq z < 0.7$), and high (*right*, $z > 0.7$) redshift. The arrow in the top left panel shows the how points change due to the typical 10% error in velocity dispersion. *Bottom*: the residuals $\Delta \log M/L_B + 1.66 \log(1+z)$ as a function of galaxy dynamical mass for field galaxies at low (*left*, $z < 0.5$), intermediate (*middle*, $0.5 \leq z < 0.7$), and high (*right*, $z \geq 0.7$) redshift. Colors and symbols as in Fig. 17. The green points show averages over $\log M_{dyn}$ bins 0.25 dex wide.

3.3. The rotation of the fundamental plane

As discussed by di Serego Alighieri et al. (2005), a mass dependence of the $\Delta \log M/L$ residuals implies a rotation of the FP as a function of redshift. Here we investigate the effect by assuming that the zero-point variation $\Delta \log M/L_B = -1.66 \times \log(1+z)$ for cluster and $\Delta \log M/L_B = -2.27 \times \log(1+z)$ for field galaxies is caused entirely by pure luminosity evolution. Accordingly, we correct the surface brightnesses of cluster galaxies by applying the offset $\Delta \log I_e = -1.66 \times \log(1+z)/0.83$ and of field galaxies by applying $\Delta \log I_e = -2.27 \times \log(1+z)/0.83$. This agrees with the observed evolution of the average effective surface brightness (see dotted line in Fig. 10), except for the highest redshift bins. We then fit the parameters α and β of Eq. (1) using the maximum likelihood algorithm of Saglia et al. (2001), which uses multi-Gaussian functions to describe the distribution of data points, taking into account the full error covariance matrix and selection effects (for a Bayesian approach to the modeling of systematic effects, see Treu et al. 2001). To ensure conformity with the procedures adopted in the literature, the results were derived with and without taking into account selection effects, but the differences between the two approaches are always smaller than the large statistical errors. We analyzed three redshift ranges for cluster galaxies and two for field galaxies. The results are shown in Table 6. The errors were computed as the 68% percentile of the results of Monte Carlo simulations for each fitted sample as in Saglia et al. (2001). The low redshift bins (up to $z = 0.7$) infer α coefficients that are compatible with local values ($\alpha \approx 1.2$) and β coefficients ($\beta \approx 0.23$–0.3) slightly smaller

than the local value ($\beta \approx 0.33$). In contrast, the highest redshift bins produce shallower $\log \sigma$ slopes. Given the relatively low number of galaxies per bin, especially in the low velocity dispersion regime, the statistical significance is just $\approx 1\sigma$, but the trend confirms the claims of the literature (see Sect. 1). In particular, both values of α and β decrease at high redshift, as observed by di Serego Alighieri et al. (2005), a consequence of the flattening with redshift of the power-law relation between luminosity and mass (see Sect. 4).

4. Size and velocity dispersion evolution

4.1. Setting the stage

Up to this point, we have analyzed and interpreted the ZP variations of the FP based on the assumption that it is caused mainly by a variation in the luminosity. As discussed in the Introduction, there is growing evidence that early-type galaxies evolve not only in terms of luminosity, but also in size and velocity dispersion. Here we examine the consequences of these findings.

In general, if sizes were shrinking with increasing redshift, we would expect the surface brightness to increase. Therefore, if the velocity dispersions do not increase a lot, the net effect will be to reduce the net amount of brightening with redshift caused by stellar population evolution. In detail, setting $\Delta ZP = ZP(z) - ZP(0)$ and considering that $\langle SB_e \rangle = -2.5 \log(L/2\pi R_e^2)$, we derive

$$\Delta ZP = \alpha_0 \Delta \log \sigma - 2.5\beta_0 \Delta \log L + (5\beta_0 - 1)\Delta \log R_e, \quad (6)$$

Table 6. The coefficients α and β of the EDisCS FP as a function redshift and the derived quantities $\epsilon = \frac{2-\alpha}{2\alpha}$ (with $M/L \propto L^\epsilon$), $\lambda = \frac{1}{1+\epsilon}$ (with $L \propto M^\lambda$), $A = \frac{10\beta-2-\alpha}{5\beta}$.

z range	$N_{\rm gal}$	$P_{\rm S}$	α	β	ϵ	λ	A	Environment
0		–	1.2	0.33	0.33	0.75	0.06	Local Sample
0.4–0.5	46	No	1.09 ± 0.33	0.23 ± 0.02	0.42 ± 0.30	0.71 ± 0.14	-0.69 ± 0.37	Cluster
0.5–0.7	57	No	1.04 ± 0.24	0.30 ± 0.02	0.46 ± 0.24	0.68 ± 0.11	-0.03 ± 0.21	Cluster
0.7–1.0	50	No	0.69 ± 0.42	0.23 ± 0.02	0.95 ± 1.07	0.51 ± 0.24	-0.35 ± 0.42	Cluster
0.4–0.7	39	No	1.05 ± 0.6	0.23 ± 0.02	0.45 ± 0.63	0.69 ± 0.27	-0.67 ± 0.58	Field
0.7–1.0	21	No	0.37 ± 0.27	0.23 ± 0.02	2.20 ± 2.09	0.31 ± 0.20	-0.06 ± 0.30	Field
0.4–0.5	46	Yes	1.06 ± 0.25	0.27 ± 0.02	0.44 ± 0.24	0.69 ± 0.11	-0.29 ± 0.25	Cluster
0.5–0.7	57	Yes	1.09 ± 0.30	0.32 ± 0.03	0.42 ± 0.27	0.70 ± 0.13	$+0.07 \pm 0.26$	Cluster
0.7–1.0	50	Yes	0.44 ± 0.20	0.25 ± 0.03	1.77 ± 1.21	0.36 ± 0.13	$+0.02 \pm 0.28$	Cluster
0.4–0.7	39	Yes	1.00 ± 0.7	0.23 ± 0.02	0.50 ± 0.75	0.67 ± 0.32	-1.03 ± 0.76	Field
0.7–1.0	21	Yes	0.22 ± 0.7	0.20 ± 0.02	4.04 ± 3.42	0.20 ± 0.13	$+0.15 \pm 0.20$	Field

where $\Delta \log R_e = \overline{\log R_e(z)} - \overline{\log R_e(0)}$ and $\Delta \log \sigma = \overline{\log \sigma(z)} - \overline{\log \sigma(0)}$ are the variations with redshifts in the mean half-luminosity radius and average surface brightness. Therefore, the redshift variation in the luminosity, taking into account the size and velocity dispersion evolution of galaxies is

$$\Delta \log L = \frac{10\beta_0 - 1}{5\beta_0} \Delta \log R_e + \frac{2\alpha_0}{5\beta_0} \Delta \log \sigma - \frac{2\Delta ZP}{5\beta_0} . \quad (7)$$

We note that the ZP variations were determined by assuming constant α_0 and β_0 coefficients, which is probably not true at the high redshift end of our sample (see Sect. 3.3).

If the variations are computed at constant dynamical mass, then $\Delta \log \sigma = -\Delta \log R_e/2$, as in the "puffing" scenario of Fan et al. (2008, see below) and Eq. (7) becomes

$$\Delta \log L_{\rm pu} = \frac{10\beta_0 - 2 - \alpha_0}{5\beta_0} \Delta \log R_e - \frac{2\Delta ZP}{5\beta_0} . \quad (8)$$

In this case, the contribution of the size evolution to the luminosity evolution at constant mass derived from the FP is zero if

$$A_0 = \frac{10\beta_0 - 2 - \alpha_0}{5\beta_0}, \quad (9)$$

is zero, i.e., $\alpha_0 = 10\beta_0 - 2$. This is the expected relation between α and β if the mass-to-light ratio M/L varies as a power law of the luminosity $M/L \propto L^\epsilon$, in which case one has $L \propto M^{\frac{1}{1+\epsilon}} = M^\lambda$, $\alpha = \frac{2}{1+2\epsilon}$, and $\beta = \frac{2}{5} \frac{1+\epsilon}{1+2\epsilon}$. Table 6 lists the values of ϵ, λ, and A implied by the fits of the FP coefficients performed in Sect. 3.3.

If we parametrize all variations as a function of $\log(1 + z)$ as $\Delta \log R_e = \nu \log(1 + z)$, $\Delta \log \sigma = \mu \log(1 + z)$, and $\Delta ZP = \kappa \log(1 + z)$, we find that

$$\Delta \log L = \left(\frac{10\beta_0 - 1}{5\beta_0} \nu + \frac{2\alpha_0}{5\beta_0} \mu - \frac{2}{5\beta_0} \kappa \right) \log(1 + z) + \phi z, \quad (10)$$

where ϕz is the correction for progenitor bias estimated by van Dokkum & Franx (2001) to be $\phi = +0.09$. Their result can be applied to our work directly, since our redshift dependence of the FP ZP closely matches that considered there.

As discussed in the Introduction, the size and σ evolution of galaxies is usually interpreted as a result of the merging history of galaxies. The merger models of Hopkins et al. (2009) predict $\nu_{\rm me} \approx -0.5$ and $\mu_{\rm me} = 0.1$ for galaxies with constant stellar mass $M_* \approx 10^{11}$ with $(M_{\rm halo}/R_{\rm halo})/(M_*/R_e) \approx 2$. This means that $\Delta \log R_e = -0.2\Delta \log \sigma$. As an alternative explanation, Fan et al. (2008) proposed the "puffing" scenario, where

galaxies grow in size conserving their mass as a result of quasar activity. In this case, one has $\sigma_{\rm pu} \propto R_e^{-1/2}$. We note, however, that this mechanism should already have come to an end at redshift 0.8. Moreover, the strong velocity dispersion evolution predicted by the puffing scenario at redshifts higher than 1 was ruled out by Cenarro & Trujillo (2009).

Using $\nu = -0.5$, $\mu = +0.1$, the change in the slope $\Delta \tau = \frac{10\beta_0 - 1}{5\beta_0} \nu + \frac{2\alpha_0}{5\beta_0} \mu$ of the luminosity evolution $\Delta \log L = \tau \log(1 + z)$ (see Eq. (7)) is ≈ -0.5 units. We now attempt to determine the values of ν and μ implied by our dataset.

4.2. The redshift evolution of R_e and σ

Following van der Wel et al. (2008), we investigated the size evolution of EDisCS galaxies by considering the $Mass - R_e$ relation for objects with masses higher that $3 \times 10^{10} M_\odot$. In Fig. 19, we divided our sample into 8 redshift bins (centered on redshifts from 0.25 to 0.95 of bin size $\Delta z = 0.1$) and fit the relation $R_e = R_c(M/M_c)^b$. We considered both dynamical ($M_{\rm dyn}$, left) and stellar (M_*, right) masses, and we weighted each galaxy with $1/P_{\rm S}$. Within the errors, b does not vary much and is compatible with the values $b = 0.56$ found locally. In Fig. 19, we therefore keep its value fixed and determine R_c at the mass $M_c = 2 \times 10^{11} M_\odot$. We fitted the function $R_c(z) = R_c(0) \times (1 + z)^\nu$ and summarize the values of the parameters resulting from the fits in Table 7. As becomes clear below, this does not necessarily describe the size evolution of a galaxy of fixed mass, but rather at any given redshift the mean value of the size of the evolving population of galaxies with this given mass.

Given the larger uncertainties in the R_e values derived from VLT photometry, we first fitted the HST dataset alone (entries 1 and 2 of Table 7). Within the errors, both $R_c(0)$ and the slope are very similar to the values reported by van der Wel et al. (2008, $R_c(0.06) = 4.8$ kpc, $\nu = 0.98 \pm 0.11$) for both dynamical and stellar mass fits. Our results do not change within the errors if we separately fit galaxies belonging to clusters or to the field. If we add the galaxies with VLT photometry only (entries 3 and 4 of Table 7), we derive larger R_c and steeper slopes.

Figure 20 shows R_c as a function of redshift when we apply a correction for progenitor bias as in Valentinuzzi et al. (2010a). The EDisCS galaxies considered here are a sample of spectroscopically selected passive objects. In contrast, a morphologically selected local sample of early-type galaxies contains objects with relatively young ages that, when evolved to EDisCS redshifts, would not be recognized as being spectroscopically passive. Valentinuzzi et al. (2010a) analyze the WINGS sample of local galaxies and determine their ages by means of a

Fig. 19. The evolution in the $R_e - mass$ relation with redshift. *Left*: dynamical masses. *Right*: stellar masses. Colors and symbols are as in Fig. 17. The numbers give the average redshift in each bin. The full lines show the best-fit relation $R_e = R_c(M/2 \times 10^{11} \, M_\odot)^{0.56}$ with uniform galaxy weighting, the dashed lines with selection weighting. The blue lines show the reference line at zero redshifts. The vertical lines show the $2 \times 10^{11} \, M_\odot$ mass.

Table 7. The redshift evolution of the mass correlation fits.

Case	Parameter	P_S	PB	$\log M$ slope	M_{dyn}		M_*	
					$z = 0$	$(1 + z)^{Slope}$	$z = 0$	$(1 + z)^{Slope}$
1	R_e(kpc) HST	No	No	0.56	5.1 ± 0.7	-1.0 ± 0.3	4.3 ± 1.1	-1.0 ± 0.6
2	R_e(kpc) HST	Yes	No	0.56	5.5 ± 0.9	-1.3 ± 0.4	4.6 ± 1.3	-1.2 ± 0.7
3	R_e(kpc)	No	No	0.56	5.7 ± 0.5	-1.2 ± 0.2	6.1 ± 0.6	-1.6 ± 0.2
4	R_e(kpc)	Yes	No	0.56	5.7 ± 0.8	-1.3 ± 0.3	6.4 ± 0.9	-1.7 ± 0.4
5	R_e(kpc) HST	No	Yes	0.56	4.4 ± 0.4	-0.46 ± 0.2	4.3 ± 0.7	-0.68 ± 0.4
6	R_e(kpc) HST	Yes	Yes	0.56	4.6 ± 0.5	-0.67 ± 0.3	4.3 ± 0.7	-0.84 ± 0.4
7	R_e(kpc)	No	Yes	0.56	4.6 ± 0.4	-0.5 ± 0.2	4.8 ± 0.4	-0.75 ± 0.2
8	R_e(kpc)	Yes	Yes	0.56	4.6 ± 0.5	-0.65 ± 0.2	4.9 ± 0.5	-0.86 ± 0.3
9	σ (km s^{-1})	No	No	0.23	175 ± 8	$+0.59 \pm 0.10$	185 ± 13	$+0.34 \pm 0.14$
10	σ (km s^{-1})	Yes	No	0.23	175 ± 14	$+0.68 \pm 0.17$	189 ± 23	$+0.39 \pm 0.24$
11	σ (km s^{-1})	No	Yes	0.23	188 ± 7	$+0.41 \pm 0.08$	199 ± 9	$+0.19 \pm 0.1$
12	σ (km s^{-1})	Yes	Yes	0.23	188 ± 10	$+0.49 \pm 0.11$	201 ± 15	$+0.27 \pm 0.16$
13	$L(10^{10} \, L_\odot)$ Cluster	No	No	0.75	2.1 ± 0.4	$+2.1 \pm 0.4$	2.8 ± 0.7	$+1.2 \pm 0.4$
14	$L(10^{10} \, L_\odot)$ Cluster	Yes	No	0.75	1.9 ± 1.4	$+1.9 \pm 1.2$	2.5 ± 0.6	$+1.4 \pm 0.4$
15	$L(10^{10} \, L_\odot)$ Field	No	No	0.75	2.4 ± 0.2	$+2.4 \pm 0.2$	2.3 ± 0.5	$+1.9 \pm 0.4$
16	$L(10^{10} \, L_\odot)$ Field	Yes	No	0.75	2.0 ± 0.7	$+2.7 \pm 0.6$	2.0 ± 0.8	$+2.1 \pm 0.8$

Notes. Selection weighting and progenitor bias correction are applied when P_S = Yes and PB = Yes.

spectral analysis. They select objects that were already passive (i.e., have an age $\geq$1.5 Gyr) at the cosmic time of the redshifts $z = 0, 0.25, 0.5, 0.75$ and 1, and compute the median half-luminosity radii of massive galaxies. The resulting R_e vary as $R_e = (4.1 \pm 0.1) - (0.8 \pm 0.2)z$ (kpc), when selecting galaxies with dynamical masses $10^{11} < M_{dyn}/M_\odot < 3 \times 10^{11}$, and as $(4.3 \pm 0.1) - (0.9 \pm 0.2)z$ when selecting galaxies with stellar masses $10^{11} < M_*/M_\odot < 3 \times 10^{11}$. Therefore, we multiply the $R_c(z)$ derived at $M_{dyn} = 10^{11} M_\odot$ by $\frac{4.1}{4.1-0.8z}$, and those at $M_* = 10^{11} M_\odot$ by $\frac{4.3}{4.3-0.9z}$. With these corrections, the residual evolution is small, and even compatible with no evolution up to redshift $z \approx 0.7$ with dynamical masses, and 0.5 with stellar masses. Similar results are derived if we also consider the galaxies with VLT photometry, with the caveats discussed

above. Our correction for progenitor bias is of course somewhat model-dependent, since objects might cross the boundaries between populations. For example, there might be $z \sim 0.6$ passive galaxies that produce $z = 0$ descendants with some younger stars, after accreting gas or gas-rich objects.

In Figs. 21 and 22, we show the analogous plots and fits for the velocity dispersion. Table 7 lists the relative results. We find that σ scales as $\approx M_{dyn}^{0.23}$. The trend weakens at low masses and high redshifts, especially when stellar masses are considered. The fit at constant dynamical mass is just a consistency check, which should infer a slope of the redshift dependence of opposite sign to and half the value of the one measured for R_c ($\mu = +0.68$) and this is the case. In contrast, a weaker redshift evolution ($\mu = 0.39$) is derived if stellar masses are considered,

Fig. 20. The size evolution with redshift of EDisCS galaxies corrected for progenitor bias (see text). *Left*: R_c as a function of redshift at $2 \times 10^{11} M_\odot$ (see Fig. 19, left) derived using M_{dyn}. *Right*: R_c at $2 \times 10^{11} M_\odot$ (see Fig. 19, right) as a function of redshift derived using M_*. The full lines show the best-fit function to the galaxies with HST photometry (yellow points) $R_c = R_c^0 \times (1+z)^{-\nu}$ without selection weighting (see Table 7, case 1). The open dots show the local sample of Valentinuzzi et al. (2010a) evolved at the redshifts 0, 0.25, 0.5, 0.75, and 1, after having applied the progenitor bias correction. The dashed line shows the local value.
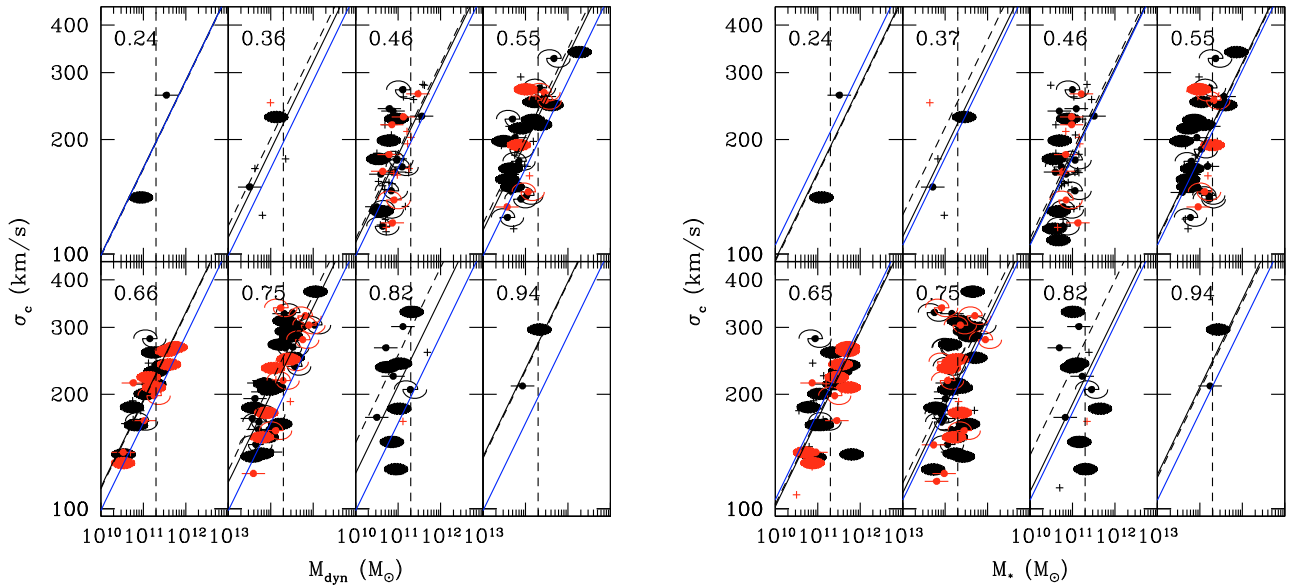
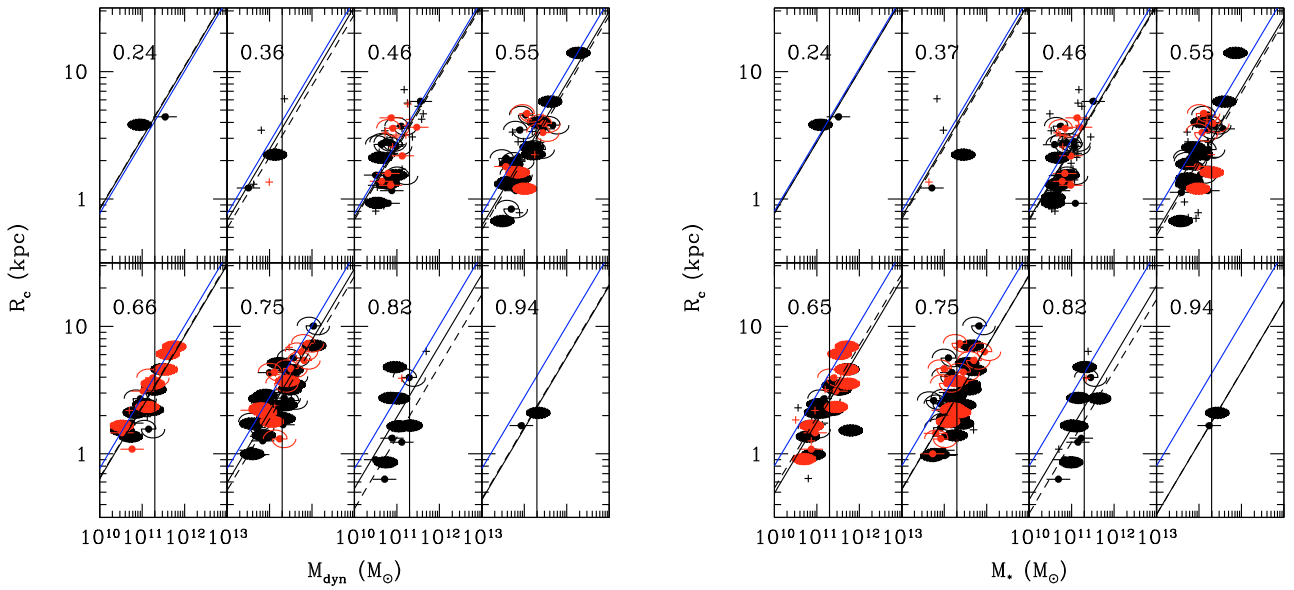**Fig. 21.** The evolution of the σ-mass relation with redshift. *Left*: dynamical masses. *Right*: stellar masses. Colors and symbols as in Fig. 17. The numbers give the average redshift in each bin. The full lines show the best-fit relation $\sigma = \sigma_C (M/M_C)^{0.23}$ with uniform galaxy weighting, the dashed line with selection weighting. The blue lines show the reference line at zero redshifts. The vertical line indicates the $M_C = 2 \times 10^{11} M_\odot$ mass.

in agreement with Cenarro & Trujillo (2009). This is expected, since, as discussed above, σ_c at fixed M_* should certainly be smaller than σ_c at fixed M_{dyn} given that $M_{dyn}/M_* < 1$.

Following the procedure of Valentinuzzi et al. (2010a) described above, we construct the local sample of WINGS galaxies with velocity dispersions, trimmed to contain only massive spectroscopically passive galaxies at the redshifts $z = 0, 0.25, 0.5, 0.75$, and 1, and compute the median σ of massive galaxies. The resulting σ vary as $\sigma = (197 \pm 2) + (6 \pm 4)z$ km s^{-1}, when selecting

galaxies with dynamical masses $10^{11} < M_{dyn}/M_\odot < 3 \times 10^{11}$, and is constant at (210 ± 1.5) km s^{-1} when selecting galaxies with stellar masses $10^{11} < M_*/M_\odot < 3 \times 10^{11}$. Therefore, we correct the measured σ_c for the progenitor bias by multiplying the values derived at $M_{dyn} = 10^{11} M_\odot$ by $\frac{197}{197 + 6z}$, and no correction is applied at constant stellar mass. The residual redshift evolution after the correction and fitting the point at zero redshift is small.

Table 9 lists the changes in the slope $\Delta\tau = \frac{10\beta_0 - 1}{5\beta_0}\nu + \frac{2\alpha_0}{5\beta_0}\mu$ of the luminosity evolution $\Delta \log L = \tau \log(1 + z)$ (see Eq. (7))
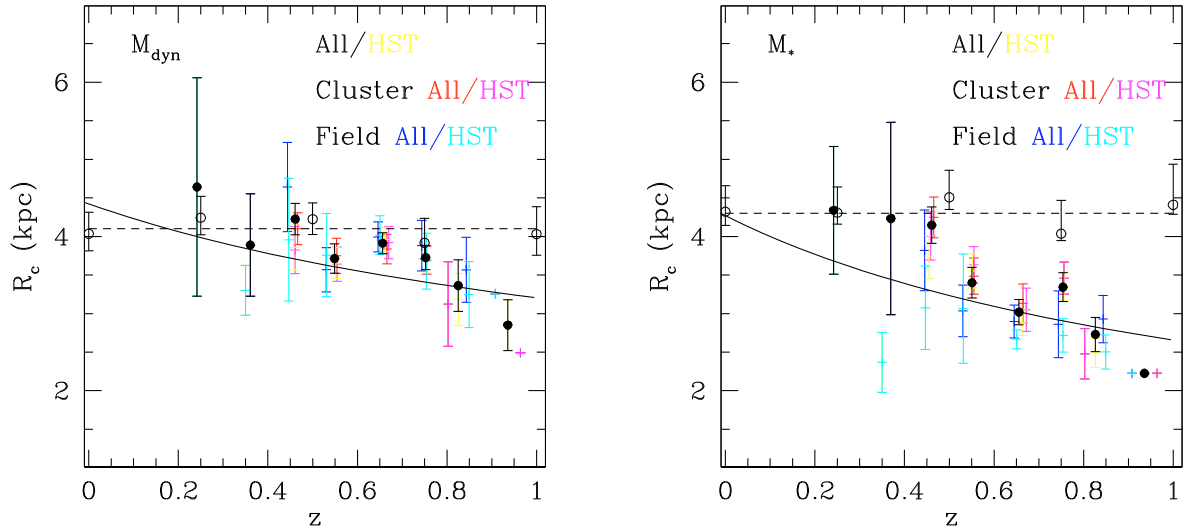
Fig. 22. The σ evolution with redshift of EDisCS galaxies corrected for progenitor bias (see text). *Left*: σ_c as a function of redshift derived using M_{dyn}. *Right*: σ_c as a function of redshift derived using M_*. The full lines show the best-fit function $\sigma_c = \sigma_c^0 \times (1+z)^\mu$ without selection weighting (see Table 7). The open dots show the local sample of Valentinuzzi et al. (2010a) evolved to the redshifts 0, 0.25, 0.5, 0.75, and 1, and after having applied the progenitor bias correction. The dashed line shows the local value.

derived from the measured variation in the FP ZP caused by the size and velocity dispersion evolution, coding the different cases listed in Table 7. For example, "case 1+9 M_{dyn}" uses the value of ν derived for the redshift evolution of R_c constructed using the $R_e - M_{\mathrm{dyn}}$ relation with HST data, without both selection weighting and progenitor bias correction (case 1 of Table 7), and the value of μ derived from the redshift evolution of σ inferred in turn from the $\sigma - M_{\mathrm{dyn}}$ relation, without both selection weighting and progenitor bias correction (case 9 of Table 7), obtaining $\Delta \tau = -0.39$. This implies that the luminosity evolution inferred from the ZP evolution of the EDisCS clusters without selection weighting ($L \sim (1+z)^{1.61}$, see Table 5) reduces to $L \sim (1+z)^{1.22}$.

To summarize, none of the values of $\Delta \tau$ listed in Table 9 differ statistically from zero. However, without taking into account the progenitor bias (rows two to five of Table 9), the values of ν and μ are much larger than inferred by the merger scenario of Hopkins et al. (2009) and when used in Eq. (10) reduce the predicted luminosity evolution with redshift drastically. In contrast, by taking into account the progenitor bias (rows six to nine of Table 9), the correction $\Delta \tau$ to the redshift slope of the luminosity evolution inferred from the FP is far smaller.

4.3. Luminosity evolution: the direct fit

To close the loop, in Fig. 23 we directly considered the relation between total luminosity L_B and dynamical mass as a function of redshift. In general, the power law $L = L_C(M/M_C)^{0.75}$ provides a reasonable fit to the data. Without selection weighting, we derived L_C as a function of redshift as shown in Fig. 24 for dynamical and stellar masses. Fitting the power-law relation $L_C = L_C(0)(1 + z)^\tau$ to $z > 0.4$ data points, separately for cluster and field galaxies, we derived the results listed in Table 7. The zero-redshift extrapolations compare well to the local values derived by considering the sample of Faber et al. (1989) ($L_C = 2.2 \times 10^{10}\ L_\odot$ and $M/L_B = 8.9\ M_\odot/L_\odot$). As for the $\sigma_c - z$ relation, we inferred a shallower luminosity evolution

when measuring L_c at constant M_*. The luminosity evolution with redshift is steeper for field galaxies.

Given the large errors in the luminosity fits, the derived luminosity evolution agrees with the ones derived from the FP analysis. At face value, the FP ZPs without size and velocity dispersion evolution corrections slightly overestimate the luminosity evolution at constant stellar mass and underestimate that at constant dynamical mass. This corroborates the conclusion that the corrections $\Delta \tau$ for size and velocity dispersion evolution must be small, as one finds when the progenitor bias is taken into account.

4.4. Ages

As a final step, we translated the observed evolution in the FP zero points, into an age estimate. We examined three cases that define the realistic range of possible luminosity evolutions: (1) minimal evolution, using $\Delta \tau = -0.7$ (M_*, case 6+12, of Table 7) and $\phi = 0$; (2) $\Delta \tau = 0$ and $\phi = 0$, where the small size and velocity dispersion correction compensates the progenitor bias of van Dokkum & Franx (2001); (c) $\Delta \log L = \phi z$, where the size and velocity dispersion correction is zero and we take into account the progenitor bias of van Dokkum & Franx (2001). We convert the mean $\Delta \log M/L_B$ for cluster and field galaxies measured in the mass bins of Fig. 18 into an age, by considering the various options for size evolution discussed above. We use the solar-metallicity (motivated by the analysis of the averaged line indices discussed below), Salpeter IMF SSP models of Maraston (2005) at the appropriate mean redshift of the bin. Ages older than the age of the universe at that redshift are set to the age of the universe. Figure 25 shows the results, Table 8 gives the average values for $M_{\mathrm{dyn}} < 10^{11}\ M_\odot$ and $M_{\mathrm{dyn}} > 10^{11}\ M_\odot$.

Cluster galaxies more massive than $10^{11}\ M_\odot$ are 6 to 8 Gyr old, with formation redshifts higher than 1.5, while galaxies of lower masses are some 3−4 Gyr younger. This parallels the findings of Sánchez-Blázquez et al. (2009), where the analysis of

Table 8. The ages derived from the evolution of the FP ZP, averaged for $M_{\rm dyn} < 10^{11}\ M_\odot$ and $M_{\rm dyn} > 10^{11}\ M_\odot$.

					Age (Gyr)		
Type	HST	VLT	Morph	Mass	$z < 0.5$	$0.5 < z < 0.7$	$z > 0.7$
Cluster	Yes	Yes	10	<	$4.7^{+3.1}_{-1.2}$	$2.4^{+2.7}_{0.4}$	$1.8^{+2.1}_{-0.3}$
Cluster	Yes	Yes	10	>	$8.6^{+0}_{-0.3}$	$5.7^{+2.0}_{-1.7}$	$6.3^{+0.5}_{-0.3}$
Cluster	Yes	No	0	<	$7.2^{+0.7}_{-0.1}$	$3.2^{+4.1}_{-0.7}$	$1.8^{+1.9}_{-0.3}$
Cluster	Yes	No	0	>	$8.5^{+0.2}_{-1.0}$	$4.4^{+3.2}_{-1.1}$	$4.6^{+2.1}_{-1.3}$
Field	Yes	Yes	10	<	$3.9^{+3.2}_{-0.8}$	$1.7^{+1.6}_{-0.3}$	$1.1^{+0.9}_{-0.2}$
Field	Yes	Yes	10	>	$6.7^{+2.7}_{2.0}$	$3.8^{+4.0}_{-0.9}$	$4.5^{+1.1}_{-1.0}$
Field	Yes	No	0	<	$3.4^{+2.8}_{-0.7}$	$2.2^{+2.3}_{-0.4}$	$1.4^{+1.1}_{-0.3}$
Field	Yes	No	0	>	$3.3^{+3.3}_{-0.4}$	$2.1^{+2.0}_{-0.3}$	$2.4^{+1.8}_{-0.6}$

Notes. The variations in the case of maximal evolution and the progenitor bias of van Dokkum & Franx (2001) are also given.
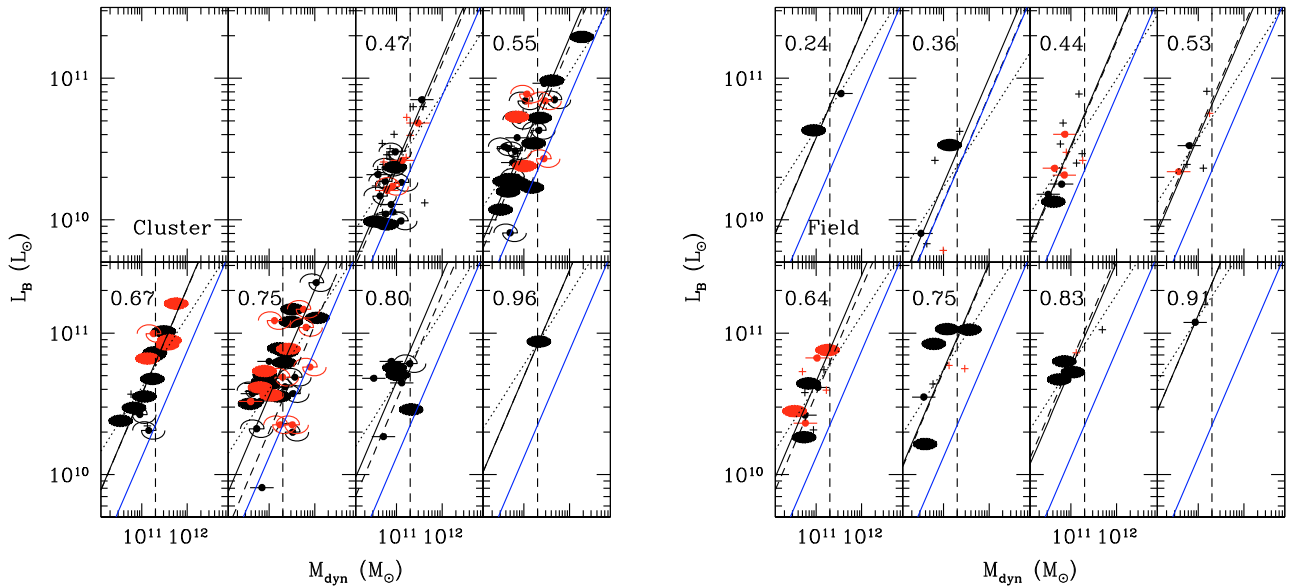
Fig. 23. The evolution of the luminosity-mass relation with redshift for cluster (*left*) and field (*right*) galaxies. Colors and symbols as in Fig. 17. The numbers give the average redshift in each bin. The full lines show the best-fit relation $L_B = L_{\rm c}(M/M_{\rm C})^{0.75}$, and the dotted lines $L = L_{\rm c}(M/M_{\rm C})^{0.5}$, both relations having uniform galaxy weighting. The dashed lines show the 0.75 power law with selection weighting. The blue lines show the reference line at zero redshifts. The vertical line indicates the $M_{\rm C} = 2 \times 10^{11}\ M_\odot$ mass.

Table 9. The change in slope $\Delta\tau = \frac{10\beta_0 - 1}{5\beta_0}\nu + \frac{2\alpha_0}{5\beta_0}\mu$ of the luminosity evolution $\Delta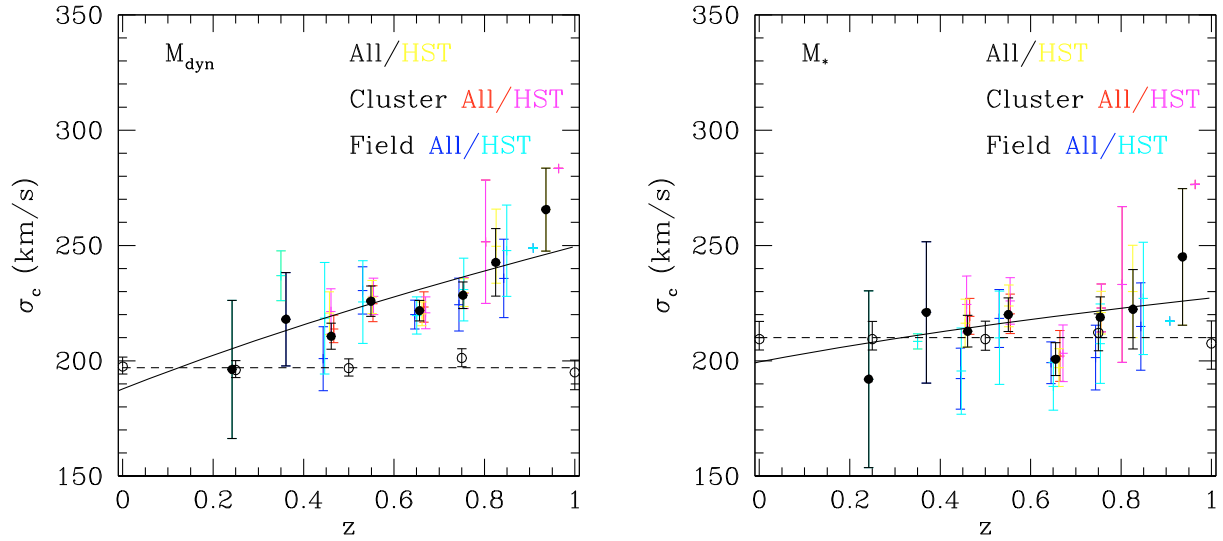 \log L = \tau \log(1 + z)$ (see Eq. (7)) derived from the measured variation in the FP ZP caused by the size and velocity dispersion evolution for the different cases listed in Table 7.

Case	ν	μ	$\Delta\tau$
Hopkins et al. (2009)	−0.5	+0.1	−0.51
1+9 $M_{\rm dyn}$	−1.0	+0.59	−0.39 ± 0.43
1+9 M_*	−1.0	+0.34	−0.78 ± 0.83
2+10 $M_{\rm dyn}$	−1.3	+0.68	−0.65 ± 0.60
2+10 M_*	−1.2	+0.39	−0.98 ± 1.01
5+11 $M_{\rm dyn}$	−0.46	+0.41	+0.04 ± 0.30
5+11 M_*	−0.68	+0.19	−0.60 ± 0.55
6+12 $M_{\rm dyn}$	−0.67	+0.49	−0.11 ± 0.43
6+12 M_*	−0.84	+0.27	−0.69 ± 0.59

spectral indices of EDisCs cluster galaxies with velocity dispersion larger than 175 km s^{-1} assigns them formation redshifts >1.4. Galaxies with lower velocity dispersions have instead younger ages, compatible with continuous low levels of star formation. Alternatively, the low-mass, spectroscopic early-type cluster sample is building up progressively with the acquisition of new and young objects, as discussed in De Lucia et al. (2004, 2007) and Rudnick et al. (2009). The result also agrees with the analysis of the scatter in the color−magnitude relation of EDisC clusters of Jaffé et al. (2010).

Field galaxies are slightly younger than cluster galaxies at the same redshift and mass. Taking into account the size and velocity dispersion evolution considered above in the case 6+12 pushes all formation ages upwards by 1−4 Gyr. Taking into account the progenitor bias of van Dokkum & Franx (2001) reduces the ages by 1−2 Gyr. Table 8 lists the mean ages of the HST sample of galaxies with morphologies $T < 0$. The differences between low and high mass galaxies are smaller.

We next correlated the FP ages of Fig. 25 with those derived from the analysis of the spectral indices. As performed in Sánchez-Blázquez et al. (2009), we averaged the spectra of the galaxies appearing in each mass bin shown in Fig. 18, measured the Fe4383, HdA, and CN2 indices, and recovered the ages and metallicities of SSP models that reproduce their values best. The
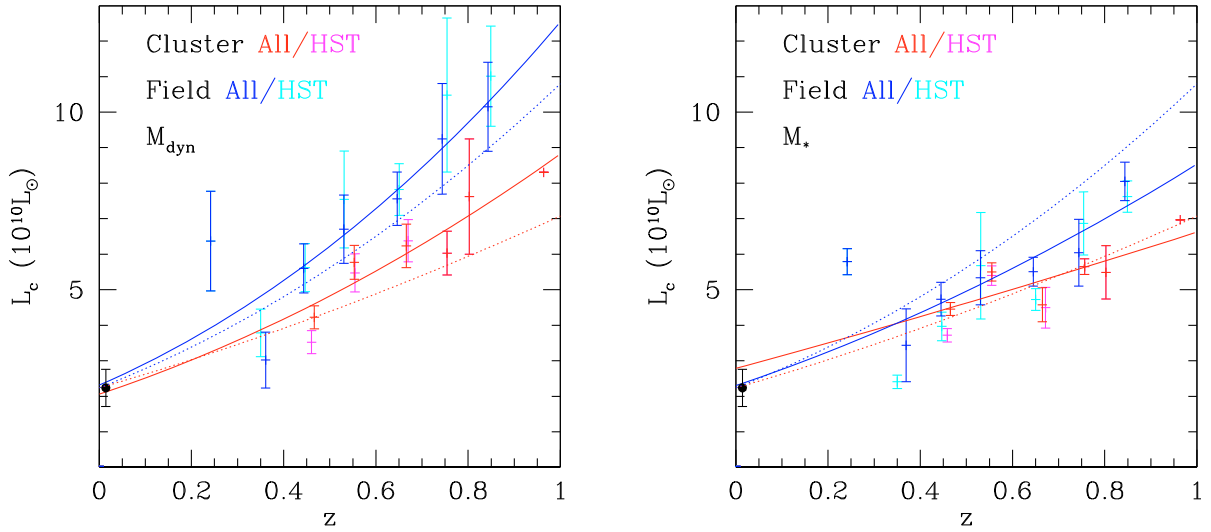
Fig. 24. The luminosity evolution with redshift of EDisCS galaxies. *Left*: L_c as a function of redshift derived using M_{dyn}. *Right*: L_c as a function of redshift derived using M_*. The full lines show the best-fit function $L_c = L_c^0 \times (1 + z)^\tau$, red for cluster and blue for field galaxies, derived for the full sample without selection weighting. The dotted lines show the corresponding redshift dependences derived from the FP analysis with $\Delta\tau = 0$ (Table 5). The black dot shows the local value derived from Faber et al. (1989).

derived metallicity averaged over the sample is solar, which justifies the choice above. We also estimated luminosity-weighted and mass-weighted ages directly by fitting the spectra with a library of model spectra. Within the large errors, there is overall agreement with the ages derived from the indices. The optimal match is achieved when considering the minimal evolution ages. As a final check, we evaluated the rest-frame $U-B$ and $B-V$ colors corresponding to a SSP of solar metallicity and age derived above and compared them to the measured averaged colors. The agreement was fair, but either the colors predicted using the FP ages are too red or the spectral ages appear to be too high. The discrepancy is exacerbated when size evolution is taken into account. This could simply reflect the known difficulties for stellar population synthesis models in reproducing the colors of real galaxies (Maraston et al. 2009).

5. Conclusions

We have examined the FP of EDisCS spectroscopic early-type galaxies, in both the cluster and the field. Combining structural parameters from HST and VLT images and velocity dispersions from VLT spectra, we have compiled a catalogue of 154 cluster and 68 field objects in the redshift range 0.2–0.9. For the first time, we have explored the FP of galaxy clusters of medium-to-low velocity dispersion in the redshift range 0.4–0.9. At face-value, on average, the evolution of the zero point follows the predictions of simple stellar population models with high (≈ 2) formation redshift for all clusters, independent of their velocity dispersion, with a slight increase (from 15% to 18%) in the scatter in mass-to-light ratios for clusters with low ($\sigma_{clus} < 600$ km s^{-1}) velocity dispersions. The FP zero point of field galaxies follows similar tracks up to redshift ≈ 0.5, but implies brighter luminosities, or lower formation redshifts at higher redshifts.

We have determined dynamical and stellar masses for our galaxies. The ratio M_{dyn}/M_* is ≈ 0.9 with a scatter of a factor of 2 and a tendency to decrease with redshift. We investigated the FP

residuals as a function of galaxy mass. At high redshifts ($z > 0.7$ for cluster galaxies, slightly below for field galaxies), galaxies with mass lower than $\approx 10^{11}$ $M_\odot$ have lower mass-to-light ratios than a passive evolution of the ZP predicts. This implies that there is a rotation in the FP: we have confirmed that for cluster galaxies the velocity dispersion coefficient α is compatible with the local value up to a redshift $z = 0.7$ and decreases to $\alpha \approx 0.7 \pm 0.4$ at higher redshifts, but this detection is of low statistical significance.

We have investigated the size and velocity dispersion evolution of our sample. At a given mass, galaxy sizes decrease and velocity dispersions increase at increasing redshift. We fitted the relations $R_e \approx (1 + z)^{-1.0 \pm 0.3}$, and $\sigma \approx (1 + z)^{0.59 \pm 0.1}$ and $\sigma \approx (1 + z)^{0.34 \pm 0.14}$ at a constant dynamical or stellar mass of 2×10^{11} $M_\odot$, respectively, for both cluster and field galaxies. However, after taking into account the progenitor bias affecting our sample (large galaxies that joined the local early-type class only recently will progressively disappear in higher redshift samples), the effective size and velocity dispersion evolution reduced substantially (to $R_e \propto (1 + z)^{-0.5 \pm 0.2}$ and $\sigma \propto (1 + z)^{0.41 \pm 0.08}$ for dynamical masses and $R_e \propto (1 + z)^{-0.68 \pm 0.4}$ and $\sigma \propto (1 + z)^{0.19 \pm 0.10}$ for stellar masses).

We computed the luminosity evolution predicted by the ZP variation with redshift of the FP when the size and velocity dispersion evolution are taken into account. The corrections computed at constant dynamical masses with a progenitor bias correction almost cancel out; at constant stellar mass, they reduce the slope of the $(1 + z)$ dependence of luminosity by -0.6 units (case 5+11 of Table 7). Fitting directly the luminosity-mass relation, we derived a luminosity evolution that agrees with the one derived from the FP analysis and does not allow for large size and velocity dispersion corrections such as those derived without taking into account the progenitor bias, where a reduction of the slope of the $(1 + z)$ dependence of luminosity by -0.8 is derived at constant M_* (case 1+9 of Table 7).

Using SSP models, we translated the variations in the FP ZP into formation ages as a function of redshift and galaxy mass.
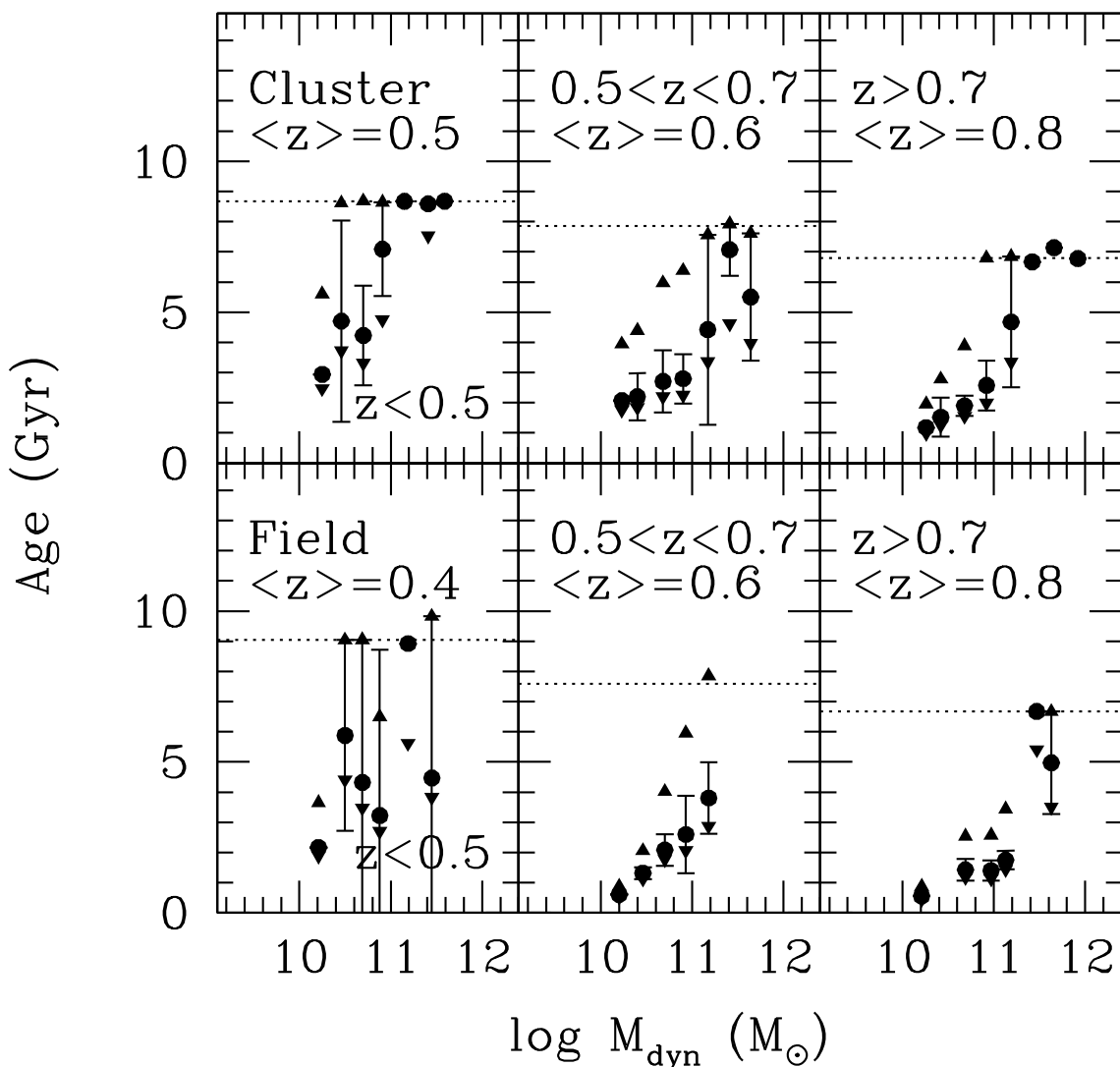
Fig. 25. The ages of cluster (*top*) and field (*bottom*) galaxies at low (*left*, $z < 0.5$ *left*), medium ($0.5 < z < 0.7$, *middle*), and high ($z > 0.7$, *right*) redshifts as a function of dynamical mass. The circles show the ages as derived from the bare FP zero-point evolution. The triangles pointing upwards take into account size evolution at constant M_*, case 3+7 (see Table 9). The triangles pointing downwards take into account the progenitor bias of van Dokkum & Franx (2001). The median redshifts are given and the corresponding ages of the universe are shown by the dotted lines.

Massive ($M > 10^{11} \ M_\odot$) cluster galaxies are old, with formation redshifts $z_f > 1.5$. In contrast, lower mass galaxies are just 2 to 3 Gyr old. This agrees with the EDisCS results presented in De Lucia et al. (2004, 2007), Poggianti et al. (2006), Sánchez-Blázquez et al. (2009), and Rudnick et al. (2009), who argue from different points of view that the lower luminosity, lower mass population of early-type galaxies comes in place only at later stages in clusters. Field galaxies at all masses are somewhat younger (by ≈ 1 Gyr) than the cluster ones with similar masses and redshifts. In general, the FP ages agree reasonably well with those derived from spectral indices.

To conclude, our analysis of the FP, size, and velocity dispersion evolution of EDisCS galaxies points towards a picture where a large fraction of the population became passive only fairly recently. The high-redshift passive galaxies are a biased subset of all present-day passive galaxies. At any probed redshift, from 0 to 1, passive galaxies are an inhomogeneous population in terms of their formation paths, and as redshift increases, a subset of the population leaves the sample, with the less massive galaxies dropping out of the sample more rapidly with redshift than the more massive ones, and at a somewhat

accelerated rate in the field. Only when these effects are taken into account may coherent estimates of the luminosity evolution of early-type galaxies from the colors, indices, and the FP zero point be derived.

References

Baldry, I. K., Glazerbrook, K., & Driver, S. P. 2008, MNRAS, 388, 945
Bell, E. F., & de Jong, R. S. 2001, ApJ, 550, 21
Bender, R., Saglia, R. P., & Gerhard, O. 1994, MNRAS, 269, 785
Bender, R., Saglia, R. P., Ziegler, B., et al. 1998, ApJ, 493, 529
Bertin, E., & Arnouts, S. 1996, A&AS, 117, 393
Bessel, M. S. 2990, PASP, 102, 1181
Biermann, P., & Shapiro, S. L. 1979, ApJ, 230, L33
Blakeslee, J. P., Franx, M., Postman, M., et al. 2003, ApJ, 596, L143
Bruzual, G., & Charlot, S. 2003, MNRAS, 344, 1000

Burstein, D., Davies, R. L., Dressler, A., et al. 1987, ApJS, 64, 601
Buitrago, F., Trujillo, I., Conselice, C. J., et al. 2008, ApJ, 687, L61
Cappellari, M., & Emsellem, E. 2004, PASP, 116, 138
Cappellari, M., Bacon, R., Bureau, M., et al. 2006, MNRAS, 366, 1126
Cappellari, M., di Serego Alighieri, S., Cimatti, A., et al. 2009, ApJ, 704, L34
Carlberg, R. G., Yee, H. K. C., Ellingson, E., et al. 1996, ApJ, 462, 32
Cenarro, A. J., & Trujillo, I. 2009, ApJ, 696, L43
Cimatti, A., Cassata, P., Pozzetti, L., et al. 2008, A&A, 482, 21
Clowe, D., Schneider, P., Aragón-Salamanca, A., et al. 2006, A&A, 451, 395
Colless, M., Saglia, R. P., Burstein, D., et al. 2001, MNRAS, 321, 277
Conroy, C., & Gunn, J. E. 2010, ApJ, 712, 833
Daddi, E., Renzini, A., Pirzkal, N., et al. 2005, ApJ, 626, 680
Damjanov, I., McCarthy, P. J., Abraham, R. G., et al. 2009, ApJ, 695, 101
de Jong, R. S., Simard, L., Davies, R. L., et al. 2004, MNRAS, 355, 1155
de Jong, R. S., & Bell, E. F. 2007, ed. R. S. de Jong (Springer), ApS&S Proc., 107
De Lucia, G., Poggianti, B. M., Aragón-Salamanca, A., et al. 2004, ApJ, 610, L77
De Lucia, G., Springel, V., White, S. D. M., Croton, D., & Kauffmann, G. 2006, MNRAS, 366, 499
De Lucia, G., Poggianti, B. M., Aragón-Salamanca, A., et al. 2007, MNRAS, 374, 809
Desai, V., Dalcanton, J. J., Aragón-Salamanca, A., et al. 2007, ApJ, 661, 1151
Di Serego Alighieri, S., Vernet, J., et al. 2005, A&A, 442, 125
Di Serego Alighieri, S., Lanzoni, B., & Jørgensen, I. 2006, ApJ, 652, L145
Djorgovski, S., & Davis, M. 1987, ApJ, 313, 59
D'Onofrio, M., Fasano, G., Varela, J., et al. 2008, ApJ, 685, 875
Dressler, A., Faber, S. M., Burstein, D., et al. 1987, ApJ, 313, L37
Dressler, A., Oemler, A., Jr., Couch, W. J., et al. 1997, ApJ, 490, 577
Edwards, S., Colless, M., Bridges, T., et al. 2002, ApJ, 567, 178
Faber, S. M., Wegner, G., Burstein, D., et al. 1989, ApJS, 69, 763
Fan, L., Lapi, A., De Zotti, G., & Danese, L. 2008, ApJ, 689, L101
Ferreras, I., Lisker, T., Pasquali, A., Khochfar, S., & Kavira, S. 2009, MNRAS, 395, 554
Fisher, D., Fabricant, D., Franx, M., & van Dokkum, P. 1998, ApJ, 498, 195
Gebhardt, K., Faber, S. M., Koo, D. C., et al. 2003, ApJ, 597, 239
Gómez, P. L., Hughes, J. P., & Birkinshaw, M. 2000, ApJ, 540, 726
Halliday, C., Milvang-Jensen, B., Poirer, S., et al. 2004, A&A, 427, 397
Hudson, M. J., Russell, J. S., Lucey, J. R., & Branchini, E. 2004, MNRAS, 352, 61
Holden, B. P., van der Wel, A., Franx, M., et al. 2005, ApJ, 620, L83
Hopkins, P. F., Hernquist, L., Cox, T. J., Keres, D., & Wuyts, S. 2009, ApJ, 691, 1424
Jaffé, Y. L., Aragón-Salamanca, A., De Lucia, G., et al. 2010, MNRAS, in press
Johnson, O., Best, D., Zaritsky, D., et al. 2006, MNRAS, 371, 1777
Jørgensen, I., Franx, M., & Kjaergaard, P. 1995, MNRAS, 276, 1341
Jørgensen, I., Franx, M., Hjorth, J., & van Dokkum, P. G. 1999, MNRAS, 308, 833
Jørgensen, I., Bergmann, M., Davies, R., et al. 2005, AJ, 129, 1249
Jørgensen, I., Chiboucas, K., Flint, K., et al. 2006, ApJ, 639, L9
Jørgensen, I., Chiboucas, K., Flint, K., et al. 2007, ApJ, 654, L179
Just, D. W., Zaritsky, D., Sand, D. J., Desai, V., & Rudnick, G. 2010, ApJ, 711, 192
Kauffmann, G. 1996, MNRAS, 281, 475
Kelson, D. D., Illingworth, G. D., van Dokkum, P. G., & Franx, M. 2000, ApJ, 531, 184
Khochfar, S., & Silk, J. 2006, ApJ, 468, L21
Kochanek, C. S., Falco, E. E., Impey, C. D., et al. 2000, ApJ, 543, 131
Le Borgne, J. F., Pello, R., & Sanahuja, B. 1992, A&AS, 95, 87
Longhetti, M., Saracco, P., Severgnini, P., et al. 2007, MNRAS, 374, L614
Lynden-Bell, D., Faber, S. M., Burstein, D., et al. 1988, ApJ, 326, 19
Mancini, C., Daddi, E., Renzini, A., et al. 2010, MNRAS, 401, 933
Maraston, C. 2005, MNRAS, 362, 799

Maraston, C., Strömback, G., Thomas, D., Wake, D. A., & Nichol, R. C. 2009, MNRAS, 394, L107
MacArthur, L. A., Ellis, R. S., Treu, T. U. V., Bundy, K., & Moran, S. 2008, ApJ, 680, 70
Mellier, Y., Soucail, G., Fort, B., & Mathez, G. 1988, A&A, 199, 13
Milvang-Jensen, B., Noll, S., Halliday, C., et al. 2008, A&A, 482, 419
Menanteau, F., Ford, H. C., Illingworth, G. D., et al. 2004, ApJ, 612. 202
Pelló, R., Rudnick, G., De Lucia, G., et al. 2009, A&A, 508, 1173
Pérez-González, P. G., Trujillo, I., Barro, G., et al.2008, ApJ, 687, 50
Poggianti, B. M., von der Linden, A., de Lucia, G., et al. 2006, ApJ, 642, 188
Rudnick, G., et al. 2003, ApJ, 599, 487
Rudnick, G., von der Linden, A., Pelló, R., et al. 2009, ApJ, 700, 1559
Saglia, R. P., Bertschinger, E., Baggley, G., et al. 1997a, ApJS, 109, 79
Saglia, R. P., Burstein, D., Baggley, G., et al. 1997b, MNRAS, 292, 499
Saglia, R. P., Colless, M., Burstein, D. et al. 2001, MNRAS, 324, 389
Saglia, R. P., Bender, R., & Dressler, A. 2003, A&A, 279, 75
Sánchez-Blázquez, P., Peletier, R. F., Jiménez-Vicente, J., et al. 2006, MNRAS, 371, 703
Sánchez-Blázquez, P., Jablonka, P., Desai, V., et al. 2009, A&A, 499, 47
Saracco, P., Longhetti, M., & Andreon, S. 2009, MNRAS, 392, 718
Shen, S., Mo, H. J., White, S. D. M., et al. 2003, MNRAS, 343, 978
Simard, L., Willmer, C. N. A., Vogt, N. P., et al. 2002, ApJS, 142, 1
Simard, L., Willmer, C. N. A., Vogt, N. P., et al. 2009, A&A, 508, 1141
Thomas, J., Saglia, R. P., Bender, R., et al. 2010, MNRAS, submitted
Toft, S., van Dokkum, P., Franx, M., et al. 2007, ApJ, 671, 285
Tran, K.-V., van Dokkum, P., Illingworth, G. D., et al. 2005, ApJ, 619, 134
Treu, T., Stiavelli, M., Bertin, G., Casertano, S., & Møller, P. 2001, MNRAS, 326, 237
Treu, T., Stiavelli, M., Casertano, S., Møller, P., & Bertin, G. 2002, ApJ, 564, L13
Treu, T., Ellis, R. S., Liao, T. X., et al. 2005a, ApJ, 633, 174
Treu, T., Ellis, R. S., Liao, T. X., & van Dokkum, P. G. 2005b, ApJ, 622, L5
Trujillo, I., Förster Schreiber, N. M., Rudnick, G., et al. 2006, ApJ, 650, 18
Trujillo, I., Conselice, C. J., Bundy, K., et al. 2007, MNRAS, 382, 109
Valentinuzzi, T., Fritz, J., Poggianti, B. M., et al. 2010a, ApJ, 712, 226
Valentinuzzi, T., Poggianti, B. M., Saglia, R. P., et al. 2010b, ApJ, 721, L19
van der Marel, R., & van Dokkum, P. G. 2007a, ApJ, 668, 738
van der Marel, R., & van Dokkum, P. G. 2007b, ApJ, 668, 756
van der Wel, A., Franx, M., van Dokkum, P. G., & Rix, H.-W. 2004, ApJ, 601, L5
van der Wel, A., Franx, M., van Dokkum, P. G., et al. 2005, ApJ, 631, 145
van der Wel, A., Holden, B. P., Zirm, A. W., et al. 2008, ApJ, 688, 48
van Dokkum, P. G., & Franx, M. 1996, MNRAS, 281, 985
van Dokkum, P. G., & Franx, M. 2001, ApJ, 553, 90
van Dokkum, P. G., & Stanford S. A. 2003, ApJ, 585, 78
van Dokkum, P. G., & van der Marel, R. 2007, ApJ, 655, 30
van Dokkum, P. G., Franx, M., Kelson, D. D., & Illingworth, G. D. 1998, ApJ, 504, L17
van Dokkum, P. G., Franx, M., Fabricant, D., et al. 2000, ApJ, 541, 95
van Dokkum, P. G., Franx, M., Kelson, D. D., & Illingworth, G. D. 2001, ApJ, 553, L39
van Dokkum, P. G., Franx, M., Kriek, M., et al. 2008, ApJ, 667, L5
van Dokkum, P. G., Kriek, M., & Franx, M. 2009, Nature, 460, 717
van Dokkum, P. G., Whitaker, K. E., Brammer, G., et al. 2010, ApJ, 709, 1018
Vazdekis, A., Sánchez-Blázquez, P., Falcón-Barroso, J., et al. 2010, MNRAS, 404, 1639
White, S. D. M., Aragón-Salamanca, A., Bender, R., et al. 2005, A&A, 444, 365
Wuyts, S., van Dokkum, P. G., Kelson, D. D., Franx, M., & Illingworth, G. D. 2004, ApJ, 605, 677
Zaritsky, D., Zabludoff, A. I., & Gonzalez, A. H. 2008, ApJ, 682, 68
Ziegler, B. L., Thomas, D., Böhm, A., et al. 2005, A&A, 433, 519
Zirm, A. W., van der Wel, A., Franx, M., et al. 2007, ApJ, 656, 66

1 Max-Planck Institut für extraterrestrische Physik, Giessenbachstraße, 85741 Garching, Germany
   e-mail: saglia@mpe.mpg.de
2 Universitäts-Sternwarte München, Scheinerstr. 1, 81679 München, Germany
3 Departamento de Fisica Teorica, Universidad Autonoma de Madrid, 28049 Madrid, Spain
4 Departamento de Astrofísica, Universidad de La Laguna, 38205 La Laguna, Tenerife, Spain
5 Herzberg Institute of Astrophysics, National Research Council of Canada, Victoria, BC V9E 2E7, Canada
6 *Spitzer* Science Center, Caltech, Pasadena CA91125, USA
7 School of Physics and Astronomy, University of Nottingham, University Park, Nottingham NG7 2RD, UK
8 Dark Cosmology Centre, Niels Bohr Institute, University of Copenhagen, Juliane Maries Vej 30, 2100 Copenhagen, Denmark
9 Osservatorio Astrofisico di Arcetri, Largo Enrico Fermi 5, 50125 Firenze, Italy
10 Observatoire de Genève, Laboratoire d'Astrophysique Ecole Polytechnique Federale de Lausanne (EPFL), 1290 Sauverny, Switzerland
11 GEPI, Observatoire de Paris, CNRS UMR 8111, Université Paris Diderot, 92125 Meudon Cedex, France
12 Institut für Astro- und Teilchenphysik, Universität Innsbruck, Technikerstr.25/8, 6020 Innsbruck, Austria
13 Osservatorio Astronomico, vicolo dell'Osservatorio 5, 35122 Padova, Italy
14 Ohio University, Department of Physics and Astronomy, Clippinger Labs 251B, Athens, OH 45701, USA
15 INAF, Astronomical Observatory of Trieste, via Tiepolo 11, 34143 Trieste, Italy
16 Laboratoire d'Astrophysique de Toulouse-Tarbes, CNRS, Université de Toulouse, 14 avenue Edouard Belin, 31400-Toulouse, France
17 The University of Kansas, Malott room 1082, 1251 Wescoe Hall Drive, Lawrence, KS 66045, USA
18 Astronomy Department, University of Padova, Vicolo dell'Osservatorio 3, 35122 Padova, Italy
19 Max-Planck-Institut für Astrophysik, Karl-Schwarzschild-Str. 1, Postfach 1317, 85741 Garching, Germany
20 Steward Observatory, University of Arizona, 933 North Cherry Avenue, Tucson, AZ 85721

Appendix A: Circularized half-luminosity radii

GIM2D delivers bulge a_e and disk a_h scale lengths along the major axis, bulge apparent flattening $(b/a)_B$ and disk inclination angles i (corresponding to an apparent flattening $(b/a)_D = 1 - \cos i$), and bulge-to-total ratios B/T. When fitting Sersic profiles, GIM2D delivers the n Sersic index, the major axis a_e^{Ser}, and the flattening $(b/a)^{Ser}$. We compute the circularized half-luminosity radius R_e of the resulting galaxy model as follows. We determine the flux inside a circular aperture of radius R (the so-called curve of growth) of a model of apparent flattening b/a and surface density distribution constant on ellipses $f(x, y) = f(\sqrt{x^2/a^2 + y^2/b^2})$ as

$$F(R) = \int_0^{2\pi} \int_0^R f(\sqrt{(R'\cos\phi)^2/a^2 + (R'\sin\phi)^2/b^2}\,R'dR'd\phi. \quad \text{(A.1)}$$

Using $F_c(R) = 2\pi \int_0^R r f(r) dr$, we derive

$$F(R) = 4b^2 \int_0^{\pi/2} \frac{F_c(r/b\sqrt{1 - (1 - b^2/a^2)\cos^2\phi})}{1 - (1 - b^2/a^2)\cos^2\phi} d\phi. \quad \text{(A.2)}$$

We perform the angular integration numerically, using $F_c^{deVauc}(z) = 1 - (1 + \sum_{i=1}^{7} z^i/i!)e^{-z}$, where $z = 7.67(r/R_{eB})^{1/4}$, and $F_c^{exp}(x) = 1 - (1 + x)e^{-x}$, and $x = R/h$ for the normalized de Vaucouleurs and exponential density laws, respectively. For a Sersic profile of given n, we use $F_c^n = P(2n, X)$, where P is the incomplete Γ function and $X = k(r/R_{eSer})^{1/n}$ and $k = 1.9992n - 0.3271$ (Simard et al. 2002). We determine R_e by solving the equation

$$B/T \times F^{deVauc}(R_e) + (1 - B/T)F^{exp}(R_e) = 0.5 \quad \text{(A.3)}$$

for the bulge-plus-disk models, and

$$F^n(R_e) = 0.5 \quad \text{(A.4)}$$

for the Sersic fits numerically. In general, the resulting R_e agree within 1% with the half-luminosity radii derived by measuring the curves of growth directly from (ACS HST like) images generated by GIM2D with the fit parameters and no PSF convolution, but the image-based method overestimates R_e by up to 10% when it is smaller than 4 pixels (0.2 arcsec).

Figure A.1 illustrates that a more accurate approximation of the circularized radius R_e(Ser) of Sersic profiles, more accurate than 2%, is obtained by taking the simple mean $R_{ave} = (a_e + b_e)/2$ of the major and minor axis scale lengths a_e and b_e instead of the harmonic mean $R_{har} = \sqrt{a_e \times b_e}$. This is surprising only at a first sight, since R_{har} goes to zero as the flattening increases,
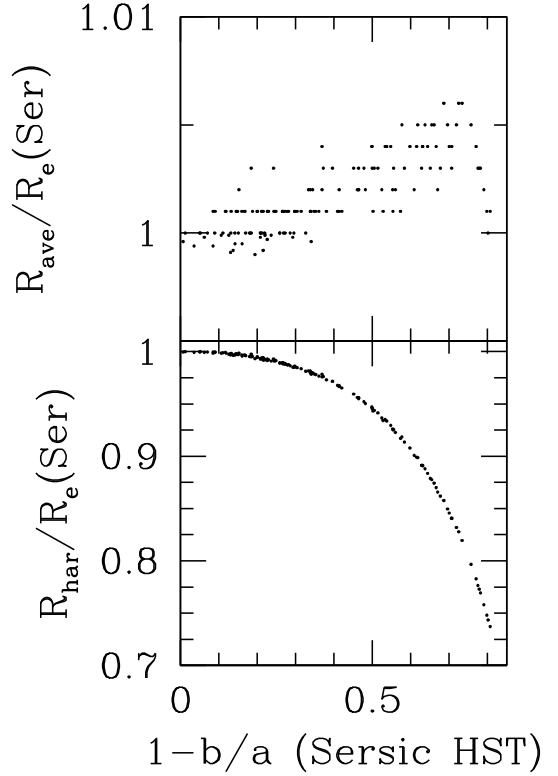
Fig. A.1. The circularized half-luminosity radius R_e(Ser) of the sample of EDisCS galaxies with HST photometry and velocity dispersions computed according to Eqs. (A.2) and (A.4) compared to the simple mean $R_{ave} = 0.5(a_e + b_e)$ (*top*) and harmonic mean $R_{har} = \sqrt{a_e \times b_e}$ (*bottom*) as a function of the ellipticity $1 - b_e/a_e$. The simple mean approximates more accurately R_e(Ser).

while R_{ave} does not. Therefore R_{ave} should provide a closer approximation of the half-luminosity radius derived from circular curves of growth at high ellipticities. On the other hand, the effective surface brightness within the ellipse of semi-major and minor axis a_e and b_e is constant regardless of the flattening, while this is not true for the surface brightness within the circle of radius R_e(Ser). Since in this exercise the total luminosity L is kept constant, we have $\log R_e(Ser)/R_{har} = 0.2(\langle SB_e \rangle - \langle SB_e^{har} \rangle)$, with $\langle SB_e \rangle = -2.5 \log \frac{L}{2\pi R_e(Ser)^2}$ and $\langle SB_e^{har} \rangle = -2.5 \log \frac{L}{2\pi R_{har}^2}$. This is almost orthogonal to the FP (see Eq. (1)), making the choice of method unimportant, as long as not too many disks seen edge-one (i.e. of very high flattening) are present in the sample (see Fig. 5 and discussion in Sect. 2.2).

Table 1. The FP parameters of cluster galaxies.

Name	N_{clus}	z	S Type	σ_{mes} (km s^{-1})	σ_{cor} (km s^{-1})	dσ (km s^{-1})	R_{e} (kpc)	$\log I_{\text{e}}$ $\log L_\odot/\text{pc}^2$	T Type	P_{S}	$\log M_*$ $\log M_\odot$	dlog M_* $\log M_\odot$
EDCSNJ1040403-1156042	9	0.702	1	161.3	167.1	13.6	5.147	2.092	−5	0.199	11.54	0.06
EDCSNJ1040407-1156015	9	0.703	1	155.9	161.5	15.4	1.698	2.807	−2	0.149	11.28	0.05
EDCSNJ1040346-1157566	9	0.7024	1	148.9	154.3	17.8	2.9	2.404	−5	0.161	11.25	0.08
EDCSNJ1040396-1155183	9	0.7046	2	226.2	234.4	13.4	1.789	2.68	−5	0.096	11.09	0.09
EDCSNJ1040356-1156026	9	0.7081	2	172.7	178.9	8.4	2.123	2.703	−5	0.304	11.35	0.12
EDCSNJ1054244-1146194	8	0.6965	1	230.2	238.5	19.5	4.614	2.307	−5	0.150	11.72	0.05
EDCSNJ1054250-1146238	8	0.6968	1	221.8	229.8	18	3.194	2.477	−5	0.196	11.53	0.06
EDCSNJ1054309-1147095	8	0.6998	1	193.5	200.5	16.9	2.452	2.396	−5	0.150	11.04	0.08
EDCSNJ1054263-1148407	8	0.7014	1	256.8	266	15	4.047	1.98	1	0.129	11.09	0.08
EDCSNJ1054338-1149299	8	0.6945	1	205.3	212.7	17.4	3.45	2.393	−5	0.172	11.4	0.06
EDCSNJ1054280-1149598	8	0.6964	1	134.2	139	10.9	1.527	2.635	−5	0.112	11.8	0.03
EDCSNJ1054296-1147123	8	0.6981	2	214.1	221.8	16.8	2.336	2.707	−5	0.245	11.45	0.05
EDCSNJ1054278-1149580	8	0.6949	2	191.4	198.3	14.6	3.95	2.428	1	0.271	11.4	0.44
EDCSNJ1054305-1146536	8	0.6986	2	256.7	265.9	10.5	6.945	2.15	−5	0.295	11.71	0.15
EDCSNJ1054303-1149132	8	0.6964	2	250.9	259.9	13.9	4.592	2.22	−5	0.254	11.7	0.06
EDCSNJ1054237-1146107	8	0.6962	2	135.8	140.7	20	0.9097	2.755	−5	0.077	10.7	0.08
EDCSNJ1054246-1146124	8	0.7034	1	228.6	236.8	34.3	5.657	1.805	4	0.126	11.1	0.15
EDCSNJ1054467-1245035	10	0.7304	1	142.3	147.5	13.7	1.774	2.716	1	0.141	11.06	0.10
EDCSNJ1054435-1245519	10	0.7503	1	359.1	372.4	33.9	7.076	2.031	−5	0.129	11.65	0.04
EDCSNJ1054451-1247336	10	0.7305	1	195.8	203	17.3	1.371	2.872	−2	0.140	11.01	0.04
EDCSNJ1054436-1244202	10	0.7463	1	187.9	194.8	24.9	0.9712	3.22	−2	0.142	11.01	0.05
EDCSNJ1054438-1245409	10	0.7568	1	205.4	213	24.2	1.396	2.991	−5	0.146	11.27	0.04
EDCSNJ1054445-1246173	10	0.7498	2	325.4	337.5	40.9	1.311	2.741	1	0.077	10.92	0.04
EDCSNJ1054440-1246390	10	0.7496	1	163.1	169.1	23	1.601	2.539	1	0.074	10.92	0.05
EDCSNJ1054442-1245331	10	0.7446	1	209.5	217.2	38.9	1.267	2.327	−2	0.008	10.18	0.07
EDCSNJ1054439-1245556	10	0.7531	2	119.4	123.8	16.5	2.203	2.454	−2	0.126	10.98	0.05
EDCSNJ1054398-1246055	10	0.7482	2	154.8	160.5	12.7	4.38	2.428	1	0.121	11.45	0.07
EDCSNJ1054396-1248241	10	0.7478	2	209.6	217.4	39.7	3.572	2.204	1	0.136	11.06	0.06
EDCSNJ1054431-1246205	10	0.7553	2	234.7	243.4	42.7	4.66	1.64	4	0.047	11	0.08
EDCSNJ1216470-1159267	12	0.7971	1	170.8	177.3	15.6	2.469	2.47	1	0.204	10.91	0.06
EDCSNJ1216454-1200017	12	0.7996	1	260.4	270.3	14.4	1.938	2.6	−5	0.204	11.12	0.07
EDCSNJ1216490-1200091	12	0.7863	1	255	264.6	44	2.737	2.369	1	0.208	11.07	0.07
EDCSNJ1216453-1201176	12	0.7955	1	293.1	304.2	19.9	10.09	1.972	1	0.323	11.82	0.05
EDCSNJ1216420-1201509	12	0.7941	1	273.7	284.1	19.5	3.208	2.692	−5	0.301	11.59	0.07
EDCSNJ1216468-1202226	12	0.7987	1	135.8	141	14.3	4.333	2.149	−2	0.230	11.18	0.05
EDCSNJ1216401-1202352	12	0.8022	1	214.9	223.1	15.4	1.327	3.176	−2	0.270	11.23	0.07
EDCSNJ1216462-1200073	12	0.7847	1	122.3	126.9	21.8	0.9628	3.026	−5	0.034	10.72	0.06
EDCSNJ1216418-1200449	12	0.7967	1	155.5	161.4	10.5	3.027	2.304	−2	0.208	11.15	0.06
EDCSNJ1216438-1200536	12	0.7945	1	282.2	292.9	22.5	2.414	2.728	−5	0.274	11.47	0.04
EDCSNJ1216461-1201143	12	0.7997	1	240.4	249.5	10	4.545	2.477	−5	0.295	11.71	0.05
EDCSNJ1216456-1201080	12	0.8058	1	122.4	127.1	15.9	4.794	2.018	−5	0.209	11.31	0.04
EDCSNJ1216453-1201209	12	0.8054	1	198.2	205.8	24.1	3.969	2.209	2	0.237	11.45	0.06
EDCSNJ1216443-1201429	12	0.7918	1	132.2	137.2	22.7	1.73	2.647	−5	0.282	11.42	0.05
EDCSNJ1216438-1202155	12	0.8028	1	255.3	265	23.9	0.6319	3.291	−2	0.010	10.69	0.07
EDCSNJ1216417-1203054	12	0.8012	1	167.5	173.9	17.2	0.8983	3.397	−2	0.233	10.83	0.06
EDCSNJ1216359-1200294	12	0.793	1	206.2	214	31.5	0.9888	3.221	−2	0.211	11.05	0.05
EDCSNJ1216446-1201089	12	0.8001	1	317.3	329.4	32.6	1.668	2.638	−5	0.145	11.01	0.06
EDCSNJ1216449-1201203	12	0.8035	1	176.6	183.3	12	2.72	2.457	−5	0.218	11.65	0.05
EDCSNJ1216403-1202029	12	0.7976	1	316.2	328.2	31.5	2.62	2.089	1	0.021	10.75	0.08
EDCSNJ1216522-1200595	12	0.7882	2	113.8	118.1	7	1.45	2.607	−2	0.057	10.8	0.07
EDCSNJ1216382-1202517	12	0.79	2	238.3	247.3	20.7	3.737	2.365	−5	0.250	11.28	0.07
EDCSNJ1216387-1201503	12	0.8008	1	290.4	301.4	32.3	1.233	3.091	−2	0.221	11.15	0.04
EDCSNJ1232318-1249049	4	0.5408	1	145.7	150.2	19.5	1.883	2.363	−5	0.092	10.73	0.10
EDCSNJ1232280-1249353	4	0.5449	1	316.7	326.6	21.3	3.797	2.314	5	0.171	11.37	0.09
EDCSNJ1232303-1250364	4	0.5419	1	329.2	339.5	24.9	14.03	1.621	−5	0.147	11.86	0.08
EDCSNJ1232250-1251551	4	0.5399	1	120.9	124.7	17.3	2.082	2.503	3	0.160	10.78	0.16
EDCSNJ1232287-1252369	4	0.5432	1	264.9	273.2	11.3	2.448	2.479	1	0.268	11.23	0.08
EDCSNJ1232271-1253013	4	0.5445	1	243.4	251	21.4	2.244	2.462	−5	0.174	11.04	0.12
EDCSNJ1232343-1249265	4	0.5395	1	196.3	202.4	16.7	1.198	2.872	−2	0.163	10.93	0.12
EDCSNJ1232350-1250103	4	0.5397	1	212.1	218.7	13.2	4.001	2.14	−5	0.268	11.09	0.11

Table 1. continued.

Name	N_{clus}	z	S Type	σ_{mes} (km s^{-1})	σ_{cor} (km s^{-1})	dσ (km s^{-1})	R_e (kpc)	log I_e log $L_\odot$/pc^2	T Type	P_S	log M_* log $M_\odot$	dlog M_* log $M_\odot$
EDCSNJ1232313-1250327	4	0.5496	1	162.6	167.7	18.5	1.373	2.549	−5	0.084	10.82	0.12
EDCSNJ1232317-1249275	4	0.542	1	138.2	142.5	13.1	4.564	2.143	1	0.238	11.21	0.10
EDCSNJ1232309-1249408	4	0.5485	1	251.6	259.5	22.9	3.559	2.485	−2	0.071	11.57	0.05
EDCSNJ1232303-1251092	4	0.5428	1	140.8	145.2	25.1	1.128	2.613	−2	0.085	10.59	0.11
EDCSNJ1232303-1251441	4	0.55	1	169.9	175.2	19.8	1.976	2.331	3	0.103	10.8	0.11
EDCSNJ1232370-1248239	4	0.5401	1	142.1	146.5	7.7	1.812	2.612	−2	0.163	11.02	0.12
EDCSNJ1232372-1249258	4	0.5377	1	219.4	226.2	29.9	0.8342	2.688	1	0.023	10.4	0.12
EDCSNJ1232296-1250119	4	0.5509	1	135.1	139.4	9.3	3.48	2.242	3	0.252	11.22	0.11
EDCSNJ1232301-1250362	4	0.5424	1	218.4	225.2	29.5	2.542	2.039	−5	0.119	10.87	0.08
EDCSNJ1232288-1250490	4	0.547	1	164.7	169.9	6.4	2.121	2.55	−2	0.215	11.18	0.11
EDCSNJ1232299-1251034	4	0.5493	1	207.4	213.9	14.7	1.452	2.555	−5	0.092	10.73	0.09
EDCSNJ1232207-1252016	4	0.5416	1	238.9	246.3	17.7	5.822	2.076	−5	0.140	11.6	0.08
EDCSNJ1232204-1249547	4	0.546	2	245.7	253.4	18.2	3.916	2.278	3	0.187	11.33	0.09
EDCSNJ1037527-1243456	5	0.5807	2	262.5	271	20.1	1.206	2.841	−5	0.089	10.98	0.07
EDCSNJ1037548-1245113	5	0.5789	2	187.3	193.4	13.6	1.618	2.934	−5	0.129	11.3	0.06
EDCSNJ1037447-1246050	5	0.4222	1	106	108.7	11.6	1.288	2.373	−5	0.129	10.67	0.07
EDCSNJ1037552-1246368	1	0.4245	1	175.8	180.3	11.6	1.529	2.295	−2	0.141	10.74	0.09
EDCSNJ1037535-1241538	5	0.5789	2	257.9	266.3	14.8	3.322	2.012	1	0.076	11.07	0.07
EDCSNJ1037525-1243541	5	0.5772	1	182.7	188.6	5	1.56	2.724	2	0.138	11.04	0.06
EDCSNJ1037428-1245573	1	0.4225	1	142.9	146.6	7.2	2.778	2.109	2	0.219	11.06	0.06
EDCSNJ1037527-1244485	1	0.4223	2	223.7	229.4	9.3	2.183	2.367	−2	0.123	10.98	0.09
EDCSNJ1037473-1246245	1	0.4229	1	193.7	198.7	23.7	1.326	2.347	−5	0.102	10.7	0.13
EDCSNJ1103365-1244223	18	0.7031	2	268.7	278.4	11.1	6.336	2.189	3	0.306	11.95	0.08
EDCSNJ1103372-1245215	7	0.6251	1	160.5	166	8.9	2.113	2.447	−5	0.154	10.98	0.10
EDCSNJ1103363-1246220	7	0.6288	1	164.1	169.7	10.5	2.71	2.182	2	0.172	11.17	0.13
EDCSNJ1103444-1245153	17	0.964	1	284.5	296	49.3	2.097	2.918	−5	0.085	11.43	0.04
EDCSNJ1103349-1246462	7	0.6257	2	231.7	239.6	10	6.083	2.004	−5	0.264	11.54	0.07
EDCSNJ1103413-1244379	18	0.7038	2	148.8	154.2	28.1	2.272	2.527	−5	0.130	11.21	0.08
EDCSNJ1103357-1246398	7	0.6278	1	270.9	280.1	33.6	1.564	2.545	1	0.159	10.94	0.08
EDCSNJ1138068-1132285	3	0.4787	2	134.9	138.7	24.2	3.589	1.75	3	0.114	10.85	0.21
EDCSNJ1138102-1133379	3	0.4801	1	224	230.4	9.1	5.841	1.937	−2	0.294	11.51	0.11
EDCSNJ1138069-1134314	3	0.4819	1	220.4	226.7	14.1	1.539	2.62	−5	0.157	10.9	0.10
EDCSNJ1138074-1137138	2	0.4528	2	256.6	263.6	20	3.661	2.181	−2	0.318	11.21	0.08
EDCSNJ1138104-1133319	3	0.4844	1	159.5	164.1	24.9	2.675	1.824	−2	0.175	10.6	0.14
EDCSNJ1138107-1133431	3	0.4764	1	262.8	270.3	15.3	1.523	2.52	1	0.169	11	0.12
EDCSNJ1138127-1134211	3	0.4804	1	172.8	177.7	25	0.9325	2.673	−5	0.175	10.56	0.23
EDCSNJ1138116-1134448	2	0.4571	1	157.9	162.2	8.9	1.285	2.727	−2	0.171	10.85	0.12
EDCSNJ1138069-1132044	3	0.4798	2	177.4	182.5	8.1	1.589	2.428	−2	0.123	10.84	0.11
EDCSNJ1138130-1132345	3	0.4791	1	127.4	131	8.3	2.788	2.004	3	0.198	10.88	0.13
EDCSNJ1138110-1133411	3	0.4825	1	115	118.3	13.7	2.681	1.936	3	0.158	10.78	0.19
EDCSNJ1138022-1135459	2	0.4541	1	171.9	176.6	7	2.59	2.278	2	0.228	11.06	0.12
EDCSNJ1138065-1136018	2	0.4561	1	165	169.5	29.9	3.729	1.471	4	0.159	10.74	0.21
EDCSNJ1138031-1134278	2	0.4549	1	231.2	237.5	16.7	1.163	2.602	−2	0.195	10.69	0.12
EDCSNJ1354098-1231098	11	0.7568	2	141.9	147.2	11.8	1.002	2.84	−2	0.049	10.73	0.04
EDCSNJ1354098-1231015	11	0.7562	2	310.3	321.8	8.3	5.41	2.195	1	0.130	11.7	0.06
EDCSNJ1354097-1230579	11	0.7565	1	300.9	312.1	8.5	1.89	2.864	−5	0.110	11.32	0.05
EDCSNJ1354026-1230127	6	0.5942	1	152.1	157.1	11.4	1.312	2.661	−5	0.069	10.72	0.08
EDCSNJ1354114-1230452	6	0.5947	2	141	145.7	7.2	4.694	2.168	2	0.128	11.11	0.17
EDCSNJ1354159-1232272	6	0.5929	1	191.7	198	12.5	0.672	3.041	−5	0.027	10.57	0.10
EDCSNJ1354102-1230527	11	0.7593	2	293.1	304	53.7	7.373	1.648	3	0.108	11.36	0.08
EDCSNJ1354101-1231041	11	0.7612	1	314.3	326	9.4	1.691	2.73	−2	0.117	11.16	0.06
EDCSNJ1354204-1234286	6	0.6006	1	249.3	257.6	14.8	2.212	2.61	−5	0.121	11.35	0.56
EDCSNJ1354106-1230499	11	0.7634	1	198.4	205.8	11.2	1.896	2.703	−5	0.120	11.1	0.05
EDCSNJ1018471-1210513	14	0.4716	2	197.1	202.6	15.8	4.213	1.969	−	0.343	11.16	0.12
EDCSNJ1018464-1211205	14	0.4717	1	115.5	118.8	22.3	1.243	2.6	−	0.133	10.78	0.06
EDCSNJ1018467-1211527	14	0.4716	1	236.2	242.8	9.7	14.77	1.493	*	0.000	11.85	0.08
EDCSNJ1018489-1211357	14	0.4779	1	172.9	177.8	19.4	3.588	1.997	−	0.193	10.87	0.07
EDCSNJ1018474-1211537	14	0.4746	1	284.8	292.9	40.3	1.33	2.785	*	0.000	11	0.09
EDCSNJ1018464-1211392	14	0.4696	1	179	184	15	0.8029	2.811	−	0.094	10.61	0.08
EDCSNJ1018470-1212483	14	0.4704	1	177.9	182.9	26.9	0.6736	2.935	−	0.088	10.44	0.07
EDCSNJ1059100-1251390	13	0.4517	2	164	168.5	5.5	5.845	1.885	*	0.000	11.42	0.07

Table 1. continued.

Name	N_{clus}	z	S Type	σ_{mes} (km s^{-1})	σ_{cor} (km s^{-1})	dσ (km s^{-1})	R_e (kpc)	$\log I_e$ $\log L_\odot/pc^2$	T Type	P_S	$\log M_*$ $\log~M_\odot$	d$\log M_*$ $\log~M_\odot$
EDCSNJ1059107-1253020	13	0.4552	1	169.2	173.8	21	0.8354	2.711	–	0.080	10.53	0.11
EDCSNJ1059096-1253197	13	0.455	2	214	219.8	17.6	8.433	1.665	*	0.000	11.46	0.10
EDCSNJ1059053-1255535	13	0.4572	2	204.4	210	19.2	3.187	2.057	–	0.196	10.84	0.10
EDCSNJ1059046-1251583	13	0.4561	1	115.9	119.1	14.3	2.335	2.243	–	0.199	10.87	0.11
EDCSNJ1059093-1253065	13	0.4537	1	270.4	277.8	30.9	4.667	1.405	–	0.058	10.49	0.14
EDCSNJ1059075-1253351	13	0.4565	1	242.3	248.9	10.9	9.692	1.559	*	0.000	11.42	0.09
EDCSNJ1059069-1253531	13	0.4573	1	147.1	151.1	17.1	1.617	2.478	–	0.129	10.74	0.13
EDCSNJ1059102-1254115	13	0.4598	1	200.2	205.7	8.7	1.412	2.785	–	0.283	11.07	0.09
EDCSNJ1059135-1254337	13	0.4559	1	146.3	150.3	9.9	1.719	2.577	*	0.000	11.05	0.10
EDCSNJ1059106-1253118	13	0.4511	1	111.5	114.5	16.5	3.44	1.779	–	0.079	10.52	0.13
EDCSNJ1059102-1253260	13	0.4559	1	140.7	144.6	12.9	3.53	2.04	*	0.000	11.13	0.09
EDCSNJ1059104-1253211	13	0.4553	1	263.7	270.9	10.3	3.783	2.007	*	0.000	11.19	0.07
EDCSNJ1059022-1253465	13	0.4582	2	317.6	326.3	21.1	80.52	0.08597	*	0.000	11.63	0.11
EDCSNJ1059060-1253574	13	0.4559	1	271.7	279.1	10.3	4.227	2.172	–	0.118	11.34	0.09
EDCSNJ1059086-1255576	13	0.4515	2	114.3	117.4	22.3	3.303	1.995	–	0.145	10.65	0.38
EDCSNJ1119168-1130290	19	0.5491	1	288	297.1	10.9	3.975	2.342	*	0.000	11.37	0.11
EDCSNJ1119166-1130442	19	0.551	1	152.8	157.6	15.7	0.7064	3.469	–	0.138	10.93	0.08
EDCSNJ1119165-1130541	19	0.5492	1	283.3	292.2	29.1	0.7822	3.229	–	0.127	10.98	0.17
EDCSNJ1119173-1129304	19	0.5482	1	150.8	155.5	16.6	0.4868	3.885	*	0.000	11.12	0.11
EDCSNJ1119173-1129425	19	0.5503	1	265.9	274.3	16.4	2.785	2.464	–	0.196	11.23	0.08
EDCSNJ1119168-1129376	19	0.5497	1	111.2	114.7	17.9	4.054	1.97	*	0.000	11.39	0.21
EDCSNJ1202411-1222495	20	0.4267	1	128.3	131.6	16.9	4.259	1.868	*	0.000	11.16	0.12
EDCSNJ1202430-1223461	20	0.4244	1	188.9	193.7	23.4	0.1114	4.404	–	0.058	10.41	0.15
EDCSNJ1202430-1224044	20	0.4228	2	157.3	161.3	25.5	3.179	1.873	–	0.194	10.73	0.15
EDCSNJ1202433-1224301	20	0.4246	1	239.9	246.1	11.3	10.98	1.473	*	0.000	11.48	0.13
EDCSNJ1202432-1224227	20	0.423	1	170	174.3	27.1	1.801	2.303	*	0.000	10.78	0.13
EDCSNJ1202478-1226383	20	0.4244	1	150.3	154.2	9.4	2.206	2.397	–	0.198	10.9	0.12
EDCSNJ1227589-1135135	16	0.6375	1	211.1	218.3	7.7	12.29	1.484	*	0.000	11.55	0.07
EDCSNJ1227539-1138173	16	0.6339	2	142.4	147.3	19.1	5.542	1.768	*	0.000	11.04	0.13
EDCSNJ1227531-1138340	16	0.6345	1	137.4	142.1	12.1	1.235	2.79	*	0.000	10.76	0.08
EDCSNJ1227587-1135089	16	0.641	1	155.8	161.2	12.1	0.9511	3.167	*	0.000	10.94	0.08
EDCSNJ1227541-1138174	16	0.6345	2	219.1	226.6	12.7	8.193	1.58	*	0.000	11.67	0.09
EDCSNJ1227447-1140544	21	0.5822	1	119.6	123.5	14.7	0.9498	2.759	–	0.026	10.66	0.10
EDCSNJ1228003-1135243	16	0.6376	2	105.2	108.8	16.9	1.843	2.354	–	0.065	10.5	0.16
EDCSNJ1227551-1136202	16	0.639	1	233.7	241.7	17.6	1.955	2.387	–	0.166	10.88	0.12
EDCSNJ1227537-1138210	16	0.6309	1	139.9	144.7	21.5	3.299	2.038	*	0.000	10.79	0.08
EDCSNJ1227581-1135364	16	0.6383	1	166	171.7	10.1	1.692	2.733	–	0.140	11.13	0.08
EDCSNJ1227566-1136545	16	0.6391	2	124.7	129	8.8	1.267	2.642	–	0.167	10.87	0.06
EDCSNJ1238330-1144307	22	0.4606	1	408.4	419.7	64.3	6.26	2.03	*	0.000	11.76	0.14
EDCSNJ1301351-1138356	24	0.3976	1	225.8	231.2	17	12.06	1.517	*	0.000	11.71	0.09
EDCSNJ1301372-1139069	24	0.394	1	124.8	127.8	22.8	1.598	2.29	*	0.000	10.65	0.14
EDCSNJ1301402-1139229	23	0.4828	1	271.9	279.7	17.7	12.96	1.565	*	0.000	11.73	0.08
EDCSNJ1301420-1139379	23	0.4835	1	150.7	155	19.9	1.236	2.679	–	0.209	10.78	0.12
EDCSNJ1301414-1140081	23	0.4792	1	105.1	108.1	15.9	3.116	2.147	*	0.000	11.17	0.09
EDCSNJ1301302-1138187	23	0.4856	2	218.9	225.2	15.7	2.982	2.27	*	0.000	11.05	0.09
EDCSNJ1301304-1138266	23	0.4893	2	113.9	117.2	17	3.828	2.214	*	0.000	11.17	0.11
EDCSNJ1301397-1139048	23	0.4795	1	247.9	255	12.9	3.069	2.448	–	0.140	11.45	0.06
EDCSNJ1353021-1135395	25	0.5887	1	177.3	183.1	14.2	8.501	1.745	*	0.000	11.42	0.05
EDCSNJ1353017-1137285	25	0.5889	1	240.7	248.6	12.7	14.44	1.607	*	0.000	11.83	0.05
EDCSNJ1353055-1137581	25	0.5916	1	112.8	116.5	22.4	3.35	2.094	–	0.076	10.72	0.09
EDCSNJ1353019-1137290	25	0.5877	1	292.2	301.8	24.8	5.367	2.19	*	0.000	11.57	0.04
EDCSNJ1352599-1138256	25	0.5892	1	158.8	164	21.3	0.7164	3.018	–	0.067	10.75	0.06
EDCSNJ1352562-1136567	25	0.5865	1	165.8	171.2	16.5	2.833	2.479	–	0.250	11.2	0.04
EDCSNJ1411078-1146452	26	0.5191	1	157	161.8	14.7	1.906	2.51	–	0.113	10.94	0.12
EDCSNJ1411047-1148287	26	0.52	1	230	237	13.9	11.54	1.753	*	0.000	11.75	0.06
EDCSNJ1411038-1151014	26	0.5214	1	144.1	148.5	15.5	2.81	2.192	–	0.113	10.74	0.10
EDCSNJ1411160-1151292	26	0.5199	1	210.7	217.1	17.2	3.803	2.045	*	0.000	11.16	0.15
EDCSNJ1411037-1147286	26	0.5161	2	155.9	160.6	8.2	4.186	2.199	–	0.139	11.19	0.11
EDCSNJ1411059-1147515	26	0.5229	1	142.7	147	21.5	0.9881	2.857	*	0.000	10.65	0.09
EDCSNJ1411041-1148232	26	0.5177	1	150.5	155	7.2	20.58	0.8911	*	0.000	11.29	0.11
EDCSNJ1420104-1233451	15	0.4944	1	177.5	182.7	13.6	2.283	2.511	–	0.243	11.15	0.13

Table 1. continued.

Name	$N_{\rm clus}$	z	S Type	$\sigma_{\rm mes}$ (km s^{-1})	$\sigma_{\rm cor}$ (km s^{-1})	dσ (km s^{-1})	$R_{\rm e}$ (kpc)	$\log I_{\rm e}$ $\log L_{\odot}/{\rm pc}^2$	T Type	$P_{\rm S}$	$\log M_*$ $\log\ M_{\odot}$	dlog M_* $\log\ M_{\odot}$
EDCSNJ1420098-1233566	15	0.4958	1	143.6	147.8	11.5	1.909	2.6	–	0.213	10.99	0.10
EDCSNJ1420164-1235291	15	0.4958	1	119.9	123.4	17.7	2.87	2.099	–	0.127	10.78	0.13
EDCSNJ1420201-1236297	15	0.4969	1	268.4	276.3	7	11.91	1.639	*	0.000	11.67	0.08
EDCSNJ1420219-1237051	15	0.4956	1	212.6	218.8	28.5	0.8876	2.781	–	0.055	10.61	0.13
EDCSNJ1420235-1237178	15	0.4957	1	148.8	153.2	14.8	2.639	2.209	–	0.133	10.81	0.12
EDCSNJ1420228-1233529	15	0.4954	2	189.3	194.8	10.1	3.781	2.192	–	0.191	11.17	0.13
EDCSNJ1420181-1236230	15	0.489	1	234	240.8	15.2	4.454	1.94	*	0.000	11.28	0.10
EDCSNJ1420184-1236427	15	0.4965	1	219.9	226.3	19	5.343	1.847	–	0.197	11.24	0.10
EDCSNJ1420132-1237440	15	0.4976	1	159.3	164	19.6	2.303	2.405	–	0.162	11.06	0.09
EDCSNJ1420202-1236281	15	0.4938	1	284.1	292.4	22.8	5.752	2.075	*	0.000	11.6	0.07

Table 2. The FP parameters of field galaxies.

Name	z	S Type	$\sigma_{\rm mes}$ (km s^{-1})	$\sigma_{\rm cor}$ (km s^{-1})	dσ (km s^{-1})	$R_{\rm e}$ (kpc)	$\log I_{\rm e}$ $\log L_{\odot}/{\rm pc}^2$	T Type	$P_{\rm S}$	$\log M_*$ $\log\ M_{\odot}$	dlog M_* $\log\ M_{\odot}$
EDCSNJ1040391-1155167	0.766	1	177.8	184.4	29.9	0.9953	2.842	−5	0.049	10.78	0.07
EDCSNJ1040343-1155414	0.7807	1	290.4	301.3	17.1	3.494	2.562	−5	0.369	11.58	0.05
EDCSNJ1040476-1158184	0.6171	1	161.9	167.4	10.4	1.745	2.561	−2	0.276	10.99	0.08
EDCSNJ1054253-1148349	0.8657	1	231.8	240.9	43.6	1.646	2.916	−5	0.057	11.11	0.07
EDCSNJ1054289-1146428	0.2491	1	258.6	261.5	5.5	4.418	2.225	−2	0.090	11.51	0.55
EDCSNJ1054239-1145236	0.7408	1	200.8	208.2	9.4	2.376	2.901	−5	0.169	11.37	0.07
EDCSNJ1054339-1147352	0.8608	1	153	159	14.4	1.65	2.947	3	0.073	11.13	0.09
EDCSNJ1054240-1147364	0.6124	2	201.7	208.5	12.9	3.552	2.402	−5	0.190	11.73	0.04
EDCSNJ1054525-1244189	0.7283	1	211.9	219.7	6.9	3.174	2.527	1	0.185	11.38	0.04
EDCSNJ1054353-1246528	0.6932	1	191.2	198	13.1	3.102	2.342	1	0.166	11.61	0.06
EDCSNJ1054487-1245052	0.6189	2	136.2	140.8	10.4	1.462	2.753	−2	0.070	10.96	0.08
EDCSNJ1216402-1201593	0.3463	1	224.5	229.1	6.3	2.229	2.456	−5	0.174	11.45	0.23
EDCSNJ1216508-1157576	0.6501	1	132	136.6	24.5	0.9882	3.072	−5	0.068	10.92	0.08
EDCSNJ1216476-1202280	0.5434	1	209.9	216.5	20.1	1.164	3.015	−2	0.191	11.21	0.09
EDCSNJ1216445-1203359	0.2344	1	139.5	140.8	6.3	3.83	2.089	−5	0.082	11.09	0.87
EDCSNJ1216364-1200087	0.7868	1	166.4	172.7	16.6	1.065	3.115	−2	0.031	10.97	0.06
EDCSNJ1216449-1202139	0.6691	1	160.5	166.1	12.8	2.109	2.618	−5	0.155	11.1	0.07
EDCSNJ1216527-1202553	0.8263	1	226.9	235.6	20.4	0.8582	3.428	−5	0.039	10.99	0.05
EDCSNJ1216548-1157451	0.8746	2	169.8	176.5	26.9	2.799	2.704	3	0.047	11.27	0.69
EDCSNJ1232326-1249355	0.4186	1	235	241	35.4	0.9256	2.944	−2	0.111	11.09	0.12
EDCSNJ1232285-1252553	0.8457	1	144.3	149.9	22.8	2.747	2.544	−5	0.065	11.16	0.07
EDCSNJ1232315-1251578	0.4171	2	117.7	120.7	22.8	4.337	1.952	−2	0.099	11.13	0.15
EDCSNJ1037540-1241435	0.4329	1	126.2	129.5	15.6	2.111	2.102	−5	0.122	10.67	0.09
EDCSNJ1037448-1245026	0.4456	1	113.5	116.5	17.3	1.029	2.615	−5	0.053	10.57	0.11
EDCSNJ1037534-1246259	0.4948	2	212.5	218.7	13	1.285	2.724	−2	0.058	10.98	0.06
EDCSNJ1037595-1245095	0.8736	2	356.8	370.8	21.6	1.878	2.961	1	0.060	11.35	0.04
EDCSNJ1037529-1246428	0.6452	1	178.8	185	18.8	1.365	2.617	−5	0.068	10.79	0.08
EDCSNJ1103531-1243328	0.7221	1	134.7	139.6	14.7	2.711	2.679	−5	0.330	11.23	0.10
EDCSNJ1103418-1244344	0.3539	1	146.9	150	11.9	1.222	2.353	−2	0.188	10.71	0.28
EDCSNJ1103430-1245370	0.6584	1	205.6	212.8	10.8	2.085	2.601	−2	0.297	11.2	0.07
EDCSNJ1138100-1136361	0.4389	2	160.6	164.9	20.9	1.378	2.708	−2	0.096	10.78	0.16
EDCSNJ1138126-1131500	0.9079	1	202.3	210.3	20.4	1.665	3.256	−2	0.064	11.24	0.08
EDCSNJ1138078-1134468	0.5282	2	129	133	13.3	1.798	2.453	−2	0.030	10.96	0.11
EDCSNJ1354144-1228536	0.8245	2	188.7	196	11.4	2.607	2.664	1	0.231	11.47	0.08
EDCSNJ1354107-1231236	0.6183	2	207.3	214.3	14.9	1.089	2.915	−2	0.216	10.87	0.09
EDCSNJ1354016-1231578	0.4783	1	129.4	133.1	12.9	1.539	2.429	−2	0.117	10.78	0.08
EDCSNJ1354055-1234136	0.5142	2	205.4	211.6	12.9	2.483	2.363	1	0.068	11	0.09
EDCSNJ1354139-1229474	0.6865	2	127.4	131.9	20.3	1.66	2.631	−5	0.076	10.88	0.14
EDCSNJ1354161-1234210	0.5391	1	139.5	143.8	18.9	1.521	2.753	1	0.162	10.53	0.05
EDCSNJ1354164-1229192	0.6846	2	164.6	170.5	12.3	3.108	2.463	−2	0.167	11.45	0.06

Table 2. continued.

Name	z	S Type	σ_{mes} (km s^{-1})	σ_{cor} (km s^{-1})	dσ (km s^{-1})	R_{e} (kpc)	$\log I_{\mathrm{e}}$ $\log L_{\odot}/\mathrm{pc}^2$	T Type	P_{S}	$\log M_*$ $\log\ M_{\odot}$	dlog M_* $\log\ M_{\odot}$
EDCSNJ1354130-1230263	0.8223	1	251.3	260.9	17.6	1.244	3.174	3	0.229	11.09	0.05
EDCSNJ1054143-1144503	0.3976	2	243.9	249.8	34.4	1.361	2.142	–	0.045	10.64	0.11
EDCSNJ1054499-1247587	0.802	1	248.3	257.7	13.1	6.362	2.041	–	0.165	11.39	0.04
EDCSNJ1216435-1203502	0.6693	2	231.1	239.2	21.3	2.57	2.296	*	0.000	11.08	0.07
EDCSNJ1232293-1254348	0.7518	1	175	181.5	25.7	1.543	2.885	–	0.066	11.69	0.26
EDCSNJ1018465-1213510	0.4888	1	251.6	258.9	36.4	1.714	2.557	–	0.091	11.03	0.05
EDCSNJ1059233-1251010	0.5182	1	209.9	216.2	12.8	2.378	2.235	–	0.153	11.1	0.10
EDCSNJ1059055-1249491	0.675	1	174.8	181	22.2	2.297	2.218	–	0.023	10.56	0.06
EDCSNJ1059149-1251030	0.6248	1	140.9	145.7	16.8	0.6406	3.543	–	0.174	10.8	0.05
EDCSNJ1059198-1252101	0.6319	2	206.1	213.1	19.9	3.192	2.212	–	0.106	11.2	0.20
EDCSNJ1059132-1250585	0.8506	1	109.3	113.5	10.5	1.089	3.219	–	0.081	10.7	0.06
EDCSNJ1059225-1251279	0.2966	1	214.1	217.6	6.2	2.874	2.481	*	0.081	11.48	0.13
EDCSNJ1059224-1254492	0.5184	1	192	197.8	11.1	3.387	2.47	–	0.166	11.41	0.12
EDCSNJ1119226-1128488	0.5269	2	252.6	260.3	23.6	2.235	2.676	–	0.148	11.29	0.13
EDCSNJ1119216-1132475	0.4764	1	132.1	135.8	18.4	1.071	3.256	*	0.000	11.25	0.12
EDCSNJ1119194-1133231	0.7092	2	210.7	218.3	37.7	2.386	2.639	–	0.167	11.09	0.25
EDCSNJ1119271-1130174	0.6439	1	216.2	223.7	14.7	2.555	2.547	–	0.358	11.14	0.12
EDCSNJ1202496-1222081	0.3791	1	125.9	128.8	18.3	2.32	1.883	*	0.000	10.54	0.30
EDCSNJ1227589-1139039	0.4911	1	105.2	108.3	12.2	1.162	2.817	*	0.000	10.73	0.14
EDCSNJ1227539-1140303	0.834	2	163.5	169.8	21.3	3.916	2.297	–	0.096	11.34	0.04
EDCSNJ1227578-1136570	0.4679	1	159.3	163.8	10.2	5.679	1.581	–	0.128	11.15	0.09
EDCSNJ1227552-1137559	0.4893	1	146.5	150.7	8.1	2.536	2.317	*	0.000	11.09	0.13
EDCSNJ1227496-1138046	0.4879	2	169.4	174.3	17	4.618	1.77	*	0.000	11.18	0.09
EDCSNJ1228009-1138122	0.7081	2	184.8	191.5	21	6.839	1.702	–	0.097	11.32	0.07
EDCSNJ1301413-1138172	0.3534	1	123.8	126.4	21.4	3.472	1.962	–	0.105	10.98	0.15
EDCSNJ1353107-1135521	0.5559	1	176.4	182	28.5	1.458	2.687	–	0.235	10.89	0.07
EDCSNJ1353037-1136152	0.5705	2	203.1	209.6	19.3	5.696	1.845	*	0.000	11.1	0.06
EDCSNJ1352578-1138286	0.6292	1	185.9	192.2	16.3	1.313	2.966	–	0.366	10.9	0.06
EDCSNJ1353108-1139340	0.424	1	130.1	133.4	10.4	7.238	1.792	–	0.264	11.17	0.16
EDCSNJ1410565-1146209	0.3252	1	148.9	151.7	25.5	2.515	1.821	*	0.000	10.41	0.25
EDCSNJ1410570-1147052	0.3179	1	164.8	167.8	16.1	1.308	2.221	–	0.126	10.21	0.30
EDCSNJ1411028-1149063	0.4001	2	159.1	163	19	2.57	2.281	–	0.156	10.79	0.15
EDCSNJ1411143-1149241	0.4291	2	163.4	167.6	23.9	5.562	1.552	–	0.106	10.27	1.56
EDCSNJ1411171-1150200	0.4102	1	161.4	165.4	6.9	2.129	2.65	–	0.083	11.12	0.17
EDCSNJ1420242-1233126	0.4656	1	128	131.6	15.3	2.914	2.231	–	0.181	11.03	0.13
EDCSNJ1420185-1235026	0.7022	1	254.4	263.6	12.8	5.828	2.252	*	0.000	11.4	0.05
EDCSNJ1420224-1235422	0.6071	2	135.9	140.4	17.8	2.193	2.668	–	0.330	10.96	0.07
EDCSNJ1420231-1239076	0.3964	1	173.8	178	27.9	6.128	1.673	–	0.180	10.83	0.14

Table 3. The structural parameters of galaxies with measured velocity dispersions and HST photometry derived from Sersic fits to HST images and bulge+disk fits to VLT images.

Name	R_e(Sersic) (kpc)	$\log I_e$(Sersic) $\log L_\odot/pc^2$	R_e(VLT) (kpc)	$\log I_e$(VLT) $\log L_\odot/pc^2$
EDCSNJ1040403-1156042	6.153	1.986	9.822	1.682
EDCSNJ1040407-1156015	1.698	2.808	2.923	2.448
EDCSNJ1040346-1157566	3.348	2.319	5.857	1.885
EDCSNJ1040396-1155183	2.244	2.549	2.624	2.411
EDCSNJ1040356-1156026	2.345	2.659	2.543	2.606
EDCSNJ1054244-1146194	5.945	2.155	12.3	1.648
EDCSNJ1054250-1146238	3.465	2.431	8.08	1.855
EDCSNJ1054309-1147095	3.84	2.125	3.461	2.182
EDCSNJ1054263-1148407	4.523	1.927	5.196	1.854
EDCSNJ1054338-1149299	2.965	2.484	3.749	2.325
EDCSNJ1054280-1149598	1.802	2.533	2.298	2.386
EDCSNJ1054296-1147123	2.547	2.657	4.457	2.251
EDCSNJ1054278-1149580	3.372	2.522	5.019	2.268
EDCSNJ1054305-1146536	9.346	1.969	10.06	1.911
EDCSNJ1054303-1149132	4.856	2.191	9.448	1.797
EDCSNJ1054237-1146107	0.9561	2.729	0.9133	2.674
EDCSNJ1054246-1146124	6.194	1.753	5.918	1.761
EDCSNJ1054467-1245035	1.883	2.68	2.574	2.456
EDCSNJ1054435-1245519	9.555	1.849	15.48	1.566
EDCSNJ1054451-1247336	1.516	2.809	1.716	2.758
EDCSNJ1054436-1244202	1.297	2.993	0	−1948
EDCSNJ1054438-1245409	1.606	2.906	7.235	1.813
EDCSNJ1054445-1246173	1.373	2.713	1.057	2.955
EDCSNJ1054440-1246390	1.692	2.513	10.37	1.287
EDCSNJ1054442-1245331	1.684	2.142	1.377	2.184
EDCSNJ1054439-1245556	2.806	2.311	3.648	2.133
EDCSNJ1054398-1246055	5.88	2.251	4.916	2.329
EDCSNJ1054396-1248241	2.259	2.484	2.934	2.332
EDCSNJ1054431-1246205	5.025	1.601	4.152	1.686
EDCSNJ1216470-1159267	2.12	2.563	1.696	2.724
EDCSNJ1216454-1200017	2.494	2.451	3.876	2.146
EDCSNJ1216490-1200091	4.425	2.075	2.017	2.579
EDCSNJ1216453-1201176	8.92	2.033	16.17	1.716
EDCSNJ1216420-1201509	3.867	2.58	5.471	2.308
EDCSNJ1216468-1202226	6.409	1.907	4.355	2.11
EDCSNJ1216401-1202352	1.41	3.14	2.046	2.876
EDCSNJ1216462-1200073	1.052	2.957	0.8956	3.072
EDCSNJ1216418-1200449	2.802	2.35	5.177	1.936
EDCSNJ1216438-1200536	1.855	2.876	2.129	2.798
EDCSNJ1216461-1201143	4.748	2.453	6.957	2.158
EDCSNJ1216456-1201080	7.863	1.718	11.69	1.457
EDCSNJ1216453-1201209	5.509	2.012	10.02	1.7
EDCSNJ1216443-1201429	1.846	2.612	7.068	1.966
EDCSNJ1216438-1202155	0.6206	3.296	0	−1997
EDCSNJ1216417-1203054	0.9622	3.347	0.5713	3.766
EDCSNJ1216359-1200294	0.9401	3.255	0.8689	3.258
EDCSNJ1216446-1201089	1.6	2.664	4.238	2.017
EDCSNJ1216449-1201203	2.972	2.406	27.13	0.9842
EDCSNJ1216403-1202029	1.948	2.247	14.17	1.035
EDCSNJ1216522-1200595	1.641	2.53	0	−1949
EDCSNJ1216382-1202517	3.456	2.409	9.366	1.727
EDCSNJ1216387-1201503	1.297	3.06	1.834	2.811
EDCSNJ1232318-1249049	2.125	2.291	4.021	1.839
EDCSNJ1232280-1249353	4.062	2.283	4.521	2.151
EDCSNJ1232303-1250364	19.73	1.414	20.46	1.404
EDCSNJ1232250-1251551	2.304	2.438	2.034	2.483
EDCSNJ1232287-1252369	2.445	2.483	2.691	2.409
EDCSNJ1232271-1253013	2.554	2.383	3.256	2.208
EDCSNJ1232343-1249265	1.42	2.767	0.8388	3.2
EDCSNJ1232350-1250103	5.685	1.928	3.762	2.147

Table 3. continued.

Name	R_e(Sersic) (kpc)	$\log I_e$(Sersic) $\log L_\odot/pc^2$	R_e(VLT) (kpc)	$\log I_e$(VLT) $\log L_\odot/pc^2$
EDCSNJ1232313-1250327	1.44	2.523	19.95	0.6675
EDCSNJ1232317-1249275	5.449	2.049	5.643	1.964
EDCSNJ1232309-1249408	3.62	2.476	4.613	2.269
EDCSNJ1232303-1251092	1.087	2.637	1.262	2.472
EDCSNJ1232303-1251441	2.704	2.14	2.002	2.294
EDCSNJ1232370-1248239	1.831	2.605	2.289	2.428
EDCSNJ1232372-1249258	0.6312	2.869	1.396	2.254
EDCSNJ1232296-1250119	5.102	2.011	6.447	1.831
EDCSNJ1232301-1250362	1.105	2.615	8.984	1.332
EDCSNJ1232288-1250490	2.169	2.539	2.457	2.449
EDCSNJ1232299-1251034	1.526	2.526	1.231	2.712
EDCSNJ1232207-1252016	7.029	1.96	9.614	1.73
EDCSNJ1232204-1249547	4.347	2.223	3.337	2.403
EDCSNJ1037527-1243456	1.268	2.81	2.49	2.363
EDCSNJ1037548-1245113	1.74	2.889	1.263	3.175
EDCSNJ1037447-1246050	1.483	2.292	1.433	2.391
EDCSNJ1037552-1246368	1.942	2.157	1.75	2.205
EDCSNJ1037535-1241538	3.661	1.954	5.46	1.674
EDCSNJ1037525-1243541	1.731	2.666	1.616	2.716
EDCSNJ1037428-1245573	3.259	2.02	3.723	1.927
EDCSNJ1037527-1244485	2.494	2.284	2.444	2.284
EDCSNJ1037473-1246245	0.7199	2.772	3.525	1.637
EDCSNJ1103365-1244223	6.787	2.159	7.192	2.075
EDCSNJ1103372-1245215	2.682	2.305	2.563	2.316
EDCSNJ1103363-1246220	2.645	2.199	3.895	1.941
EDCSNJ1103444-1245153	2.327	2.852	2.526	2.764
EDCSNJ1103349-1246462	5.823	2.037	7.501	1.855
EDCSNJ1103413-1244379	2.637	2.441	3.182	2.319
EDCSNJ1103357-1246398	1.741	2.484	1.871	2.374
EDCSNJ1138068-1132285	3.893	1.703	3.365	1.705
EDCSNJ1138102-1133379	6.071	1.917	16.73	1.246
EDCSNJ1138069-1134314	1.692	2.565	2.575	2.224
EDCSNJ1138074-1137138	2.877	2.326	3.817	2.124
EDCSNJ1138104-1133319	4.137	1.562	5.453	1.361
EDCSNJ1138107-1133431	1.604	2.492	1.916	2.312
EDCSNJ1138127-1134211	0.9056	2.695	0.9804	2.659
EDCSNJ1138116-1134448	1.442	2.664	1.291	2.715
EDCSNJ1138069-1132044	1.138	2.66	3.871	1.74
EDCSNJ1138130-1132345	2.817	2.003	3.307	1.839
EDCSNJ1138110-1133411	2.813	1.917	3.308	1.763
EDCSNJ1138022-1135459	3.447	2.107	5.677	1.747
EDCSNJ1138065-1136018	3.032	1.584	5.204	1.243
EDCSNJ1138031-1134278	1.293	2.54	1.485	2.428
EDCSNJ1354098-1231098	0.9136	2.895	2.151	2.317
EDCSNJ1354098-1231015	7.568	1.99	13.64	1.666
EDCSNJ1354097-1230579	1.926	2.854	7.646	1.883
EDCSNJ1354026-1230127	1.385	2.64	1.492	2.564
EDCSNJ1354114-1230452	5.69	2.065	5.024	2.096
EDCSNJ1354159-1232272	0.7318	2.989	0.4524	3.394
EDCSNJ1354102-1230527	11.84	1.369	10.15	1.433
EDCSNJ1354101-1231041	1.595	2.766	8.668	1.542
EDCSNJ1354204-1234286	3.009	2.424	5.488	2.006
EDCSNJ1354106-1230499	2.117	2.635	3.311	2.334
EDCSNJ1040391-1155167	1.025	2.833	1.14	2.71
EDCSNJ1040343-1155414	3.543	2.558	5.096	2.307
EDCSNJ1040476-1158184	2.091	2.45	2.047	2.434
EDCSNJ1054253-1148349	1.526	2.977	1.711	2.915
EDCSNJ1054289-1146428	5.073	2.15	6.876	1.932
EDCSNJ1054239-1145236	2.635	2.842	2.251	2.971
EDCSNJ1054339-1147352	1.916	2.865	1.939	2.78

Table 3. continued.

Name	R_e(Sersic) (kpc)	$\log I_e$(Sersic) $\log L_\odot/\mathrm{pc}^2$	R_e(VLT) (kpc)	$\log I_e$(VLT) $\log L_\odot/\mathrm{pc}^2$
EDCSNJ1054240-1147364	4.464	2.263	10.7	1.664
EDCSNJ1054525-1244189	4.663	2.296	6.144	2.093
EDCSNJ1054353-1246528	3.469	2.282	28.39	1.085
EDCSNJ1054487-1245052	1.629	2.695	0	−1949
EDCSNJ1216402-1201593	2.423	2.402	3.819	2.033
EDCSNJ1216508-1157576	1.096	3.011	0.9015	3.123
EDCSNJ1216476-1202280	1.228	2.982	1.173	3.013
EDCSNJ1216445-1203359	4.625	1.977	6.214	1.723
EDCSNJ1216364-1200087	1.345	2.958	1.076	3.08
EDCSNJ1216449-1202139	2.355	2.549	1.783	2.712
EDCSNJ1216527-1202553	0.919	3.384	0.881	3.438
EDCSNJ1216548-1157451	4.144	2.472	2.953	2.653
EDCSNJ1232326-1249355	1.116	2.822	1.658	2.505
EDCSNJ1232285-1252553	3.761	2.359	5.188	2.112
EDCSNJ1232315-1251578	5.594	1.801	4.918	1.82
EDCSNJ1037540-1241435	2.322	2.05	2.705	1.955
EDCSNJ1037448-1245026	0.9972	2.636	0.7565	2.923
EDCSNJ1037534-1246259	1.655	2.569	1.057	2.891
EDCSNJ1037595-1245095	2.377	2.815	1.824	2.981
EDCSNJ1037529-1246428	1.555	2.538	1.12	2.822
EDCSNJ1103531-1243328	3.073	2.597	6.066	2.141
EDCSNJ1103418-1244344	1.272	2.336	1.036	2.474
EDCSNJ1103430-1245370	2.203	2.571	1.966	2.665
EDCSNJ1138100-1136361	1.381	2.709	1.227	2.774
EDCSNJ1138126-1131500	1.649	3.264	1.438	3.312
EDCSNJ1138078-1134468	1.974	2.407	3.269	2.041
EDCSNJ1354144-1228536	2.011	2.852	6.39	2.076
EDCSNJ1354107-1231236	1.085	2.919	0.7461	3.224
EDCSNJ1354016-1231578	1.583	2.409	1.085	2.713
EDCSNJ1354055-1234136	2.393	2.395	3.174	2.201
EDCSNJ1354139-1229474	1.504	2.698	2.739	2.278
EDCSNJ1354161-1234210	1.061	3.002	5.412	1.854
EDCSNJ1354164-1229192	3.845	2.33	20.08	1.206
EDCSNJ1354130-1230263	1.183	3.204	2.775	2.572